# COMPACT AUGMENTED SPARK IGNITERS FOR LIQUID ROCKET ENGINES

By

Darren C. Tinker

Dissertation

Submitted to the Faculty of the

Graduate School of Vanderbilt University

In partial fulfillment of the requirements

For the degree of

DOCTOR OF PHILOSOPHY

in

Mechanical Engineering

January 31, 2021

Nashville, Tennessee

Approved:

Robert W. Pitz, Ph.D.

Haoxiang Luo, Ph.D.

Kenneth Pence, Ph.D.

Alvin Strauss, Ph.D.

Tom Brown, Ph.D.

Robin J. Osborne, M.S.

© 2020 by Darren C. Tinker

## DEDICATION

For Hobbes, you fat lovable ball of fur

## ACKNOWLEDGEMENTS

I would like to thank my committee for their efforts throughout this research project. Thank you to my committee, Robert W. Pitz, Haoxiang Luo, Ken Pence, Alvin Strauss, Robin J. Osborne, and Tom Brown. Thank you to Dr. Pitz for your guidance, advice, and patience while overseeing a project that was a nontrivial deviation from the active work in your lab and required a strong investment from us both. Thank you, Robin, for all the mentorship, time, and effort you have devoted to this project. You have clearly been invested in both my work and professional development throughout my time as a NASA fellow. I could not have done this without you. Thank you to everyone in the Engine Components & Technology Branch (ER13) who have provided feedback and advice on my work. Thank you to Jeff West and Brian Richardson in the Fluid Dynamics Branch (ER42) for guiding and mentoring me through the CFD campaign that became a much larger portion of my dissertation than I ever expected. Thank you to John Peugeot and Paul Dumbacher for support that enabled me to complete experimental phases of this work. Thank you to all the NASA employees who have made this work possible. A list to compose what each of you have done for me would surpass this dissertation. Thank you to the NASA Space Technology Research Fellowship (grant NNX16AM57H) for funding my efforts. Thank you to A. V. Anilkumar for your insight and advice. Thank you, John Daily, for your technical expertise and guidance. Thank you, Tom Fleetwood at Champion Aerospace, for loan of the spark exciter used in this work.

Sincere thanks go to my lab group, ever-changing over the years, but always ready with support. Chad Carpenter, Garrett Marshall, Marsalis Pullen, Conrad Reihsmann, Harshini Devathi, Will Bearden, Carl Hall, and Nathan Grady, you have all made great coworkers, teammates, and friends. No shout-out does justice to my appreciation. Thank you, Dex Watkins, for your friendship, candor, and enthusiasm for educational mischief. Thank you, Devany Sweitzer, for always lending a hand, an ear, and an alibi when they were needed most. Thank you, Kelsay Neely, for always providing insightful feedback on my writing and for your hand in revising the poem that translates my work so eloquently. Thank you, Rachel Gravil, for your artistic talent and illustrations for my narrative poem. Thank you, Adam Jarrell, Cole Brubaker, Josh Webb, and Scott Williams, for being gym buddies, for adventures stumbling through Nashville, and

joining the shenanigans that made grad school enjoyable. Thank you, Yonatan Reches, for your undying support and exemplary moral code. Thank you, Caitlyn De Lucca and Josh Prince, for your constant support and impressive decryption skills. Thank you, Matt Gerboth and Casey Brock, for never failing to offer a tool, idea, or ear when need be. Thank you, Rufat Kulakhmetov, Monique McClain, and Alexis Harroun, for your adventures, memories, and advice as NASA fellows. Thank you, Connor Strawn, David Ziemnicki, Dylan Shane, and Kelsay Neely, for fantastic adventures through Dungeons and Dragons. Thank you, Timothy Bucklew, you have had my back for the last decade and there are not words in the English language to describe how much I enjoy and cherish our friendship even if sometimes I feel the need to hit you in the face with a chair. Thank you, Chris Fields, for always being a voice of reason, patient for the mail to arrive, and your friendship for all these years. Thank you to my trivia team, Melissa and Tyler Keagle, Dylan Shane, Chase Mu, Forrest Edens, and Kelsay Neely. You've been amazing friends and I would never question our friendship. Thank you, Will Johnson, Amber Rampey, and Nick Robbins, for all the adventures in Huntsville. Thank you Lauren Elgar Moehle (and Mark), Miriam Glicksberg, Allyson Shambaugh, and Keagan Chronister, for being the best roommates I could have hoped for in Nashville. Thank you to the Dooleys and Sarah DeGeorge for always taking the time to review my work at the drop of a hat. Thank you to my undergraduate professors who equipped me with everything I need to become the engineer I am today. Thank you, Hillary Galloway, for pushing me to apply to graduate school so many years ago. Last, but not least, thank you to my parents and family for molding me into the person I am.

## PREFACE

This dissertation contains content from two JANNAF manuscripts[1],[2] that are SENSITIVE BUT UNCLASSIFIED in their original form. To publicly release this dissertation, select text has been removed and replaced with "[REDACTED]." This and the alterations to figures and tables is to comply with the Arms Export Control Act (TITLE 22, U.S.C., Sec 2751 et seq.) or the Export Administration Act of 1979, as amended, Title 50, U.S.C., App. 2401 et. seq. Note that violations of these export laws are subject to severe criminal penalties. The original material can be disseminated in accordance with provisions of DoD Directive 5230.25. For those interested in full detail, the manuscripts are subject to Distribution Statement C: Distribution authorized to U.S. Government agencies and their contractors; Critical Technology; 2 March 2020. Other requests for these documents shall be referred to NASA Marshall Space Flight Center, Office of Protective Services, NASA MSFC, AL 35812.

[1] D. C. Tinker, B. R. Richardson, R. J. Osborne, R. W. Pitz and J. S. West, "Internal Flow of an Augmented Spark Impinging Pseudo-Pentad Igniter," *JANNAF Journal of Propulsion and Energetics*, vol. 20, no. 1, pp. 105-116, 2020.

[2] D. C. Tinker, B. R. Richardson, R. J. Osborne, R. W. Pitz and J. S. West, "Computational Verification of Objective Functions for the Design and Development of Nondimensional Mixing Correlations for a Liquid Rocket Engine Augmented Spark Impinging Pseudo-Pentad Igniter," *JANNAF Journal of Propulsion and Energetics*, vol. 11, no. 1, pp. 89-103, 2020.

## TABLE OF CONTENTS

Page

## LIST OF TABLES

## LIST OF FIGURES

## NOMENCLATURE

English Variables

| | | |
|---|---|---|
| $A$ | – | Area |
| $d$ | – | Diameter or distance |
| $L$ | – | Length |
| $M$ | – | Mass |
| $\dot{m}$ | – | Mass flow rate |
| $MR$ | – | Mixture ratio |
| $P$ | – | Pressure |
| $Re$ | – | Reynolds number |
| $T$ | – | Temperature |
| $t$ | – | Time |
| $\dot{W}$ | – | Power |
| $V$ | – | Velocity or Voltage |
| ~~$V$~~ | – | Volume |
| $x$ | – | Distance |

English Subscripts

| | | |
|---|---|---|
| b | – | Breakdown |
| $cool$ | – | Coolant flow |
| $c$ | – | Core flow |
| $f$ | – | Fuel |
| $g$ | – | Spark gap |
| $n$ | – | Index |
| $o$ | – | Oxidizer |
| $i$ | – | Injector |
| $s$ | – | Spark |
| $t$ | – | Tube |

Greek Variables

| | | |
|---|---|---|
| α | – | Fan inclination (polar) angle |
| β | – | Doublet impingement angle |
| $\eta$ | – | Axial momentum factor |
| $\gamma$ | – | Impingement Angle |
| $\mu$ | – | Dynamic viscosity |
| $\rho$ | – | Density |
| π | – | Buckingham-Pi Group |
| ψ | – | Radial momentum factor |
| $\phi$ | – | Equivalence ratio |
| $\theta$ | – | Angle or Temperature |
| $\sigma$ | – | Standard deviation |

Acronyms

| | | |
|---|---|---|
| AFLR | – | Advancing-Front/Local-Reconnection |
| ASI | – | Augmented Spark Impinging |
| CASI | – | Compact Augmented Spark Impinging |
| CI | – | Confidence Interval |
| LES | – | Large-Eddy Simulations |
| LRE | – | Liquid Rocket Engine |
| MSFC | – | Marshall Space Flight Center |
| NASA | – | National Aeronautics and Space Administration |
| NRMSE | – | Normalized Root-Mean Square Error |
| PAC | – | Plasma Assisted Combustion |
| PAI | – | Plasma Assisted Ignition |
| RANS | – | Reynolds-Averaged Navier Stokes |
| RMSE | – | Root- Mean Square Error |
| SSME | – | Space Shuttle Main Engine |
| SST | – | Shear Stress Transport |

# CHAPTER 1:
# INTRODUCTION

The benefits of spaceflight are greater than scientific discovery and the advancement of technology. Benefits from science and technology have profound impacts on the fields of agriculture, health care, transportation, energy, defense and more. More importantly, interest in space exploration is a unifying cultural force both internally and externally to the United States, bolstering enthusiasm for new discoveries, education, and continued exploration. Due to the multifaceted impacts on not only a single nation, but also the world, the advancement of space technology is of the utmost importance for mankind.

Spaceflight often begins with a simple spark, and logically, the ignition system of any rocket engine requires the highest attention to detail. Reliable ignition is critical for both in-space applications and launch propulsion systems associated with terrestrial ascent and descent operations. Innovations in manufacturing techniques have offered opportunities to advance liquid rocket engine (LRE) igniters and improve design. For this advancement, one must go beyond tradition, intuition, and iteration used in years past. The aim is to create accurate and cost-effective predictive design models to provide guidance from fundamental theory that has been verified with rigor and validated by comprehensive experimental testing. To safely propel our astronauts, there is need for this foundation of knowledge for future design work, as the ignition event has many unknowns that demand to be answered – from the first spark to the raging fire of the engines.

Preventing the loss of life requires reliable ignition systems. In turn, spark igniters (akin to their automotive counterparts) are an attractive solution. However, ignition is reliant upon a flammable mixture passing through the spark early in the transient engine start. While direct-spark ignition of rocket engine main combustion chambers has been successfully implemented in engines such as RL-10 [1, 2, 3], the development time can be substantial due to ignition in such devices requires precise and repeatable control of the propellant mixture ratio within the very small volume. The preferred method of implementing spark igniters within rocket engines – especially large engines – is to design a smaller pre-chamber and use an augmented spark igniter (ASI) interchangeably referred to as a torch igniter.

Spark-initiated torch igniters have proven to be both reliable and reusable ignition devices for many of NASA's human-rated vehicles [4]. Torch igniters have been used to light both preburners as well as the main combustion chamber for both core- and upper-stage engines. They are also ideal for ignition needs of component-level tests where minimizing downtime between tests is crucial for efficient ground operations. Ignition phenomena in LREs may appear to be perfected and well understood but that is far from the truth. The torch igniters in these large-scale engines required years of trial-and-error testing and design iteration.

Even within the smaller volume of an ASI pre-chamber, immediate and reliable ignition can still be a design challenge, especially with hydrocarbon-based fuels. To date, the only use of spark igniters in human-rated rocket engines is with pure hydrogen, which has much broader flammability limits than hydrocarbon fuels when combined with oxygen [5]. Highly reliable hydrogen-oxygen torch igniters are found in man-rated hydrogen-oxygen LREs such as the second stage J-2 engine and Space Shuttle Main Engine (a.k.a. the RS-25 engine) [4]. The biggest challenge, which is the focus of this research, is the design of a reliable methane-oxygen torch igniter. The SpaceX Raptor Engine and Blue Origin BE-4 Engine are currently in the development stage and use methane-oxygen, but ignition reliability has not been shown. There is limited literature on the ignition phenomena of methane-oxygen LREs, and there are no man-rated, or for that matter any flight LREs using methane-oxygen.

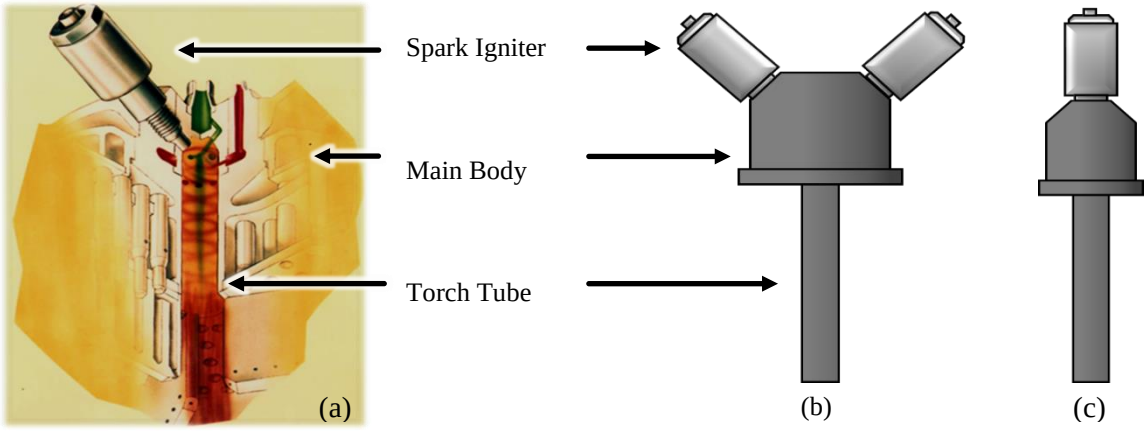


Figure 1 – (a) An artistic rendering of the SSME torch igniter [4], and depictions of (b) a traditional augmented spark igniter and (c) a compact augmented spark igniter

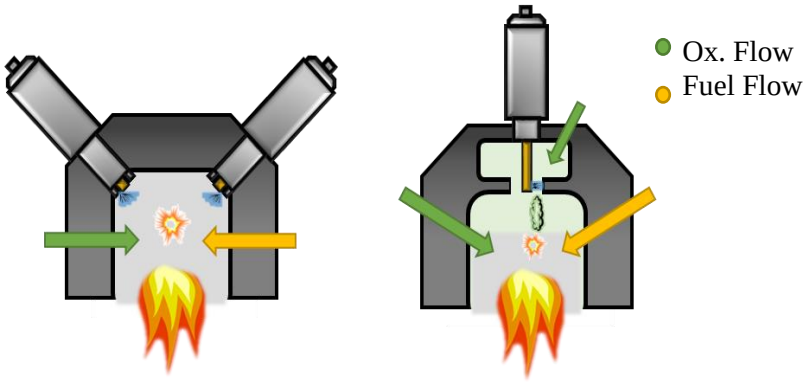


Figure 2 – Direct spark ignition (left) vs. plasma assisted ignition (right)

The best known LRE that uses an ASI is the Space Shuttle Main Engine (SSME) with an artistic rendering shown in Figure 1a [4]. Dual-redundant spark igniters are used to light the flame at the base of the pre-chamber (see Figure 2, left) and the fuel is swirled as it progresses down the torch tube, shielding the walls from the heat of combustion as the core flow reacts. The flame exits the torch tube and then ignites the propellants of the main injector.

To minimize the component volume and weight, the compact augmented spark impinging (CASI) igniter design has a single spark igniter along the axis of the torch tube (see Figure 1c). Instead of direct spark ignition in a combustible mixture, oxygen is flowed through and excited by an annular electrode during the spark discharge (see Figure 2, right). The plasma cloud is pushed away from the electrodes, toward a flammable volume of gas, and reduces potential for cold-wall quenching of the combustion kernel. The kernel stabilizes at the impingement point of the deficient reactant and sustains the core flame of the igniter. The propellant mass flow rates are set so that the core flow is either fuel-rich or fuel-lean mixtures, which results in a lower adiabatic flame temperature and therefore a lower heat load on the igniter torch tube. The exhaust from the torch tube exits primarily as hot oxygen and a variable composition of reaction products. The gases exiting the core tube react with a coaxial fuel shroud and create the global flame, which is the pilot light of the engine. To summarize, the CASI igniter has four primary stages of operation (see Figure 3) with many questions in between. While simplified in both words and art, the ignition process and

steady-flow operation of a torch igniter involves complex underlying phenomena, and comprehension is essential.

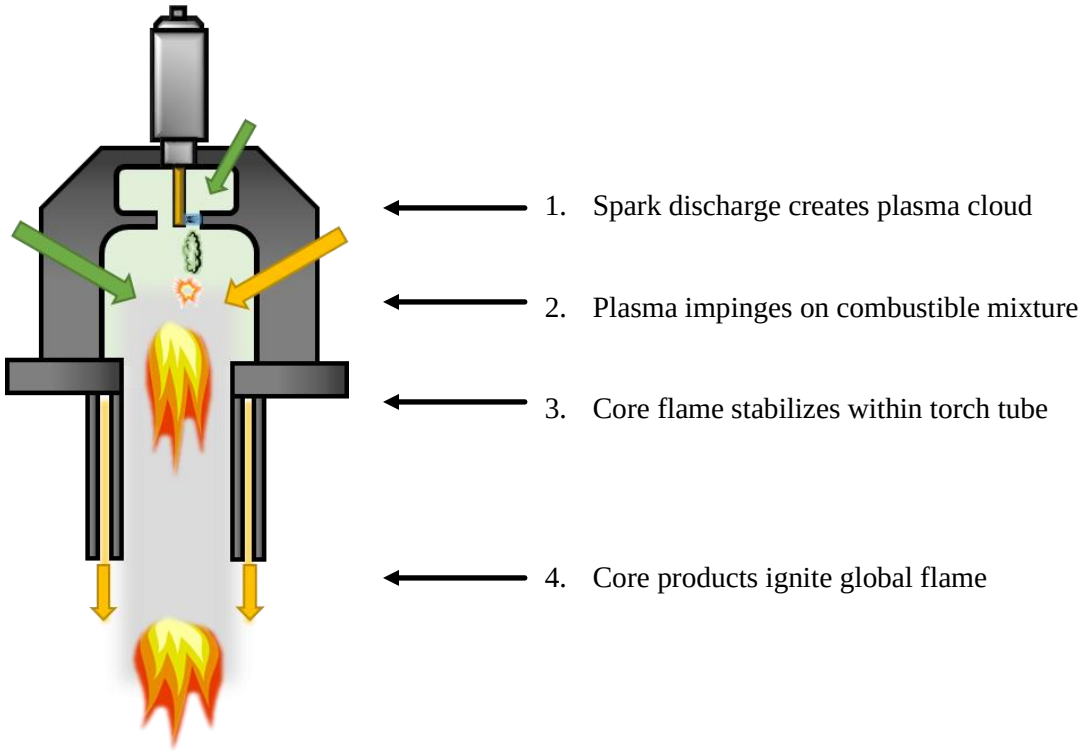


Figure 3 –Ignition process for a compact augmented spark impinging igniter

The first three of the four stages of operation, shown in Figure 3, are studied in this dissertation, and the results of these studies demonstrate that some aspects of CASI igniter performance can be predicted through analytic relations. In short, this work will provide objective functions that can be used in designing CASI igniters. The three specific aims to accomplish this are to (1) investigate spark discharges in non-reacting flowing gases, (2) develop and verify analytic design solutions through computational fluid dynamics (CFD) simulations, and (3) examine methane-oxygen plasma-assisted ignition reliability.

## PRESENT STATE OF THE FIELD AND PRIOR WORK

Noteworthy advances in liquid-methane technology are occurring for main-engine injectors, cryogenic fluid management, pump-fed and pressure-fed main engines, and rocket igniters [6, 7, 8]. NASA is coupling additive manufacturing to cryogenic liquid fuel systems, and has successfully ground-tested 3D-printed, prototype, rocket fuel pumps [9], injectors [10], and igniters specific to the RS-25 engine. Many of these

prototypes show the benefits of additive manufacture through reduced cost and freedom of design. Future propulsion technology must adhere to and take advantage of these advancements in manufacturing methods.

Liquid propulsion technology is also influenced by fuel selection due to political, environmental, and mission specific needs. Interest in liquid methane has grown due to its less rigorous storage requirements, higher energy density, and greater stability as compared to liquid hydrogen [11], yet currently there are no flight-rated liquid-methane rocket engines. Not only is there a natural abundance of methane on Earth, but in-situ harvesting holds significant promise on Mars [12, 13] and would lower system complexity and overall costs for interplanetary space missions [14]. The evidence mounting indicates that the conversion from liquid-hydrogen to liquid-methane architecture is highly probable, and research on such systems should occur before the need is pressing.

Traditional ignition methods for rocket engines include hypergolics, pyrotechnics, hot wires, spark igniters, and torch igniters. Each has their own benefits and drawbacks – hypergolics will always react, but are toxic and corrosive; pyrotechnics are reliable, but have high cost due to touch time (man hours); etc. – and thus selection of a given method is dependent on mission needs. For liquid propellant rocket engines, spark igniters are often used indirectly to light preburners, gas generators, and main thrust chambers [15] as depicted in Figure 4. Attraction for spark igniters is strongly influenced by their ability for repeatable engine starts and high reliability. In the case of direct spark ignition, a sustainable combustion reaction is reliant upon an ignitable mixture passing near the spark tip very early in the engine start transient, prior to pressure quenching of the spark. Generally, the preferred method of implementing spark igniters within rocket engines – especially larger engines – is to design a smaller augmented spark igniter (ASI) pre-chamber in which propellant injection and mixture ratio near the spark plasma can be controlled independent of the engine injector. The resultant combustion products within the small pre-chamber are directed into the larger engine chamber via a torch tube. An ASI is advantageous because the output torch flame is much larger and more energetic than a discrete train of small spark plasmas. Hence, ASI's have the reliable and repeatable characteristics of a lone spark igniter with a more robust ignition source for large scale engines.

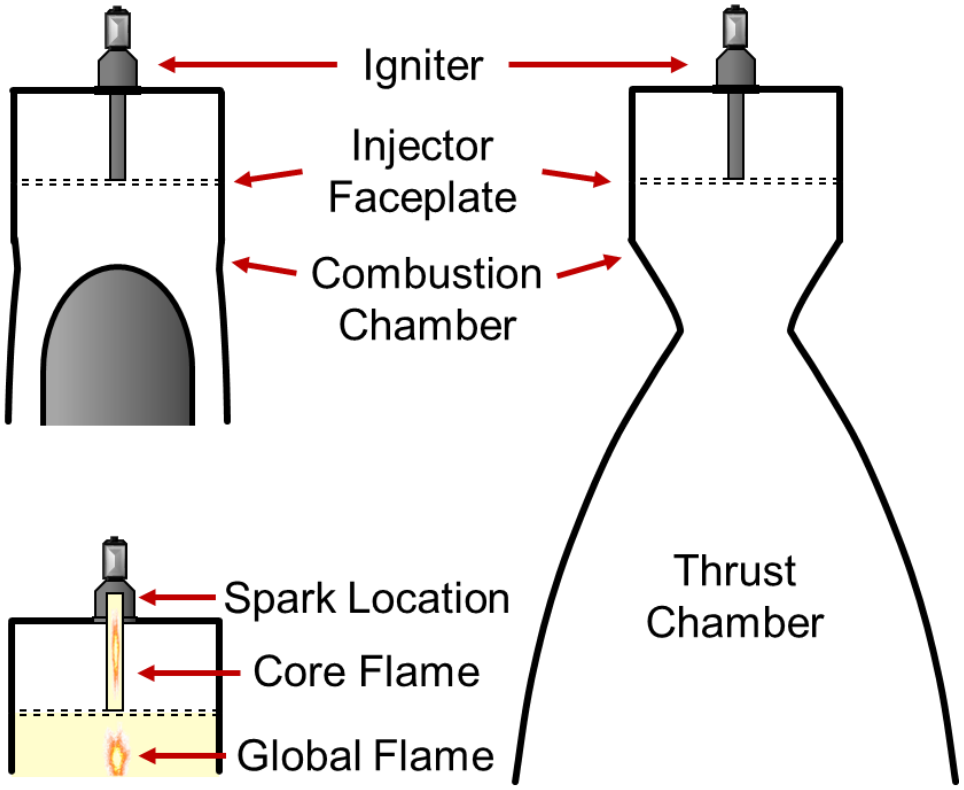


Figure 4 – Torch igniter placement relative to a preburner or combustion chamber and the relative locations of the spark event, core flame, and global flames

## SUBJECT OF THE CURRENT STUDY: THE COMPACT AUGMENTED SPARK IMPINGING (CASI) IGNITER

The ASI studied in this work is a compact augmented spark impinging (CASI) igniter, and has an injector configuration resembling a pentad. An illustrative cutout of the igniter is shown in Figure 5, depicting three of the five injectors as the others are out of plane. The central injector, colinear with the torch tube axis, contains a spark igniter that is used to excite and energize the oxidizer flowing through it. The remaining injectors are pairs of like-doublets (i.e., two streams of the same fluid), one set for the fuel and one set for the oxidizer. During the transient startup, while one reactant flows through the central injector, an electrical arc travels between the spark electrode and igniter body. The fluid along this radial arc is energized and excited, to create a short-lived plasma. While the spark igniter remains powered, spark discharges occur at a consistent repetition rate to form multiple discrete plasma clouds.

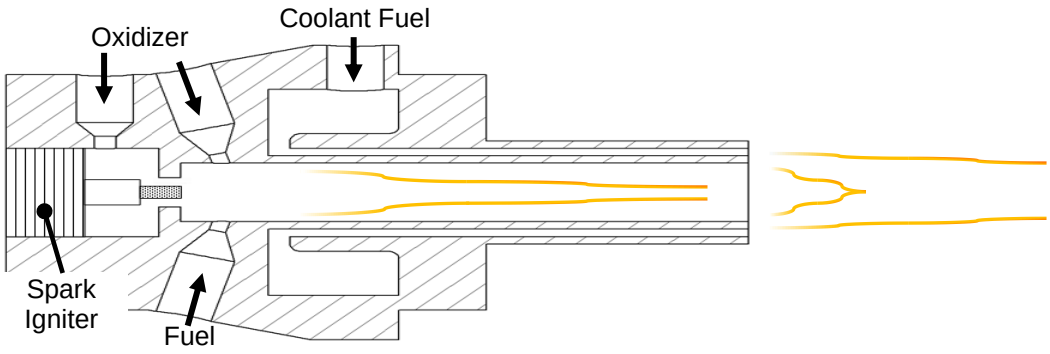


Figure 5 – Side-view cut-out example of 3D printed torch igniter

Containing radical species and free electrons, these short-lived pockets of hot oxidizer are projected downstream by the fluid flow toward a combustible mixture of fuel and oxidizer created by the remaining four injectors, which are in an opposed like-doublet configuration on the chamber wall. A flame kernel forms and is sustained at the impingement point of the deficient reactant. This creates and anchors the “core flame” that propagates down the length of the torch tube. A coolant fuel flows coaxially in channels along the outer edges of the wall to reduce the thermal load on the structure and exits the tube at the same location as the core flame exhaust. The hot oxidizer and other combustion products from the core flow mix and ignite with the coolant fuel shroud to form the “Global Flame” that acts as the pilot light for the main injectors.

Each stage requires attention to optimize the igniter functionality and reliability. Ignition is a multiphysics process as shown in Figure 6. Nonreacting fluid dynamics of the injectors, their mass flow rates, and local momentum fluxes are the basis for all other processes. The spark discharge results in plasma dynamics that add energy to the fluid in the forms of chemical excitation, dissociation, and increased thermal energy, but these affects may be hindered by advective dissipation or enhanced by local recirculation zones. The heat addition locally expands the fluid, which can result in shockwaves if too quickly deposited, and alters transport phenomena. If enough energy is present (thermally or through excited species) and combined with a locally ignitable mixture, a self-sustaining reaction may form. This combustion reaction is then a continual source of heat that feeds back into the fluid dynamics through changes in density, thermal conductivity, chemical composition, and more.

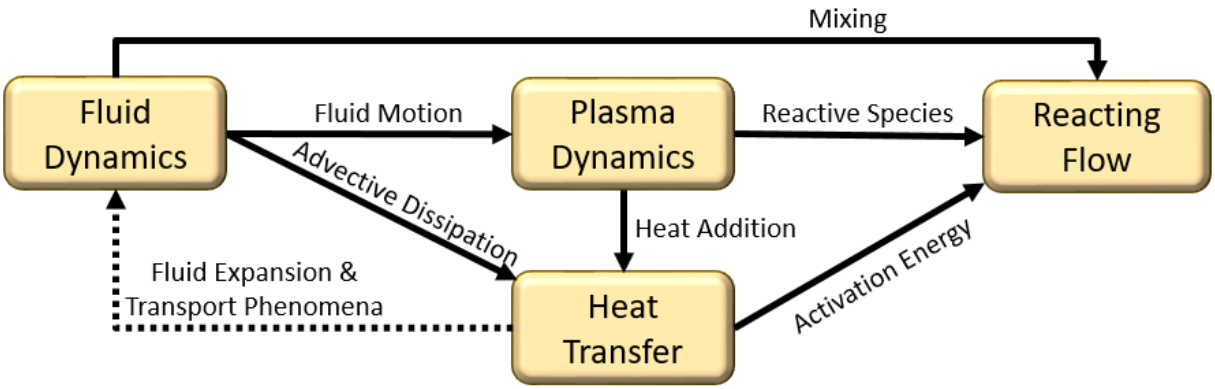


Figure 6 – Multiphysics relations for augmented spark ignition

## GOAL, OBJECTIVES, AND OUTLINE OF THE DISSERTATION

The aim of this dissertation is to characterize augmented spark impinging (torch) igniters. This body of work aims to characterize select aspects of this complex process that lead to reliable ignition while demonstrating the value of objective design functions as an analytic tool.

The first objective is to establish how large of a region may be thermally altered and the electrical properties observed for different operating conditions through a fundamental study of spark discharges. To emulate transient engine startup, spark discharges are examined against pressure, spark-gap size, and two unique capacitive exciter types. The approximate velocity and distance traveled by the exhaust plume are determined to outline the prechamber target zone where a combustible mixture is necessary for ignition. The energy imparted to the flow, channel resistance, and breakdown voltages are compared to Townsend theory (where applicable) to provide insight on discharge properties in a novel environment. The effects of spark quenching (no energy deposition) on perceived versus actual measurements are discussed to demonstrate the need for proper filtration methods, electromagnetic interference mitigation, and scrutiny of results.

Second, this work will investigate mixing correlations, estimates of flammable gas volumes, and develop novel objective design functions. The geometric design of the augmented spark impinging igniter of this work is a combination of doublets and a coaxial injector, each of which have been studied independently computationally and experimentally. Three-dimensional, time-accurate, and nonreacting computational fluid dynamics simulate the full injector configuration constrained by a torch tube to determine the effects of geometric and mass flow differences on the ability to predict local mixture ratios where energy is deposited by the spark igniter.

The third objective is to understand and determine stabilizing phenomena for combustion through fluid dynamic structures. The nonreacting computational fluid dynamics simulations are examined for features such as Mach disks and recirculation zones within the torch tube as well as effects of the vena contracta within the spark gap. The flow within the spark gap is further examined for asymmetric pressure profiles that may lead to preferential spark location and localized hardware erosion. Injector ratios and the bulk flow

Reynolds number are then investigated to approximate the size and composition of a combustible mixture near the spark gap exit.

The final objective is to quantify ignition reliability of an augmented spark impinging igniter and demonstrate the value of nondimensional variables from the previously developed objective design functions. Systematically full-scale experiments are carried out to characterize ignition probability against mixture ratios, fluid properties, propellant timing, and injector configurations. The novel objective functions for igniter design are functions of variables that may be constrained by engine-level requirements, physics, and experimental results from this body of work.

The combined results of spark discharge studies, numerical simulations, and full-scale testing provide a foundation for future igniter design and will minimize iterative processes from the design cycle for next-generation ignition hardware.

# CHAPTER 2
# CYLINDRICAL AIR-GAP ELECTRODE SPARK DISCHARGE CHARACTERIZATION AND QUENCHING

## INTRODUCTION

The aim of this study was to elucidate spark discharge characteristics, arc penetration, and exhaust plume development to guide designers of relevant ignition devices. Spark (plasma) igniters are an efficient and repeatable device for imparting energy into a localized volume of fluid. In liquid propellant rocket engines, spark igniters are often used to light pre-burners, gas generators, and main combustion chambers [15]. Rocket engines such as the RL-10 have successfully implemented direct-spark ignition of the main combustion chamber [16], but required substantial development time to precisely and repeatably control the propellant mixture ratio within the local ignition volume. Control of the mixture ratio is key as the energy is deposited over a short duration and a small volume relative to the chamber size. To increase reliability of spark ignition for larger rocket engines, the spark igniter has been placed in a smaller pre-chamber, which is known as an augmented spark igniter (ASI) [17, 18, 19].

The ASI operates on the principal of augmentation of the spark igniter with bi-propellants that are tightly controlled in both their mixture ratio and flowrate to produce a robust torch flame that is projected downstream into the engine chamber. Within the engine chamber, the ASI torch flame can readily ignite the flow of propellants from the engine injector. The spark igniter for the ASI has electrodes that can be separated by either ceramic substrate or by air. These two electrode configurations are referred to as surface-gap and air-gap, respectively [20, 21]. With an air-gap spark igniter, it may be preferred (and sometimes advantageous) to inject one reactant upstream of the electrodes to project the spark discharge downstream toward the non-premixed fuel-oxidizer mixture within the ASI chamber. Either reactant passing through the electrodes will act as an electrical insulator in its normal state. A sufficiently large voltage across the electrodes is required to initiate movement of charged particles between the electrodes, leading to a Townsend avalanche of free electrons and breakdown of the insulating gas medium. The breakdown voltage is related to the pressure-distance product (traditionally denoted by Pd with units of torr-cm) and is calculated by Paschen's curve for a uniform electric field between two parallel plate electrodes in quiescent

air. It is known that extrapolations from Paschen's curve are insufficient when used in practical applications for rocket ignition [22, 23], yet it has been the standard for estimating breakdown voltage [24]. Once ionized, the gas acts as a conductor and an electrical arc forms at a lower voltage so long as a large current is sustained. The plasma created from the spark discharge and subsequent arc is close in nature to an equilibrium plasma with a high neutral gas temperature, but low electron temperature [25]. Augmenting the spark discharge of rocket ignition devices in this manner has been referred to as a plasma assisted ignition (PAI) method [17].

Over the last twenty years, significant effort has been made to understand plasma assisted combustion (PAC) or PAI primarily utilizing both non-thermal and thermal plasmas. Parameters for combustion enhancement through plasmas occur through thermal, kinetic, or transport phenomena changes. Energy deposition to non-thermal plasmas is placed into electronic excitation, dissociation, ionization, and vibrational excitation, generating rapid pools of radicals and excited species without a significant temperature rise [25, 26]. Energy imparted to thermal plasmas, like spark discharges or laser-induced breakdowns, occurs over a large volume of the working fluid where the gas temperature increase accelerates reactions according to the Arrhenius law.

The first major spark ignition studies were in air-hydrocarbon mixtures to establish relations between ignition energy, flow range and regime, and spark duration and electrode spacing [27, 28, 29, 30, 31]. Subsequent efforts showed that while turbulence has a substantial impact on minimum ignition energy (MIE), turbulence has a minimal influence on the energy deposited by the spark [24, 32, 33]. Energy deposition is key to ignition and such information is valuable when considering the range and regime of anticipated flow (*Re* 1,000 – 100,000) through an air-gap igniter. Furthermore, the spark discharge within the annulus will be stretched in a similar manner to an arc between pronged electrodes in a wind tunnel or subject to buoyant forces. While MIE generally increases with flow velocity, a local minimum for MIE was found between 3-5 m/s for propane-air mixtures with 10-250 microsecond sparks [34]. Although these effects on MIE are studied for premixed gases, they are relevant by being a physical result of the spark elongating in the direction of flow, dispersing the energy discharged over a larger fluid volume [35].

In this work, microsecond spark discharges across annular air-gap electrodes were studied, where the working fluid is injected upstream of the air gap, which projects the electrical arc downstream from the spark gap. It is built upon prior work that focused on electrical characteristics of stagnant fluids [36] or, imaging of ignition kernels post-discharge [37, 38]. Past literature involved pronged electrodes with air-hydrocarbon mixtures, which have electrical input parameters and geometric shapes (e.g., cones, planes, prongs) comprehensively varied [37, 39, 40, 41, 42, 43]. They provide a foundation for spark discharges in stagnant conditions and the fundamental understanding of the ignition or electrical phenomena, yet do not represent the high-speed gaseous flow present in annular electrode, i.e., augmented spark igniters. In addition, pronged electrodes are obtrusive to the flow and then subject to corrosion within the combustion chamber [21], highlighting the need to investigate noninvasive spark igniter designs.

The spark discharges presented in the current work consist of gaseous oxygen flowing through the spark igniter electrodes, as inspired by current augmented spark igniter design [17]. Studies of spark kernel formation in moving flow are commonly carried out using either pronged electrodes in crossflow or a surface-gap electrode in crossflow. Kernel formation has been characterized for pronged electrodes protruding into uniform crossflow (33 m/s) for short duration discharges (<1 μs) both numerically and experimentally [44]. For stratified crossflows of fuel and air, the entrainment of the surrounding fluid increased the kernel volume thus decreasing temperatures. As pointed out by Sforzo et al. [45], fuel must be present near the igniter to ensure reliable ignition. Later work focused on spark kernel travel and its thermal impact by measuring temperatures in high-power spark discharges (10 J per pulse) in an air crossflow (16 m/s) with sunken-fire igniters [46]. Most of these studies do not apply directly to the case of a plasma igniter that involves a pressure drop across a planar or annular gap. This work explores the behavior of an annular gap spark igniter flowing oxygen through the gap. In the following sections, we outline experimental methods used to create, measure, and observe spark discharges; experimental results for discharge properties; discussion of the results, discrepancies from theory, hypotheses on the cause of discharge property trends, and variation in measurements due to spark quenching. We conclude with a summary of the results and their importance when considered by designers of relevant ignition devices.

## EXPERIMENTAL METHODS

### FACILITY AND SPARK DISCHARGE SYSTEM

An annular spark gap was formed by a nickel alloy electrode (rod) and a concentric stainless-steel cap (cylinder) as shown in Figure 7. Gaseous oxygen was injected into a cavity upstream of the spark gap filling a pre-spark chamber. To orient the reader, a sample schlieren image is shown in Figure 7c with oxygen flowing into quiescent air. Full details of high-speed imaging are discussed in *Schlieren Imaging*. Sparks were generated using a Champion Aerospace CH31887-3 spark igniter connected to a capacitive exciter powered by a PWS4305 DC power supply set to 28 V and 3 A. Two exciter models were used. One discharged with alternating current and the other discharged with direct current: Champion Aerospace SK927123 (bipolar exciter, 25 kV peak output, 83 Hz pulse rate) and Unison (unipolar exciter, 20 kV peak output, 200 Hz pulse rate). A National Instruments cRIO-9064 was used to trigger the power supply, collect data from all pressure transducers and thermocouples, and trigger a high-speed camera. Electrical measurements were taken with a model 410 Pearson current monitor (20 ns rise time with a 50 Ω termination, thus sensitivity decreased by a factor of two), high voltage probe (1 MΩ termination), and recorded by a 12-bit oscilloscope. Spatial resolution was 65.5 V/bit (span of 16 kV), and 0.3125 A/bit (span of 160 A). Uncertainty for individual measurements is one-half of the spatial resolution (viz. ±32.8 V/bit and ±0.156 A/bit). Resulting Kline-McClintock calculations for power, energy, and resistance uncertainty are 16% (nearly identical uncertainties result from voltage being the substantially more influential than current). Temporal resolution was 1 ns over a 100 μs duration, and the triggering channel was set to +800 V high voltage lead. Approximately 1,000 traces were time-averaged for each data point, creating statistically significant mean results. The mean standard deviation for energy was ±5.5 mJ across all conditions, translating to a 95% C.I. of 10.1 mJ for the margin of error. This equates to 9% uncertainty for the lowest energy measurement and 4.6% for the highest energy measurement.

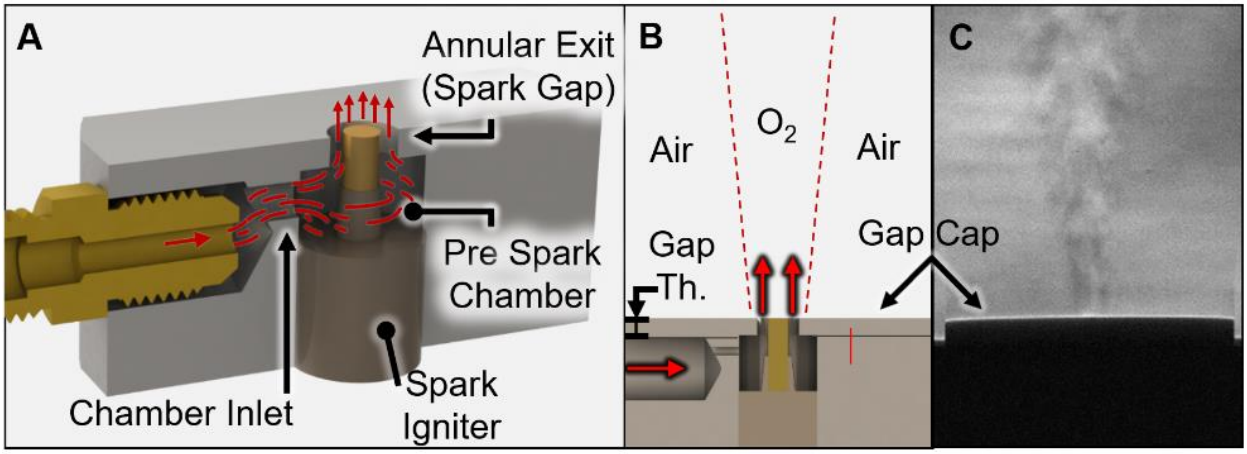


Figure 7 – (a) Schematic of igniter assembly and juxtaposition of (b) an assembly schematic and (c) a schlieren image with flowing oxygen.

The gas-handling system developed for this experiment (seen in Figure 8), described previously [47, 48], allows delivery of pure oxygen at varying pressures and flow rates through the spark gap. The spark gap distance was varied between 0.5 - 2.3 mm as outlined in Table 1. Pressure transducers (PX603 series) were accurate to ±0.4% full scale, therefore ±5 kPa (±41.3 torr) upstream of the venturi and ±0.5 kPa (±4.13 torr) downstream. Exposed K-type thermocouples were used for temperature measurements and accurate to ±2.2℃ (approximately 1%). For tests at high flow rates, pressure differentials across the venturi dropped below 0.57, indicating choked flow. The mass flow was regulated by a choked flow venturi (1.32 $mm^2$ area throat), which had nominal pressure ratios ($P_1/P_2$) between 0.27-0.32 for all tests. The pressure ($P_1$) upstream of the choked flow venturi controlled the mass flow rate.

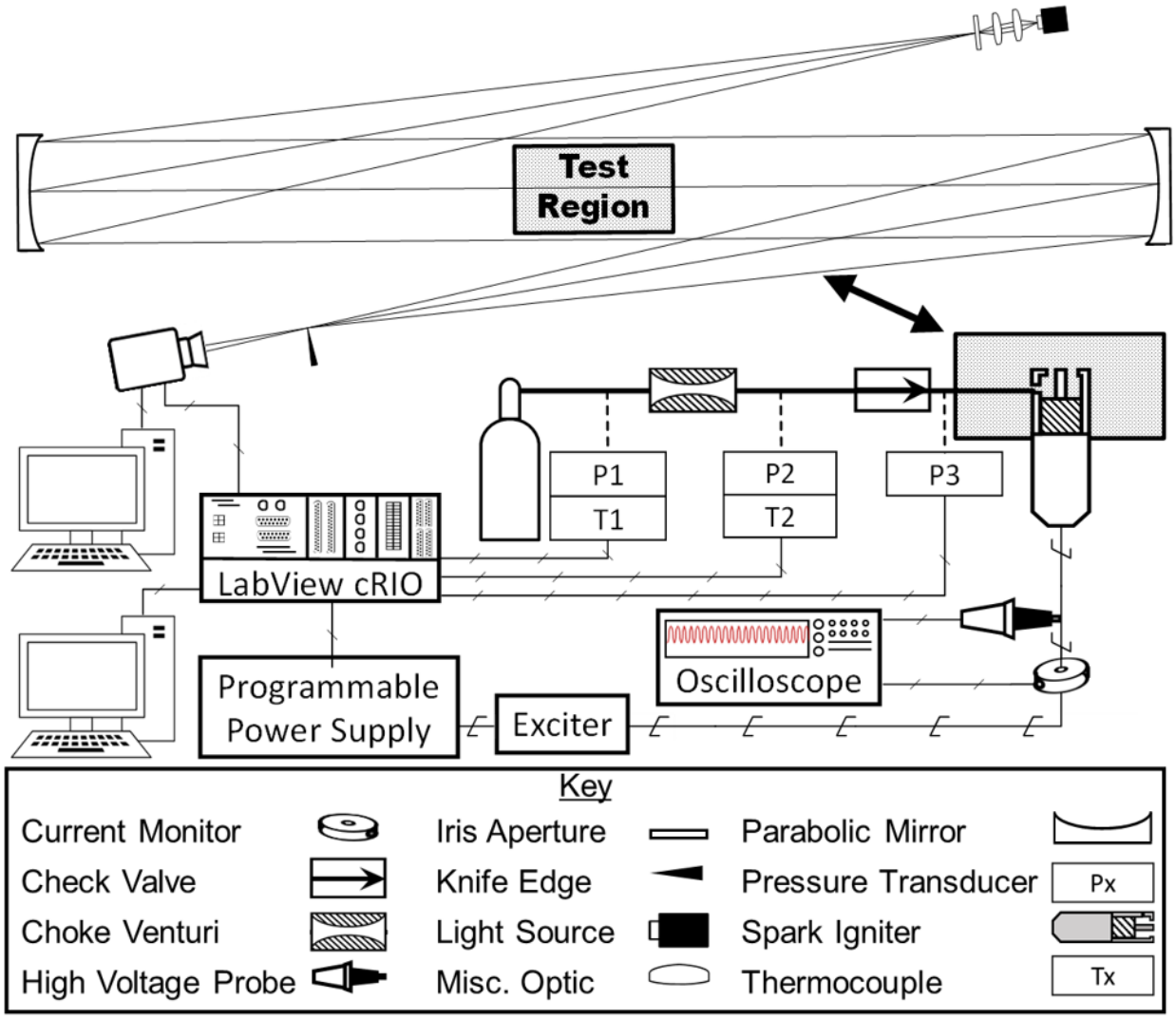


Figure 8 – Experimental setup for Schlieren imaging, high voltage, and fluid property measurements for oxygen flow through an annular spark gap.

Table 1 – Spark gap geometries

| Spark Gap | Outer Dia. [mm] | Inner Dia. [mm] | Width [mm] | Area [mm$^2$] | Th./Width [L/D] |
|---|---|---|---|---|---|
| 1 | 3.43 | 2.39 | 0.52 | 4.8 | 6.1 |
| 2 | 4.00 | 2.39 | 0.80 | 8.0 | 4.0 |
| 3 | 4.50 | 2.39 | 1.05 | 11 | 3.0 |
| 4 | 4.98 | 2.39 | 1.30 | 15 | 2.5 |
| 5 | 6.02 | 2.39 | 1.82 | 24 | 1.7 |
| 6 | 7.04 | 2.39 | 2.32 | 34 | 1.4 |

## VOLTAGE, CURRENT AND RESISTANCE MEASUREMENT, AND IDENTIFICATION OF QUENCHING EVENTS

Samples traces of the transient current (*I*), voltage (*V*), supplied energy (*E*), and channel resistance (Ω) are shown in Figure 9 and Figure 10. The results shown are for a spark gap of 2.32 mm at a 1,500 kPa nominal supply pressure (2,600 torr-cm). Voltage and current are directly measured, then are used to calculate channel resistance as shown by Eq (1) and both instantaneous power and supplied energy as shown within Eq (2).

$$R(t) = V(t)/I(t) \tag{1}$$

$$E_{supplied} = \int V(t)\, I(t)\, dt \tag{2}$$

Spark duration was calculated as a function of instantaneous power and current. The start of the discharge event was marked by the sudden fall of voltage, and the end of the discharge was marked by the last instance when 1 W and 1 A were measured simultaneously. The discharges shown in the figures below last approximately 60 μs and 30 μs for the unipolar and bipolar exciters respectively. The underdamped oscillation over the first few microseconds for each system is due to a combination of the exciter circuitry and channel resistance. Oscillations nominally occur at 9 MHz for the unipolar exciter and 10 MHz for the bipolar exciter. These oscillations were observed for all cases with variations of ±1 <MHz from nominal.

Spark discharges are comprised of multiple phases where energy is released to the medium [49, 50] with energy deposition throughout the discharge. Energy from the spark is deposited first by ionization of the gas within the channel (breakdown event). The ionized species then act as a conduit for the primary energy release (arc discharge) from the exciter. The breakdown voltage ($V_b$) is the peak voltage measured when the spark-gap channel is ionized. The unipolar exciter ionizes the channel once before fully discharging its energy. The bipolar exciter ionizes the channel before alternating current flow. The first ionization event ($1^{st}$ $V_b$) requires the highest breakdown voltage and is the value referenced for comparison to the unipolar exciter. Subsequent ionizations occur when the current flow reverses (approximately every 5 μs) and are labeled in Figure 10 as $2^{nd}$, $3^{rd}$, $4^{th}$, $5^{th}$. A significant number of ionized species is still present during this process and lower electric potential is required to ionize the channel. Following ionization, the sustaining

voltage required for discharge ranged between 50 - 300 V for both exciters. The majority of energy was added to the channel following the breakdown event during discharge for both exciters and correlates to the rise (and fall) of current traces. For the unipolar exciter, only a single overall discharge was observed and caused a steady rise of cumulative energy in two tiers from the breakdown phase and the arc discharge phase [36]. In contrast, the bipolar exciter had multiple discrete discharge phases that lead to a multi-tiered increase of cumulative energy. Peaks of the sustaining current follow breakdown and are labeled in Figure 10.

During spark quenching, the voltage rise was the similar to a non-quenched test. However, once the voltage limit of circuitry was reached without a breakdown event, the voltage would drop, potentially oscillating as observed for non-quenched tests. The electrical ringing observed would then create a "false signal." The voltage signal alone was therefore an unreliable indicator to establish if a spark discharged or if a spark quenched. In turn, quenching was identified by analyzing a combination of current and channel resistance. The bipolar exciter was quenched when the mean resistance over the measurement was greater than 3 kΩ. The absolute value was calculated for all data points to account for the oscillating signal. The unipolar exciter was quenched when the mean amperage was less than 0.02 A. Transitionary cases did exist for both exciters where the spark was not quenched, did not discharge completely, and had multiple breakdown events to ionize the channel. These were less than 0.1% of the bipolar cases, less than 3.7% of the unipolar cases. As the energy deposition to the flow was less than 10% of the mean energies recorded, these events were categorized as quenched. For the bipolar exciter, these partially quenched tests had mean channel resistances between 1-3 kΩ whereas the channel resistance for the unipolar cases was between 400-700 Ω with a mean amperage less than 1 A.

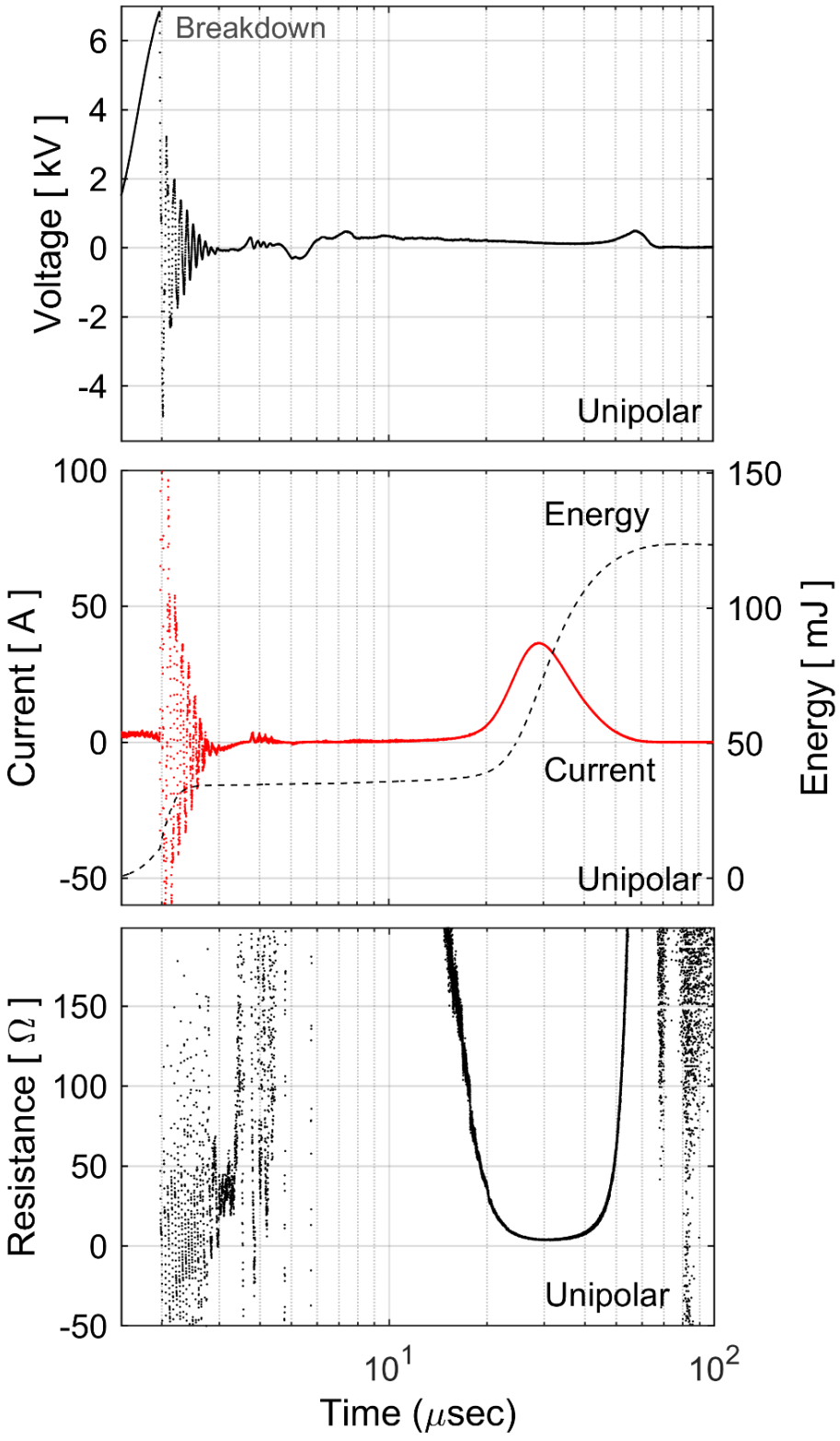


Figure 9 – Sample traces of voltage (V), current (I), energy (E), and channel resistance (Ω) measurements for the unipolar exciter at 2,600 torr-cm (spark gap of 2.32 mm at a 1,500 kPa nominal supply pressure).

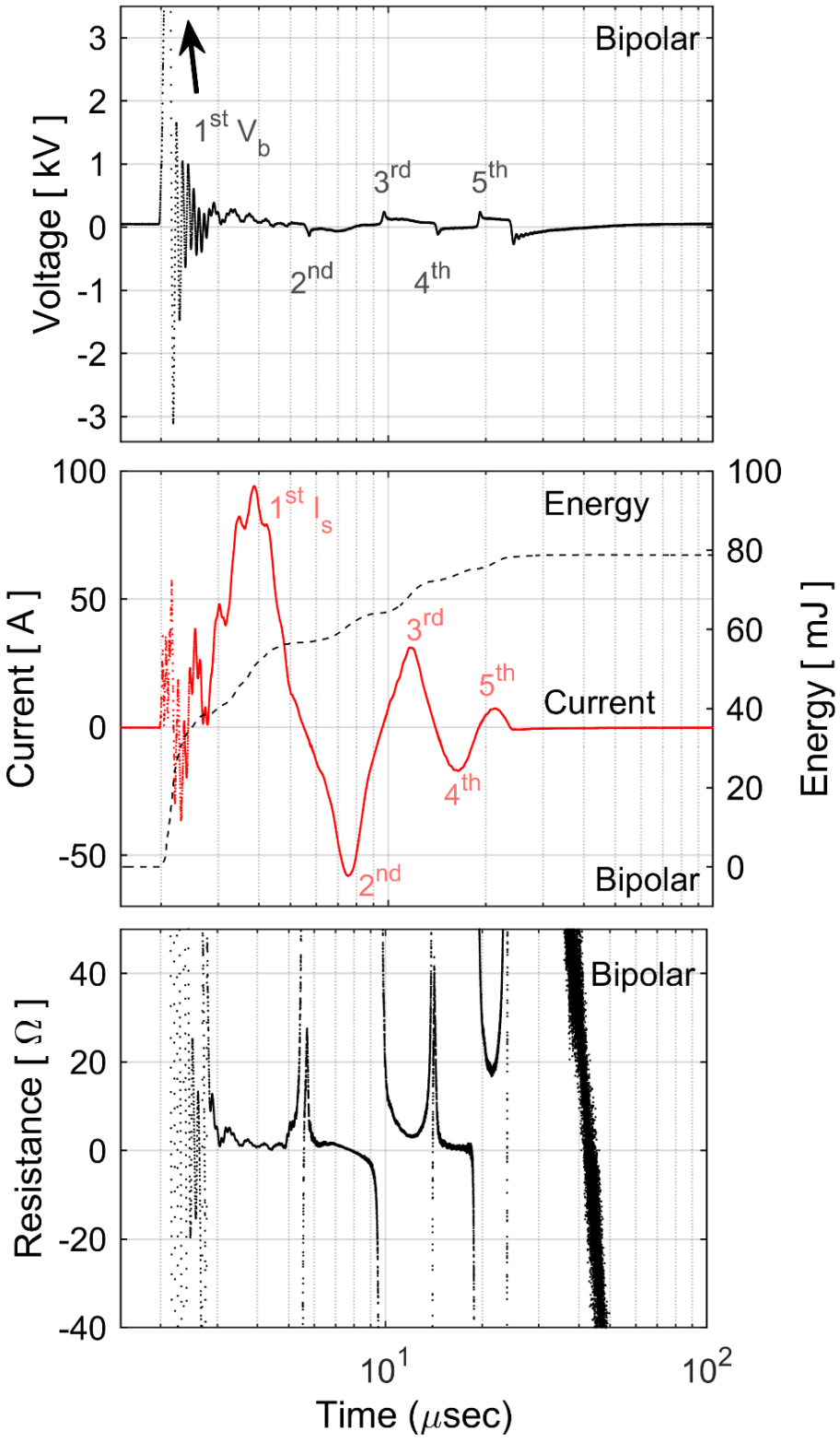


Figure 10 – Sample traces of voltage (V), current (I), energy (E), and channel resistance (Ω) measurements for the bipolar exciter at 2,600 torr-cm (spark gap of 2.32 mm at a 1,500 kPa nominal supply pressure).

### SCHLIEREN IMAGING

Schlieren imaging of the electrical discharge and subsequent exhaust plumes were taken using the experimental setup shown in Figure 8 with a typical schlieren image shown in Figure 7c. The continuous-wave schlieren light source was a UHP High Intensity Light Source ILP-2, which passed through a liquid light-guide cable and was expanded to a 15-degree beam angle using a 2-lens UV-Spot quartz glass optic. The light was passed through a condenser array with two 50 mm diameter, f/2 achromats, with the second achromat focusing the light onto a horizontal slit. An iris aperture was used to crop the light before focusing onto the first of two f/10 203 mm diameter parabolic mirrors spaced 2.4 m apart. The first parabolic mirror served to collimate the light through the test region, while the second mirror focused the light onto a knife edge just upstream of the camera. The first mirror captured 68% of the incoming light, which was sufficient to resolve an image with one microsecond exposure time at 100,000 FPS on a Phantom v310 high-speed camera using a Sigma aspherical 170-500 mm f/5-f/6.3 lens. The total image size was 160 x 127 pixels at 4.1 pixels per mm with a spatial resolution of 245 μm in the gas flow field.

High-speed schlieren images captured during the bipolar exciter experiments were processed with image processing techniques previously discussed [48]. Schlieren data associated with the unipolar exciter were lost due to hardware failure unrelated to data collection. Approximately 1,000 spark discharge attempts were recorded and an image-based trigger was used to determine the start of spark events that were not quenched. The subsequent plume development was determined using a subpixel edge detection method [51] for each spark event. Transient data was spatially averaged for a given test condition. The weighted centroid of the time-integrated plumes was used to determine plume velocity into quiescent air.

## EXPERIMENTAL RESULTS

Spark quenching was observed for multiple testing conditions. Quenching occurs when there is insufficient potential difference or voltage to ionize the medium within the spark gap. With no electron avalanche, there is neither a conductive plasma between the electrodes nor energy deposited to the media. Spark quenching is determined by a lack of current (effectively infinite resistance). Quenching increases

when the pressure-distance product increases as shown in Figure 11. The percentage of sparks quenched rapidly increases as the pressure-distance product surpasses 500 torr-cm for the unipolar exciter. In contrast, the bipolar exciter exhibits virtually no quenching for the smallest spark gap (0.5 mm), excessive quenching for intermediate spark-gap distances (0.8 - 1.3 mm) beyond 1000 torr-cm, and slight quenching for all other cases.

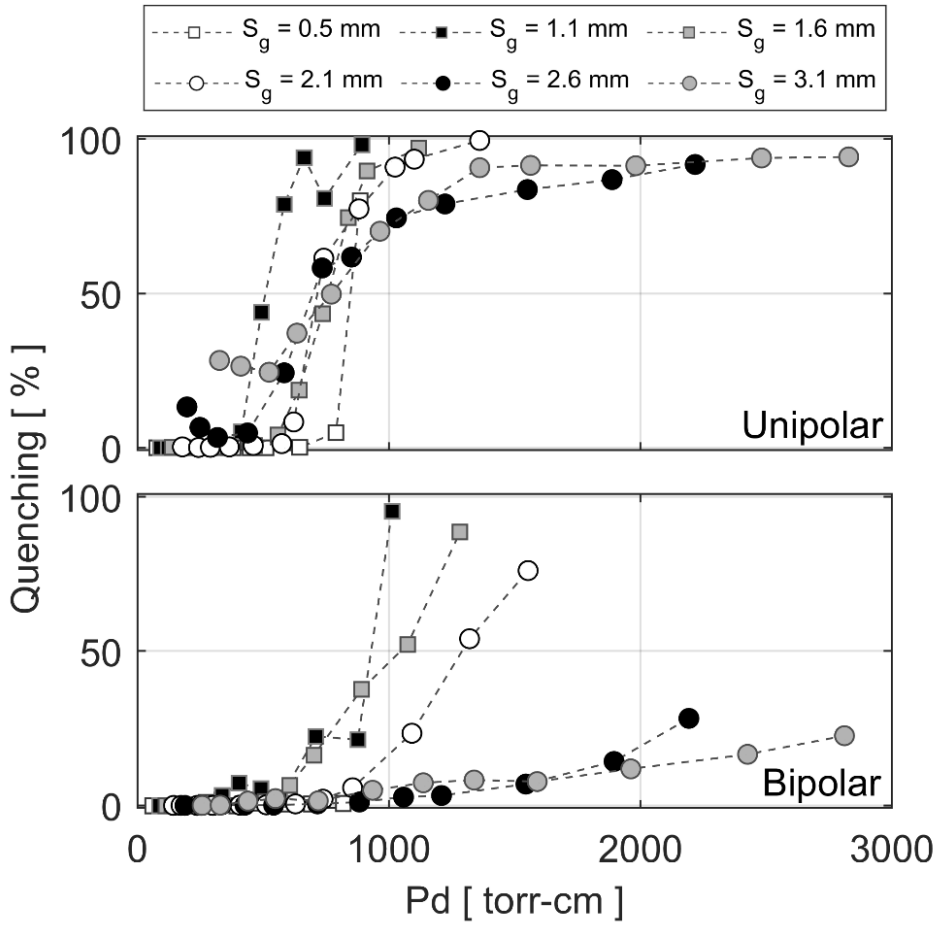


Figure 11 – Percent of spark discharges that quenched for both exciters.

Figure 12 and Figure 13 show results for cumulative energy supplied and breakdown voltage respectively, but have juxtaposed results where quenched spark attempts were not filtered from the dataset. The unfiltered results are analogous to those observed from a default hardware integration (i.e., energy calculations with mean signals); the mean result can be depressed due to quenching where no current is

measured or artificially raised due to electrical ringing. For the unipolar exciter, the unfiltered values for energy decay rapidly after 500 torr-cm and reach a floor near 40 mJ per spark discharge. The bipolar exciter shows an inverse behavior, where the unfiltered measurements of energy increases with increased quenching. For both exciters, the breakdown voltage rises with increased quenching and rises significantly more for the bipolar exciter across moderate spark gaps (0.8 - 1.3 mm).

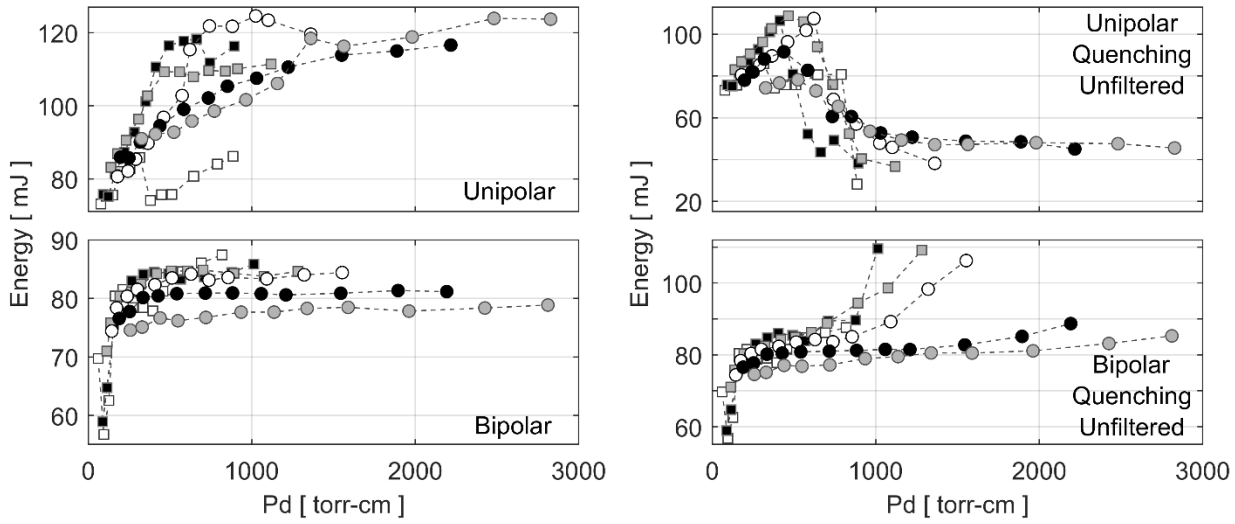


Figure 12 – Cumulative energy supplied versus the pressure-distance product when quenched spark attempts are filtered from results (left) and when quenching is not removed (right). See Figure 5 legend.

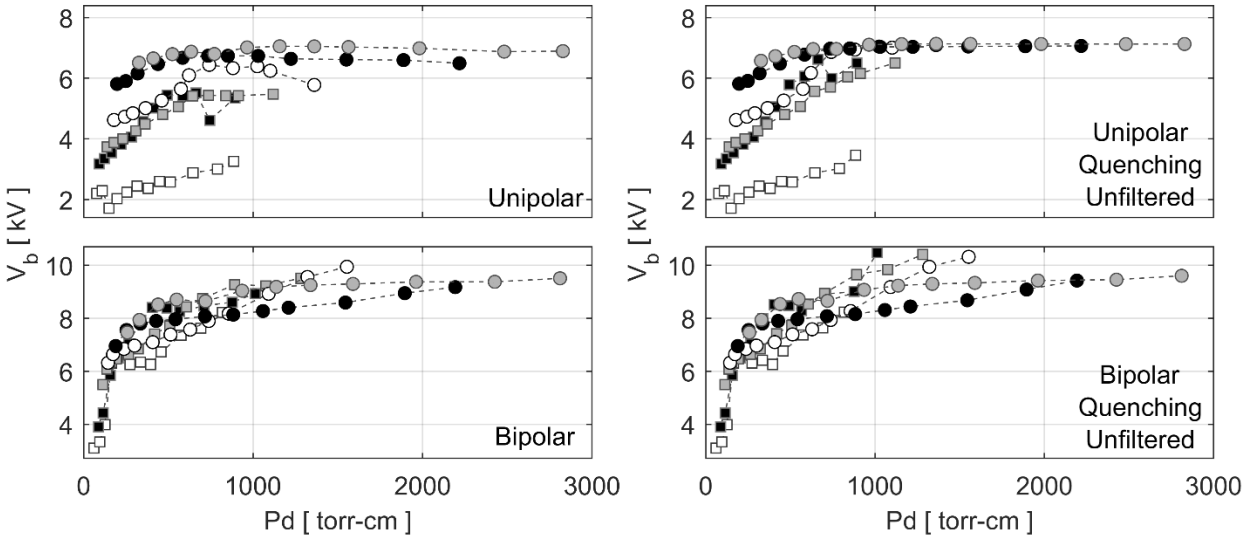


Figure 13 – Breakdown voltage versus the pressure-distance product when quenched spark attempts are filtered from results (left) and when quenching is not removed (right). See Figure 5 legend.

Electrical characteristics of spark discharges are accurately examined after quenched events are filtered. Measurements of the breakdown voltage are compared to the pressure-distance product and show a generally positive correlation in Figure 14. The bipolar exciter reaches higher breakdown voltages for the same pressure-distance products than the unipolar exciter in nearly all cases, and both datasets deviate from Townsend theory (Paschen's law) requiring lower breakdown voltages than predicted. Outliers are present for the unipolar dataset, as shown by gray-filled circles in Figure 14 and Figure 15, with the source of the deviation discussed later in this manuscript. The cumulative energy for each spark is shown in Figure 15 with 95% confidence intervals (two standard deviations) marked for select points. With the exception of outliers for the unipolar dataset (grey filled markers), uncertainty bars for the independent variables were negligible, overlapping the markers, and are thus excluded. The energy of spark discharges increases and plateaus for both exciters as the pressure-distance product increases. The bipolar exciter plateaus almost immediately near 200 torr-cm whereas the unipolar exciter levels out after a quasi-linear rise in energy up to 1200 torr-cm. Higher pressure-distance products intuitively are more turbulent (higher velocity and spark-gap width, thus higher Re) and the positive relation between energy and Reynolds number follows studies of flammable mixtures [27, 29].

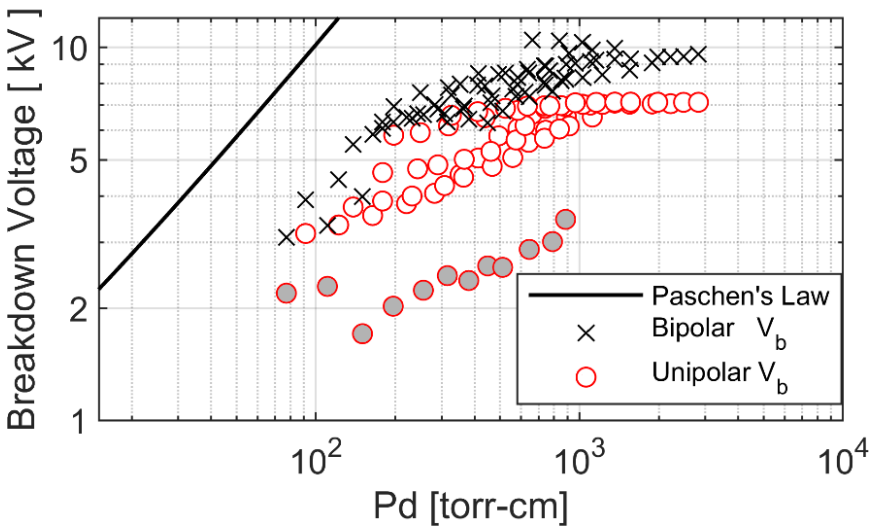


Figure 14 – Breakdown voltage versus the pressure-distance product using Townsend theory (Paschen's Law) and for experimental results of both exciter types. Outliers for the unipolar dataset are denoted by gray filled markers.

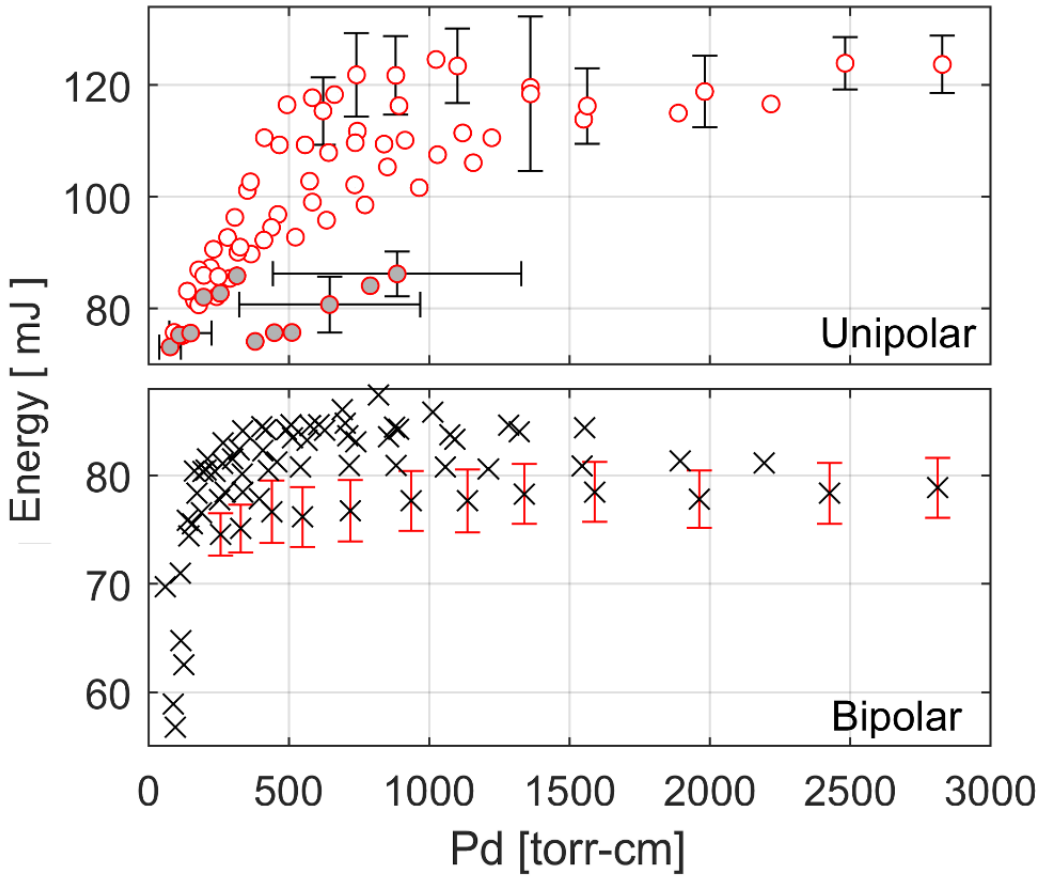


Figure 15 – Cumulative energy supplied versus the pressure-distance product. Outliers for the unipolar dataset are denoted by gray filled markers.

Mean values of the channel resistance during discharge (at each particular sustaining voltage) are determined. The resistance values calculated are only for active spark-discharge events (i.e., with quenching filtered out) with results for both exciters are shown in Figure 16. The resistance is graphed against the traditional pressure-distance product and against the pressure-distance quotient — the latter of which shows convergence of the dependent variable, outliers notwithstanding. There is a positive relation between the pressure and channel resistance as shown in both sets of plots (left and right), whereas the channel resistance correlates inversely with increasing gap-distance. This correlation is observed for both the alternating current and direct current discharges (top and bottom). For the bipolar exciter, where multiple breakdown events occur, only positive-current discharges (odd numbered) are shown.

The convergence of dependent variables by using the **pressure-distance quotient** instead of the traditional pressure-distance product is found not only for channel resistance, but also spark duration. The discharge duration decreases with pressure as shown in Figure 17 for both plot sets (left and right) and for both exciters (bipolar, top; unipolar, bottom). However, similar to the channel resistance, the discharge time decreases as the spark-gap width increases as observed on the right plots of Figure 17, once more with outliers notwithstanding.

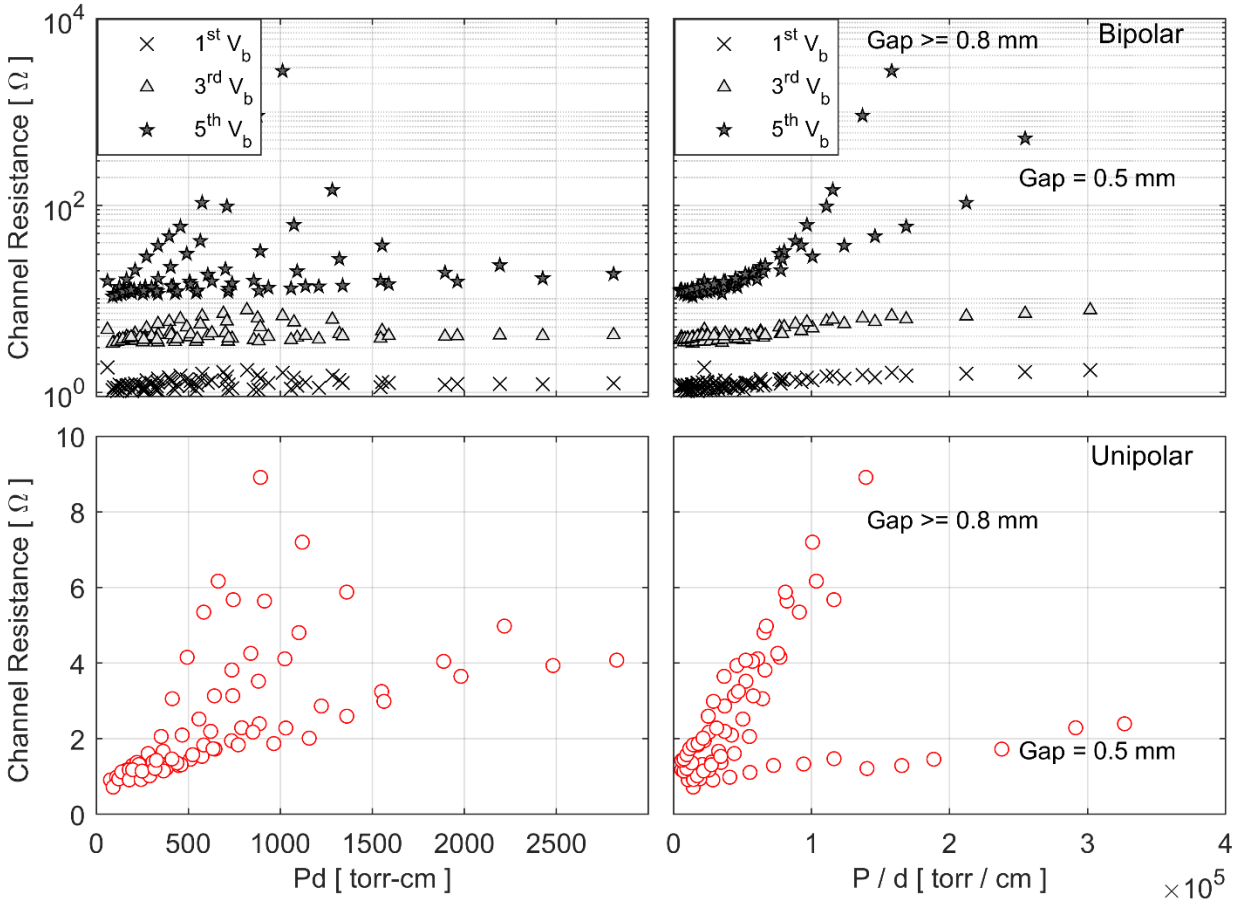


Figure 16 – Channel resistance versus the pressure-distance product (left) and pressure-distance quotient (right) for both exciters during the spark duration. For the bipolar exciter (top half), channel resistances are shown sustaining phases with positive-current.

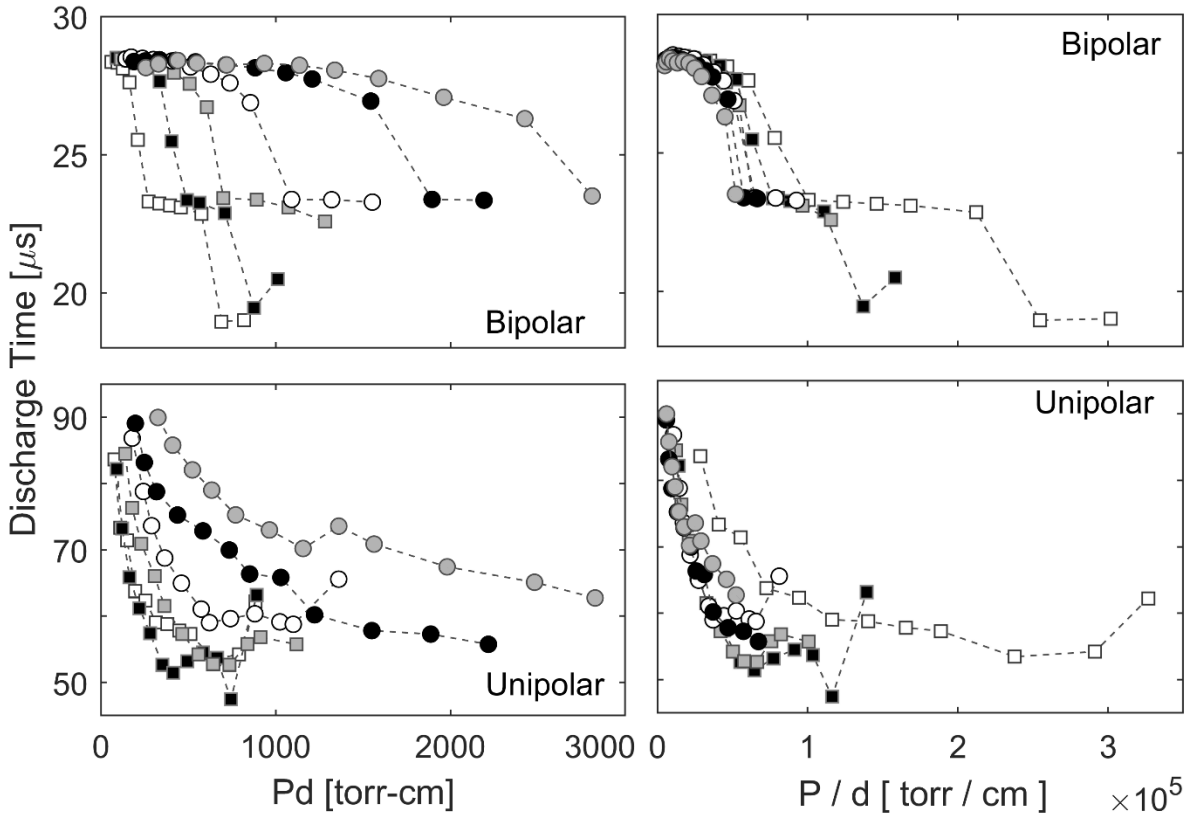


Figure 17 – Spark-discharge duration versus the pressure-distance product (left) and pressure-distance quotient (right) for the bipolar exciter (top) and unipolar exciter (bottom). See Figure 5 legend.

## DISCUSSION

Discrepancies from the theoretical basis of Paschen's curve are often due to electrode geometry or exceeding the pressure-distance product for which it was designed. Even for a simple, planar geometry Paschen's law is only applicable up to roughly 2000 torr-cm [49]. In addition, this work uses a cylindrical nickel electrode with a concentric stainless-steel grounding surface instead of two, parallel-plate electrodes. The inner electrode and outer spark gap surface both have 90-degree angled edges, which lead to electrical charge concentration (singularities) [52]. These surfaces not only have uneven distributions of electrical charge, but also oxidize during the discharge. Over time pitting occurs, which is caused by evaporation, oxide removal, particle ejection, and sputtering [53]. Erosion and increased resistance lead to the electrical arcs occurring at multiple radial and longitudinal locations on the electrode with the passage of time. The

complexity of charge concentrations, added resistances, and uneven pressure distributions within the spark gap led to deviation from Townsend theory.

While results are expected to deviate from theory, a set of outliers are clearly present in Figure 14 and Figure 15 for breakdown voltage and discharge energy respectively. The error is attributed to a geometric change of the central electrode when testing the 0.5 mm spark gap for the unipolar exciter. The tip of the electrode deformed, shortening the spark gap on one side and lengthening it on another. This undoubtedly caused variation in results and the error in distance is estimated to be near 50%. This does not account for the non-uniform pressure field, which would also cause variation from the expected results. The deviation is only observed when using a pressure-distance combination as the independent variable. For example, Figure 18 shows the relation between breakdown voltage and energy discharged. As there are no obvious outliers, it is presumed that the exciter was functioning correctly and that the breakdown voltages should occur at similar pressure distance products. It is expected that the outliers would better align if the independent variable was calculated using a smaller gap distance (consequently shifting outliers toward the y-axis in Figures 16 and 17) to correct for the electrode deformity.

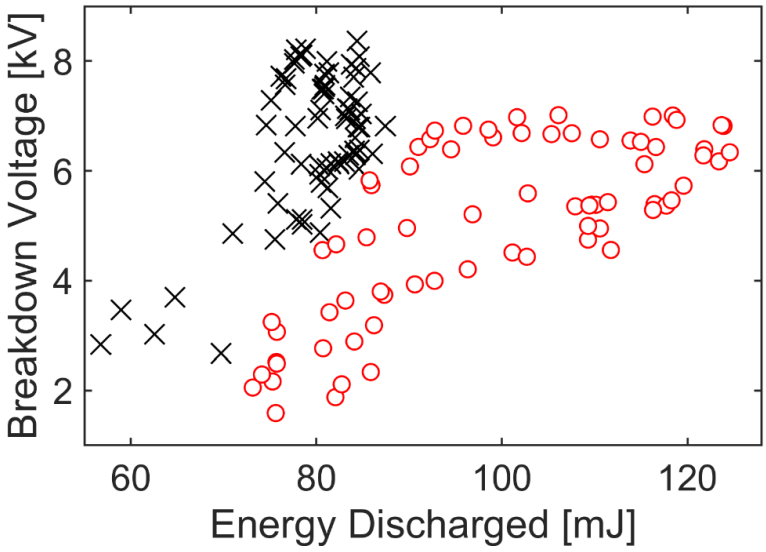


Figure 18 – Breakdown voltage versus energy discharged for the bipolar (black “x” markers) and unipolar (red “o” markers) exciters.

With this assessment of the outlying data, results generally trend well for both the unipolar and bipolar exciters (reference Figure 14). The agreement with Paschen's law for annular air-gap electrodes leaves room for improvement. However, results here are similar to those of prior work by Ballal and Lefebvre [24] who implied the deviation in results is largely caused by the nonuniformity of the electric field, which is affirmed in other literature as well [22]. Results for the bipolar exciter are in closer agreement to Paschen's curve than initial efforts [48] by over an order of magnitude. This is attributed to widening the chamber inlet (see Figure 7) to the nominal tube diameter to prevent a choked flow restriction and a major pressure loss prior to reaching the spark gap. Even so, the pressure within the gap is expected to be lower than the pressure measured. It likely lies closer to a mean value with atmospheric conditions due to the major losses across the spark gap.

There is a hardware limitation for each exciter which is best shown by spark quenching in Figure 11. The ionization voltage provided by each exciter limits the peak voltage. Consequently, conditions at the spark gap are not always permissive of an electrical arc and result in the discharge being quenched. Quenching impacts measurements of voltage, current, and all variables dependent on their values (i.e., power, energy, resistance, etc.). In addition, the impacts vary depending on exciter circuitry. For the bipolar exciter used, quenching results in the high voltage pulse reflecting between the electrode and the exciter, consequently across the measurement probes. The electrical ring results in an erroneous, artificially high breakdown voltage (a misnomer as no breakdown occurs) as well as erroneous spark-discharge energies. These do not represent the physical values from individual sparks. Removal of quenching data shows the actual energy delivered per spark discharge, which is more relevant to the ignition of a combustible gas mixture.

The most intriguing result is the convergence of multiple independent variables plotted against the pressure-distance quotient: channel resistance and discharge time. In previous work, the spark duration tended to decrease with rising velocity [29, 30, 33], which is also observed for results here as shown by Figure 19. The development of the exhaust plume was tracked using schlieren imaging (see Figure 20) and velocity was calculated using a weight-averaged centroid. Full details on image tracking and the relation of

plume velocity to the flow velocity as calculated by analytic relations are discussed in previous efforts [47, 48]. As this and prior work show that spark duration and bulk-flow velocity are related, the plume velocity was then compared to the pressure-distance combinations as shown in Figure 21. Once more, the results converge for the pressure-distance quotient and leads to a question of correlation versus causation. Both spark duration and channel resistance are electrical properties, whereas the flow velocity is fluid dynamic. Each of these variables are interrelated through the pressure-distance quotient. The bulk-flow velocity is unlikely to be affected by the spark duration and channel resistance (with the assumption that the volumetric expansion of gas is negligible relative to inertial forces). In addition, shrinking the area of the spark gap while maintaining the same supply pressure will increase the velocity for incompressible flows. For compressible flow, which accounts for most results here, a vena contracta forms within the spark gap creating an artificial nozzle to accelerate the flow. Increasing flow velocity increases flow separation as the gas enters the spark gap, shrinking the nozzle and accelerating flow and creating the same result of higher velocities with smaller spark gaps. Under these assumptions, increasing bulk-flow velocity is the cause for the decrease of spark duration (shown here and similarly in literature) and channel resistance (shown here).

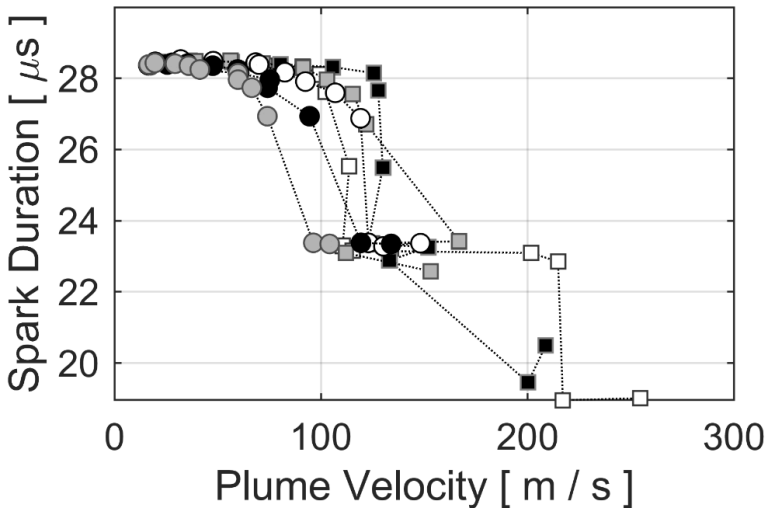


Figure 19 – Spark duration versus the plume velocity for the bipolar exciter. See Figure 11 legend.

The increase in channel resistance is hypothesized to stem from the electrical arc stretching as the flow carries ionized particles downstream. Due to boundary layer effects and highly turbulent flow, the shape of the electrical arc is anticipated to resemble a U-shape as shown in prior work [29] instead of a parabola that

may result from fully-developed laminar flow. The bands of resistance shown in Figure 16 for the bipolar exciter are products of separate breakdown events. The lowest resistance occurs during the discharge (i.e., sustaining) phase that follows the initial breakdown event ($1^{st}$ $V_b$) and rises for subsequent ionizing events. Only the positive-current sustaining phase (odd numbered) are shown in Figure 16. Negative-current discharges have inherently different properties, shown in Figure 10, as the electric field is dissimilar across the same geometry. The sustaining voltage remains fairly consistent during the succeeding discharges whereas the current flow is noticeably lower due to an increased resistance. Successive breakdown events occur at lower voltages due to the presence of ionized species from the previous discharge. The reduced voltage ionizes a lower number of molecules to electrically bridge the channel, which consequently leads to an increase in resistance for the following discharge.

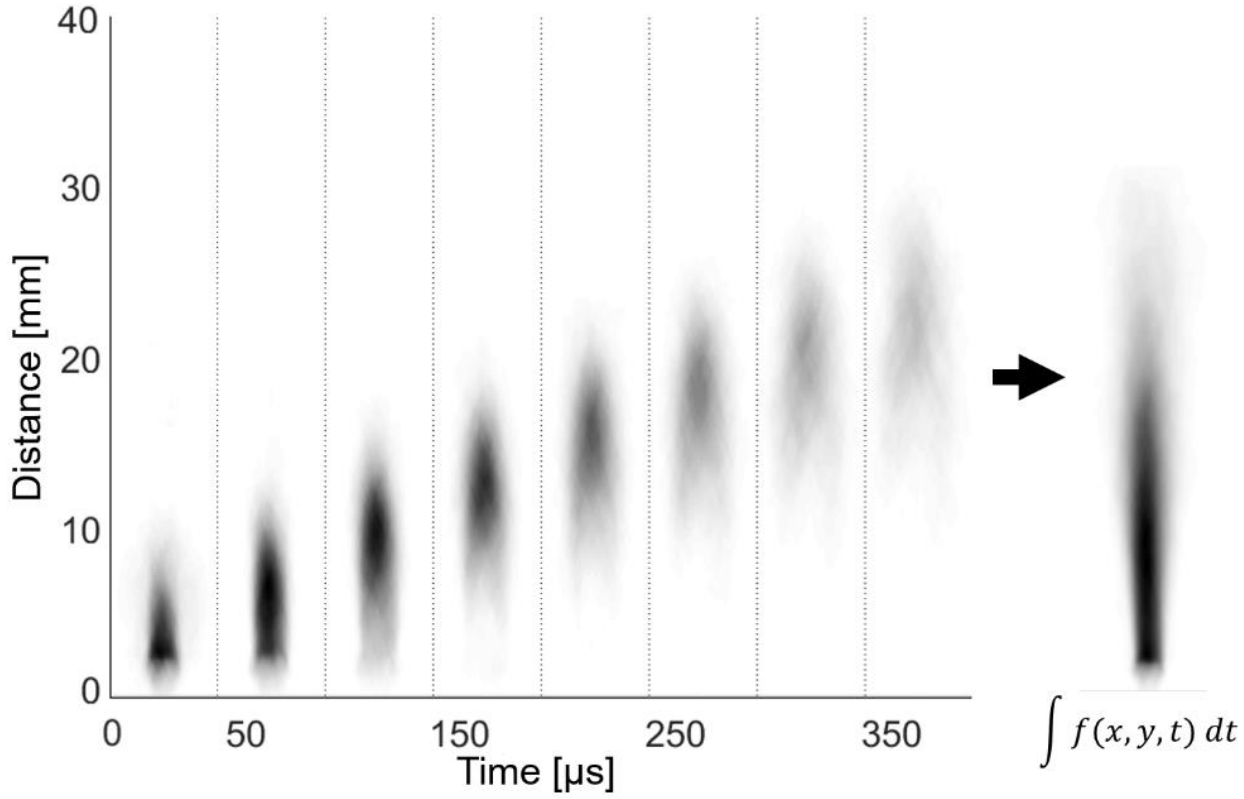


Figure 20 – Sample frames of an exhaust cloud for a 1.3 mm gap at 300 kPa, and result of a temporal integral for the bipolar exciter

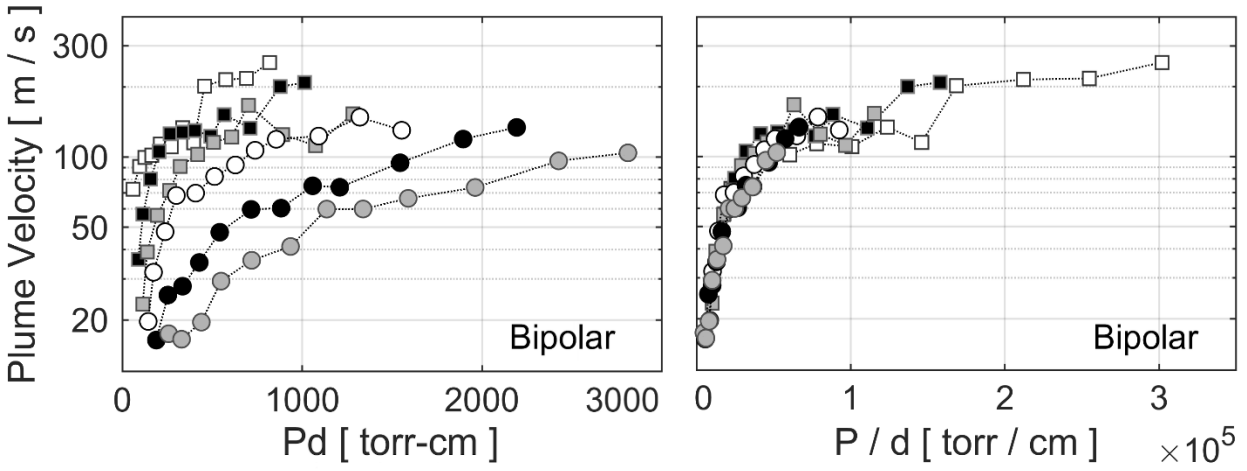


Figure 21 – Plume velocity versus the pressure-distance product (left) and versus the pressure distance quotient (right) for the bipolar exciter. See Figure 11 legend.

The penetration of the electrical arc and the exhaust plume are equally important to the ignition event. Arc penetration was calculated by multiplying the spark duration and flow velocity for the bipolar exciter with results shown in Figure 22. Convergence of the data is once again observed for the pressure-distance quotient. A positive relation between the arc penetration and rising pressure is observed, while a negative relation exists between arc penetration and rising spark-gap width. The spark gap thickness was 3.2 mm. If it is assumed that the spark formed at the lowest point possible within the spark gap, the arc penetration only exceeded the gap thickness for higher flowrates with smaller spark-gap widths. Similar results are hypothesized for the unipolar exciter under the same flow conditions. The sparks from the unipolar exciter last at least twice as long and the arc penetration into the flow should scale linearly.

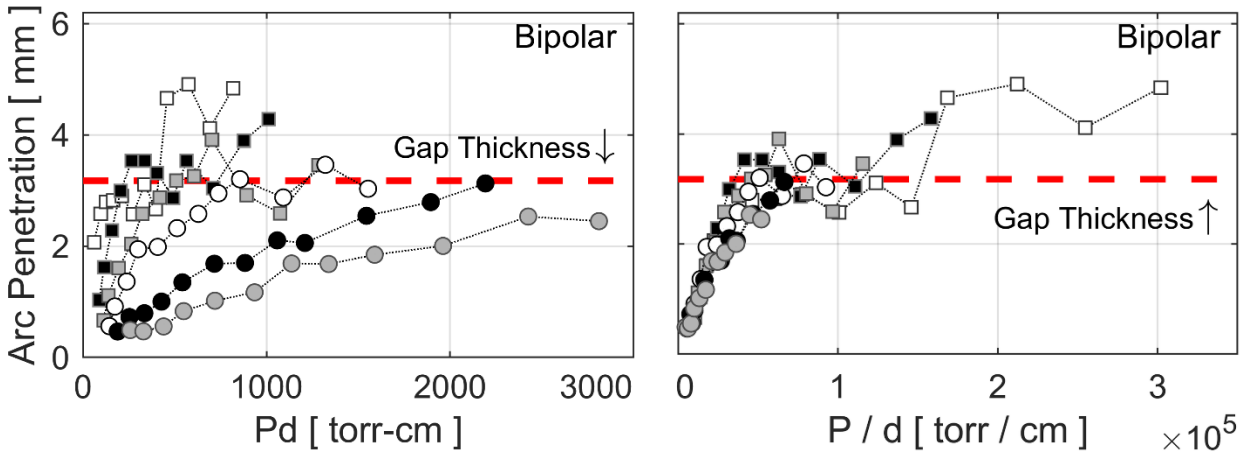


Figure 22 – Arc penetration versus the pressure-distance product (left) and versus the pressure distance quotient (right) for the bipolar exciter. See Figure 11 legend.

Time-averaged results for the spatiotemporal development of the exhaust plume are shown in Figure 23, with the method for calculating the temporal integral illustrated in Figure 20. The processing method relied on an image-based trigger (see reference [48]), and consequently results are normalized to the number of spark events captured, not attempted. In other words, the results of Figure 23 do not include the effects of quenching. An engineer interested in ignition effectiveness should reference both the development of the plume and the quenching limits of their hardware (Figure 11 for this work). No clear and consistent trend is observed for the development of the exhaust plume. A general increase in plume size is observed for increasing spark gaps, but that trend is less apparent at high pressures (i.e., velocities). Lastly, transient exhaust plumes showed a cylindrical starting shape that was dissipated from the higher velocity gases behind it. Experimental studies with larger spark gaps, stronger and faster sparks, and accompanying simulation results [31] have shown similar behaviors and discuss the shape eventually transforming to a toroidal form.

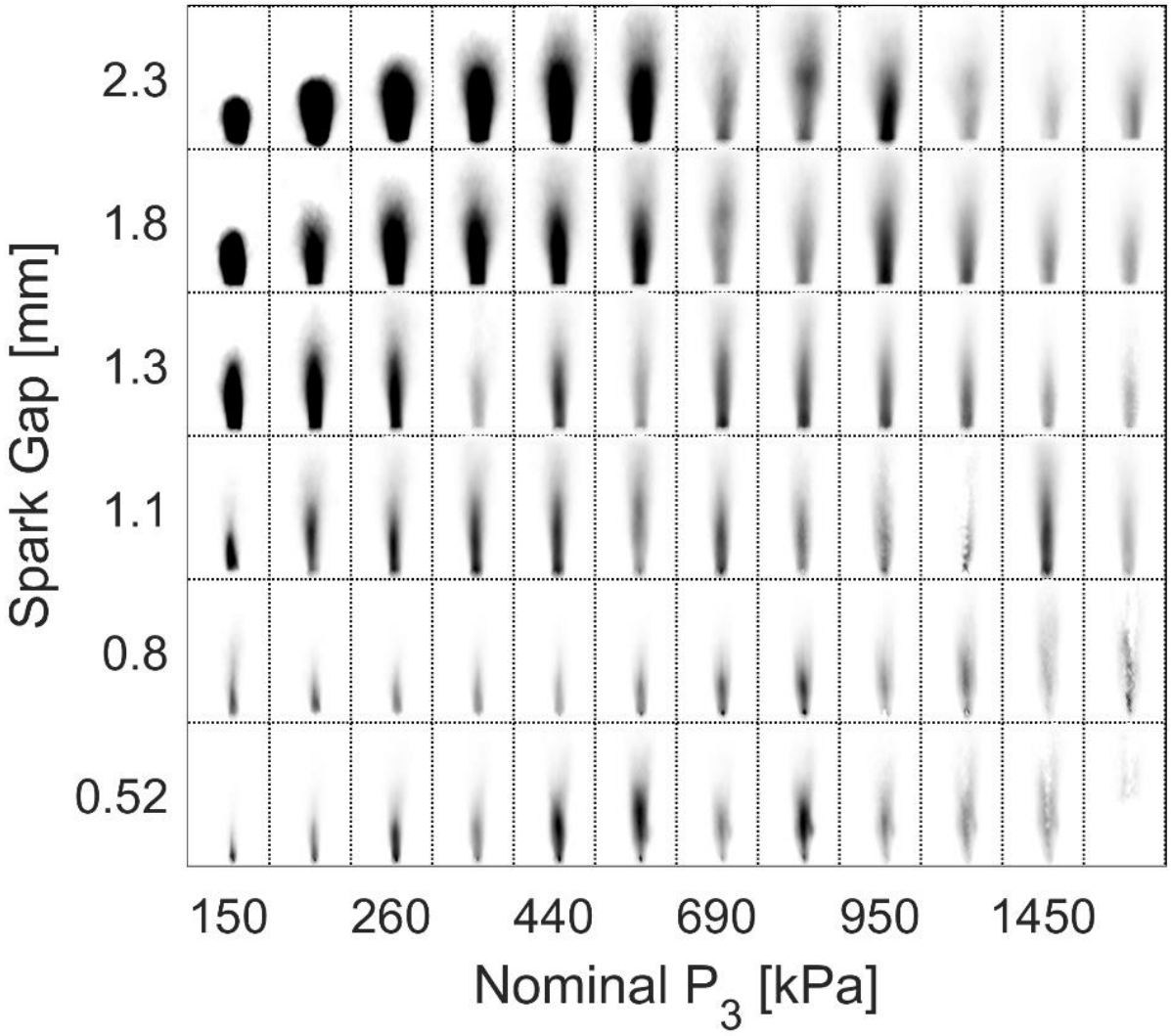


Figure 23 – Spatiotemporal signals per spark gap and pressure combination for the bipolar exciter

## CONCLUSIONS

Spark discharges are measured across an annular spark-gap for a unipolar and bipolar exciter. High variability is observed for measurements of electrical data due to the nontrivial effects of quenching. A mean measurement for attempts to discharge a spark accurately represents the mean behavior for each exciter, but does not accurately capture the properties of individual spark discharge events. To do so, the effects of quenching must be removed from dataset prior to analysis.

Spark quenching has profound impact on electrical measurements, creating false readings that artificially impact measurements. Due to differences in exciter circuitry, electrical ringing may be present

for all quenched cases, none at all, or those at the edge of the breakdown voltage. Electrical ringing causes false discharge readings for nonintrusive probes located on the leads between the spark exciter and spark igniter. False discharge readings during a quenched event may lead to elevated breakdown voltage and energy measurements, whereas quenched cases without ringing may deflate mean values. A careful examination of the current output should alleviate this issue. The percent of cases quenched typically increased with the pressure-distance product.

After filtering quenched trials, measurements for breakdown voltage and energy discharged were observed to generally increase with a rising pressure-distance product. In contrast, spark duration, channel resistance, and plume velocity were positively related to the pressure-distance quotient. The increase in channel resistance is hypothesized to be the result of the electrical arc stretching due to advection of the ionized particles during discharge. Spark discharges lasted 20 - 30 μs for the bipolar exciter and 50 - 90 μs for the unipolar exciter. Channel resistances for the unipolar exciter ranged from 1 - 10 Ω during the discharge with the sustaining voltages between 50 - 300 V. The bipolar exciter had varying channel resistances, which increased in value for each subsequent breakdown event. For positive current, the channel resistances were 1 - 2 Ω, 3 - 7 Ω, and >10 Ω for the first, third, and fifth phases of sustaining voltage respectively, which ranged similarly in value to the sustaining voltage of the unipolar exciter (between 50 - 300 V).

Schlieren imaging was used to determine the velocity of exhaust plumes from the spark discharge for the bipolar exciter. The values ranged between 20 - 300 m/s. The electrical arc was estimated to penetrate the flow anywhere from 0.5 - 5 mm with a positive correlation to the supply pressure and negative correlation to the gap size. The spatiotemporal development of the exhaust plume was represented by a time-average for each case. In general, decreasing the spark-gap width for a given pressure resulted in narrower and longer plumes. The peak length and width recorded varies per spark gap, but local maxima appear to be present as the pressure increases. The results for the spark plume do not include quenched events and are normalized to the number of spark discharges captured by schlieren. These results should be paired with the quenching map to determine the optimal conditions for downstream ignition.

# CHAPTER 3
# COMPUTATIONAL VERIFICATION OF OBJECTIVE FUNCTIONS FOR THE DESIGN AND DEVELOPMENT OF NONDIMENSIONAL MIXING CORRELATIONS

## INTRODUCTION

Liquid rocket engine (LRE) injectors have been studied by researchers for a substantial period of time. Burick, Calhoon, Falk, Gill, Kors, Ito, Nurick, and Walker [54, 55, 56, 57, 58] performed foundational experimental research on injectors at NASA in the 1970s. For like-doublet elements, Falk and Burick determined that mixing in injectors is driven primarily by geometric design variables (e.g., fan spacing and impingement angle) and secondarily by the propellant momentum ratio. Their work determined that the optimization of intraelement spacing and the fan inclination (polar) angle was interrelated. This, in turn, led them to focus their efforts on testing fan inclination and propellant momentum ratios [54]. Gill and Nurick outlined the effects of large impingement angles for unlike-impinging elements, which lead to heating of the injector face and poor mixing from backflow. They determined that short free stream jet lengths were preferable for preventing impingement of partially disintegrated streams [55].

Much of the foundational injector work consisted of cold flow, hot flow, and water flow testing with little to no computational efforts attempted due to the fluid dynamic complexity of the work and a lack of technological resources available at the time of publication. With the advancement of processing power, the field has naturally evolved. Simulations of individual elements of an injector assembly, doublets [59, 60] and coaxial elements [61], have verified the dispersion and atomization of propellant streams as functions of element geometry (e.g., doublet impingement angles) and velocity gradients between coaxial streams. More computationally intensive studies have examined injector manifolds with scores of injector elements utilized to optimize performance for specific applications [62]. These studies are further supported by related efforts to assess accuracy and validate simulations of individual coaxial elements [63, 64]. Numerical studies for swirl coaxial injectors have been used to guide design [65] and ascertain how the relative momentum of axial and swirl flows impacts mixing and flame development [66].

Gaps in the literature emerge as injector elements are combined to form more complex and unique injector configurations, without reaching the size and complexity of a full injector manifold. One such

configuration uses sets of opposed doublets and a central annular injector, which is similar but not identical to that of a pentad injector. When combined with a spark igniter, this injector forms an augmented spark impinging (ASI) igniter. Another version of the ASI, the compact augmented spark impinging (CASI) igniter [67], has the same injector geometry but a different external design, making it lighter in weight and allowing it to fit into a smaller envelope. The ASI and CASI igniters have a strong record of reliable ignition in both development and demonstration engines at the test stands at NASA Marshall Space Flight Center (MSFC) [67]. The CASI element configuration, unlike a true pentad injector, has the opposed-doublet elements impinge on unique points, coplanar with the central element, and is thus referred to as a "pseudo-pentad" igniter. To the author's knowledge, there are no existing simulations of a pseudo-pentad injector configuration at the base of a tube (i.e., a CASI igniter).

The igniter's central injector is an annular injector that is collinear with the torch tube axis. A spark igniter electrode serves as the center body of the annulus. When a sufficient voltage is applied across the gap of the annulus during igniter startup, an electrical arc is generated, exciting and thermally energizing the oxidizer flowing through the annular gap. The resultant oxidizer plasma impinges on a combustible fluid mixture created by the remaining four injectors, configured in opposed like-doublet elements (i.e., pairs of fuel and oxidizer doublets) on the chamber wall. A fuel-lean flame is created and propagates down the tube. The hot oxidizer products exit the torch tube to mix with and ignite a coaxial coolant fuel shroud, creating a fuel-rich region within the main combustion chamber.

When component tests are performed using this igniter, gaseous propellants are supplied to the CASI igniter at near-ambient conditions. Such conditions are likened to snapshots of the transient startup (viz., prior to two-phase or liquid flow) and are expected to represent real-world applications as long as the hardware is not cold-soaked and has sufficient thermal inertia to vaporize the initial incoming propellant. Under these assumptions, the experimental flame structures and ignition probability for the ASI should resemble the actual behavior in an LRE. Empirical results of component-level testing show that the core flame is stable once the combustion reaction initiates for the device [17]. [REDACTED]. Furthermore, stability is dependent on, and sensitive to, local mixture ratios and mass distributions. For unconstrained

like-doublet elements, known for high stability and good mixing, the flame is anchored at the impingement point of the fluid streams where more consistent mixture ratios are present [55]. In contrast to a like-doublet element, the opposed doublets of the CASI igniter impinge at mirrored locations on opposite sides of the central injector. Consequently, the doublet elements do not have an impingement point (in contrast to a quadlet element), but instead an impingement plane where the respective fluid fans (i.e., dispersion from the doublets) mix with the central injector flow.

[REDACTED], the core flame must be anchored by a fluid dynamic phenomenon. A parametric study has been conducted with three-dimensional, time-accurate computational fluid dynamics (CFD) simulations using Loci/CHEM [68, 69]. Nonreacting gaseous simulations were performed across a variety of mass flow rates, injector sizes, and local mixture ratios from the opposed doublets. To aid in the design and development of the torch igniters, conservation law objective functions were applied and verified through computational results. A nondimensional analysis was used to find correlations between figures of merit: core mixture ratio, injector mixture ratio, Reynolds number (*Re*), and mixing length.

Practical value lies in extrapolation. Engine-level requirements explicitly dictate design (e.g., What are the igniter propellants? What is their flammability limit? What is the acceptable heat load given the material? What is the minimum or maximum length of the torch tube? What is the reaction velocity? What is the total mass flow rate?). The answers provide constraints for core mixture ratio, mixing length, injector mixture ratio, and Reynolds number. Combined with the analytics and correlations to follow, the same answers lead to unique design solutions with respect to mass flow rate and geometric variables.

### OBJECTIVE FUNCTIONS FOR DESIGN AND DIMENSIONAL ANALYSIS

Designing a new reliable, reusable, and robust torch igniter is no trivial task. For novel designs, simulations aid in understanding fluid dynamics, mixing rates, and scalability, while experimental testing validates operating regimes. Both methods have drawbacks for resource consumption and lend to iterative designs based on the designer's intuition, past empirical results, and the singular solution from a complex

simulation. Iteration, regardless of the inspiration, can be costly with respect to both time and monetary constraints.

Returning to a simplified approach, a conservation law analysis is performed for a pseudo-pentad injector constrained by an outer tube. Assumptions for this analysis include isentropic/adiabatic conditions and elastic collisions of fluid streams. Geometric symmetry (as outlined in the methodology section) can also be assumed, simplifying relations further, but is excluded for completeness. For brevity in the following explanation, subscript c refers to the core flow, f to fuel streams, i to injectors, o to oxidizer streams, s to spark gap width, t to tube, and n to an unselected stream. Diameter is defined with d, mass flow rate with $\dot{m}$, mixture ratio with MR, velocity with V, fan inclination (polar angle) with α, doublet impingement angle with β, density with ρ, and axial momentum factor as η. Fluid properties for the injectors are estimated just upstream of the injector orifices. Note that an iterative solution may be necessary depending on system design, but is undoubtedly more affordable and faster than computational or experimental tests.

Conservation of mass is first used to define the mass flow rate of fuel in terms of the core mixture ratio, oxidizer mass flow from the injectors, and oxidizer mass flow from the spark annulus (Equation 3).

$$\dot{m}_{f,i} = \frac{\dot{m}_{o,i}+\dot{m}_{o,s}}{MR_c} = \frac{\dot{m}_{total}}{(1+MR_c)} = \frac{V_{bulk}*\rho_{bulk}*\pi*d_c^2}{4*(1+MR_c)} \quad (3)$$

Conservation of momentum is performed first radially (see Figure 24a) for each set of injectors, and then between the impingement of the resultant streams. The radial momentums are balanced with the intention of the bulk flow moving centrally down the tube and set equal (Equation 4).

$$\dot{m}_{f,i} V_{f,i} \cos(\beta_f) = \dot{m}_{o,i} V_{o,i} \cos(\beta_o) \quad (4)$$

A pseudo-physical variable, the injector mixture ratio (or analytic mixture ratio), results from algebraic manipulation (Equation 5).

$$MR_i = \frac{\dot{m}_{o,i}}{\dot{m}_{f,i}} = \left(\frac{d_{o,i}}{d_{f,i}}\right)\left(\frac{\cos(\beta_f)}{\cos(\beta_o)}\frac{\rho_{o,i}}{\rho_{f,i}}\right)^{0.5} \quad (5)$$

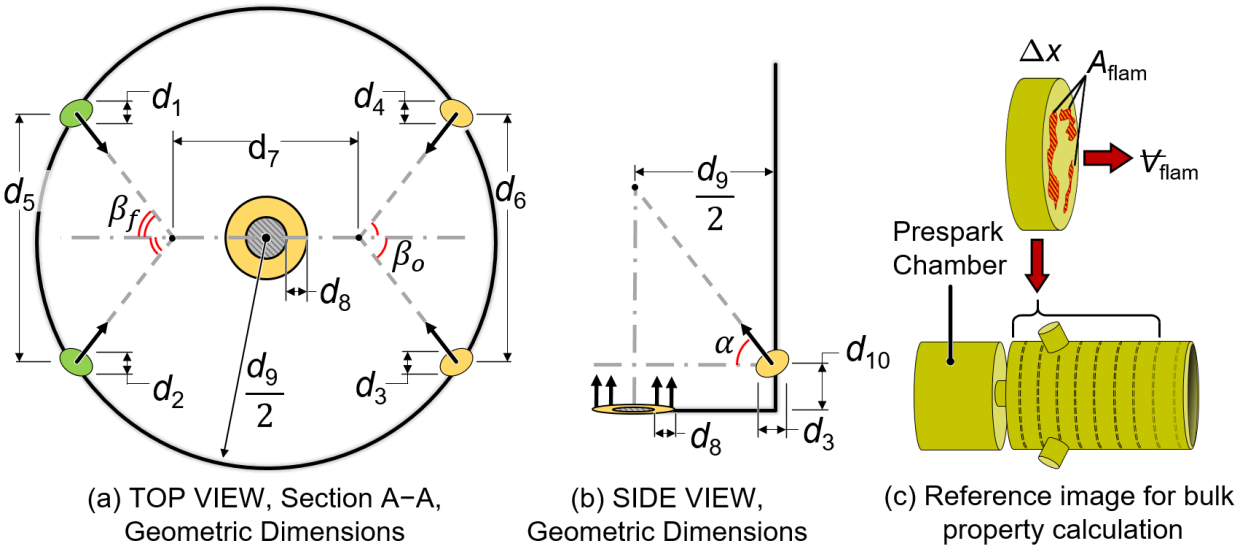


Figure 24 – (a, b) geometric variables for the pseudo pentad injectors; and (c) illustration of a bulk property calculation by spatial integration at discrete cross-sectional locations. See Table 1 for subscript references.

Conservation of momentum is next calculated axially (see Figure 1b) between a single injector stream (as streams already balanced in momentum and denoted with index n) and the flow exiting the spark annulus (Equation 6). Axial momentum is not constrained in Equation 6, and consequently a degree of freedom exists to account for the question of "annulus area" or "tube area," A. This introduces a variable referred to as the axial momentum factor (η), which is of no small consequence when solving for the relation between mass flow rates (Equation 7).

$$\dot{m}_{o,s} V_{o,s} = \eta \frac{\sin(\alpha)}{2} \dot{m}_{n,i} V_{n,i} \tag{6}$$

$$\dot{m}_{o,s} = \dot{m}_{n,i} \left( \frac{\rho_{o,s}}{\rho_{n,i}} * \frac{A_s}{A_{n,i}} * \frac{\eta \sin(\alpha)}{2} \right)^{0.5} \tag{7}$$

The question of whether to use the area of the tube or the area of the spark annulus is substantial. The difference in area results in a considerable difference between velocities at each location. Since the flow through the spark gap annulus expands prior to reaching the injector centerline, the authors selected the area of the torch tube to capture the momentum of the flow more accurately. As the pressure, P, immediately upstream of both the spark gap and each injector doublet cannot be guaranteed to be equal, the injector stream is left indexed and may be replaced with either of the injector streams (Equation 8).

$$\dot{m}_{o,s} = \dot{m}_{n,i}\left(\frac{d_t}{d_{n,i}}\right)\left(\frac{\rho_{o,s}}{\rho_{n,i}}\frac{\eta\sin(\alpha)}{2}\right)^{0.5} \tag{8}$$

Returning to conservation of mass, the core mixture ratio is then defined in terms of the injection mixture ratio and geometric properties (Equation 9).

$$MR_c = \frac{\dot{m}_{o,i}+\dot{m}_{o,s}}{\dot{m}_{f,i}} = MR_i\left(1+\frac{d_t}{d_{o,i}}\right)\left(\frac{\rho_{o,s}}{\rho_{n,i}}\frac{\eta\sin(\alpha)}{2}\right)^{0.5} \tag{9}$$

At this point, all variables are explicitly related and can be rearranged one last time. The final manipulation solves for each injector diameter (Equations 10 and 11).

$$d_{o,i} = \left(\frac{d_t}{\frac{MR_c}{MR_i}-1}\left(\frac{\rho_{o,s}}{\rho_{n,i}}\frac{\eta\sin(\alpha)}{2}\right)^{0.5}\right) \tag{10}$$

$$d_{f,i} = \frac{d_{o,i}*\left(\frac{\rho_{o,i}}{\rho_{f,i}}\frac{\cos(\beta_f)}{\cos(\beta_o)}\right)^{0.5}}{MR_i} \tag{11}$$

From a design perspective, a new igniter is subject to (1) global constraints of the system (viz., torch tube diameter and total mass flow rate), (2) material or fluid properties (viz., melting and combustion temperatures, fluid densities, and ignition probability), and (3) the polar angle of the injectors. Apart from the ignition probability, these constraints and properties are readily available, and the polar angle has been empirically optimized in past work [55, 57]. Through these relations and obeying external constraints, the task of designing a new igniter is tentatively simplified to the ignition probability for a given mixture ratio.

Healthy skepticism requires verification of these relations and their values. Initial solutions to these equations are subject to the uncertainty of the fluid densities, which inherently alters the mass flow rates and consequently the mixture ratios. An iterative solution of Equations 10 and 11 will clearly be more accurate than a single calculation based on order-of-magnitude estimates for the fluid densities (or more aptly, fluid pressures). In addition, the analytic relations here are unconstrained due to the axial momentum factor and require further information for use. Regardless of whether a spark gap length or tube diameter is known for the system, there is a lack of knowledge regarding what values the axial momentum factor should be, and therefore the injector diameters are not defined. Compensating for these uncertainties, simulation

results are used to determine mixing correlations, verify the pseudo-physical variable (i.e., injector mixture ratio), and provide an order-of-magnitude estimate for the axial momentum factor.

Twenty unique nonreacting simulations were calculated using variable geometries and mass flow rates. The test matrix was developed using Equations 3-11 with the following constraints. The bulk mass flow rate ($\dot{m}$) and injector mixture ratio ($MR_i$, Equation 5) were varied between simulations. Two spark gap lengths ($d_s$) were used based on related spark discharge efforts [47]. The tube diameter ($d_t$), core mixture ratio ($MR_c$, Equation 9), doublet impingement angle (β), and fan inclination (polar) angle of injectors (α) were held constant. All other test matrix variables were dictated by the relations above, with injector diameters bound by practical geometric constraints ($d_{o,i}$, Equation 10 and $d_{f,i}$, Equation 11). To reiterate concisely, the constants for creating the test matrix are $d_t$, $MR_c$, α, β, and ρ, and the variables are $MR_i$, $\dot{m}$, and $d_s$.

The majority of test matrix constants were selected or constrained based on prior literature or existing hardware. [REDACTED]. The doublet impingement angle (β) [REDACTED] falls within the optimal range listed by literature for fluid dispersion [54]. Density (ρ) was assumed at atmospheric conditions.

Fifteen unique geometries were then created and used across select flow rates. [REDACTED]. The lower and moderate range of mass flow rates emulated experimental data from spark annulus studies [47, 48]. Injector diameter selection was limited by torch tube dimensions, doublet geometry, and standard bit sizes used in manufacturing. [REDACTED]. The axial momentum factor (η) was not constrained in the development of the computational test matrix. Instead, it was calculated using a preselected spark gap distance. A full simulation matrix may be found in the following chapter.

The Buckingham Pi (π) theorem was applied to the pseudo-pentad injector configuration and the volume of gas constrained by the constant-area tube. The analysis was used to investigate correlations between fluid properties, mixture ratios, and geometric ratios. Table 2 displays all relevant variables used in this analysis, where d is distance or diameter, β is doublet impingement angle, α is the fan inclination (polar) angle, V is velocity, ρ is density, μ is dynamic viscosity, and V is the volume of flammable gas (i.e.,

output metric). Geometric variables are shown by top and side views of the injection elements in Figure 24a and b, respectively. Subscript numbering is consistent between impingement angles and their respective injectors. The value of fluid properties is estimated at the exit face of their respective injectors. By assuming symmetry of impingement and polar angles, and discarding linearly proportional variables, 14 π-groups become relevant from the plethora of combinations. Select groups are found through minor manipulation of the objective functions (groups 7, 11–14) or are functions of pertinent variables (group 3).

Results from the simulations are used to verify the suitability of the objective functions as a design tool and to develop correlations for mixing. The analytics, when combined with the correlations to follow, may be used to set nominal injector and core mixture ratios while conceivably maintaining a purely axial bulk flow (i.e., not canted toward a wall by unbalanced momentum fluxes).

Table 2 – Variables for individual fluid streams and relevant geometric properties (top) and the resulting nondimensional π-groups (bottom).

| $\forall$ | $V_1$ | $\rho_1$ | $\mu_1$ | $\beta_1$ | $\alpha_1$ | $d_1$ |
|---|---|---|---|---|---|---|
| $\{L^3\}$ | $\{Lt^{-1}\}$ | $\{ML^{-3}\}$ | $\{ML^{-1}t^{-1}\}$ | $\{-\}$ | $\{-\}$ | $\{L\}$ |
| | $V_2$ | $\rho_2$ | $\mu_2$ | $\beta_2$ | $\alpha_2$ | $d_2$ |
| | $\{Lt^{-1}\}$ | $\{ML^{-3}\}$ | $\{ML^{-1}t^{-1}\}$ | $\{-\}$ | $\{-\}$ | $\{L\}$ |
| | $V_3$ | $\rho_3$ | $\mu_3$ | $\beta_3$ | $\alpha_3$ | $d_3$ |
| | $\{Lt^{-1}\}$ | $\{ML^{-3}\}$ | $\{ML^{-1}t^{-1}\}$ | $\{-\}$ | $\{-\}$ | $\{L\}$ |
| | $V_4$ | $\rho_4$ | $\mu_4$ | $\beta_4$ | $\alpha_4$ | $d_4$ |
| | $\{Lt^{-1}\}$ | $\{ML^{-3}\}$ | $\{ML^{-1}t^{-1}\}$ | $\{-\}$ | $\{-\}$ | $\{L\}$ |
| | $d_5$ | $d_6$ | $d_7$ | $d_8$ | $d_9$ | $d_{10}$ |
| | $\{L\}$ | $\{L\}$ | $\{L\}$ | $\{L\}$ | $\{L\}$ | $\{L\}$ |

| Index | Parameter |
|---|---|
| 1 | Fuel stream 1 |
| 2 | Fuel stream 2 |
| 3 | Ox stream 1 |
| 4 | Ox stream 2 |
| 5 | Fuel doublet streams spacing |
| 6 | Ox doublet streams spacing |
| 7 | Lateral doublet set spacing |
| 8 | Spark gap width |
| 9 | Tube diameter |
| 10 | Doublet height offset |

$$\prod_1 = \frac{\forall}{d_1^3} \qquad \prod_2 = \frac{\rho_1}{\rho_3} \qquad \prod_3 = \frac{\rho_1 V_1 d_1}{\mu_1} \qquad \prod_4 = \beta_1 \qquad \prod_5 = \beta_3$$

$$\prod_6 = \alpha_1 \qquad \prod_7 = \frac{d_1}{d_3} \qquad \prod_8 = \frac{d_1}{d_5} \qquad \prod_9 = \frac{d_1}{d_6} \qquad \prod_{10} = \frac{d_1}{d_7}$$

$$\prod_{11} = \frac{d_1}{d_8} \qquad \prod_{12} = \frac{d_1}{d_9} \qquad \prod_{13} = MR_i \qquad \prod_{14} = MR_c$$

## METHODOLOGY

Simulations were performed using Loci/CHEM, a C++ density-based fluid solver [68, 69]. Time integration methods from the solver were a first-order backward Euler time integration with local time stepping for steady-state solutions, and a second-order, three-point backward time integration scheme for

time-accurate solutions. Menter's Shear Stress Transport (SST) model was used for turbulence, and the Nichols-Nelson hybrid Reynolds-averaged Navier-Stokes/Large-Eddy Simulation (RANS/LES) model for multiscale calculations. The fluid linear solver was symmetric Gauss-Seidel. Numerical approaches and equation formulation are outlined in full detail in the Loci/CHEM user manual.

The flow domain, shown in Figure 30d, was a pseudo-pentad injector constrained by a constant-area tube. The igniter had two like-doublet elements on the wall of the tube and a central flow of oxygen from a spark gap annulus shown in Figure 24a. Injectors were offset axially from the spark gap annulus shown in Figure 24b. Flow exited to stagnant conditions through a converging nozzle and dissipated before reaching the far-field boundary conditions. All flows were nonreacting/cold flow. Wall boundaries were no-slip and adiabatic. Inlets were prescribed a constant mass flow rate and species concentration of either pure oxygen or pure methane. Fluid properties and species were spatially integrated over cross sections to determine bulk values, as illustrated in Figure 24c.

The surface mesh consisted of an unstructured triangular mesh with a minimum cell density of one per thousandth of an in. along the circumference. The surface mesh was imported to an advancing-front/local-reconnection (AFLR) tool to generate an unstructured tetrahedral volume mesh [70]. AFLR generated the volume mesh from the surface mesh (initially an unstructured triangular mesh). The boundary layer mesh, which overrode the initial volume mesh, was made of prisms extruded from the wall, initially 35 layers thick with spacing of 2e-5 in.

A mesh independence study was performed by reducing the surface cell density by 25% and 50%. Quantitatively, the root-mean square error (RMSE) between all three meshes was low, with a peak value of 8% RMSE for mass fraction indicating low absolute differences and good correlation in species concentrations to the original mesh. Qualitatively, the velocity gradient exiting the spark gap was smeared with the minimum 25% reduction of cell density. This resulted in a higher pressure at the head end of the tube and decreased backflow. At the region of interest, the finest mesh resolution was implemented.

## RESULTS

Correlations of nondimensionalized π-groups (viz., geometric ratios, Reynolds number, and analytic mixture ratios) with (1) mixing lengths and (2) local mixture ratios of nonreacting gaseous flow are presented here for a pseudo- pentad injector constrained by a constant-area tube.

Twenty simulations were performed across 15 unique geometries at a variety of flow rates. The core mixture ratio was [REDACTED] near the lean flammability limit for methane-oxygen mixtures. Reynolds numbers varied from 10,000 to 160,000 for bulk flow. Bulk flow rates were subsonic, and compressibility effects were observed for the upper half of mass flow rates, as shown in Figure 25a by the asymptotic approach to 0.3 Mach and nonlinear increase in bulk core density. The analytic injector mixture ratio ($MR_i$) was varied [REDACTED] as constrained by Equation 5. Explicitly, the injector diameter ratio and subsequent mass flow rates were altered to satisfy the radial momentum balance (Equation 4). The local mixture ratio present in the torch tube was evaluated by the two methods shown in Figure 25b—an effective 2D integral across the injector centerline plane and the volume of flow within one-half-tube diameter of the spark annulus.

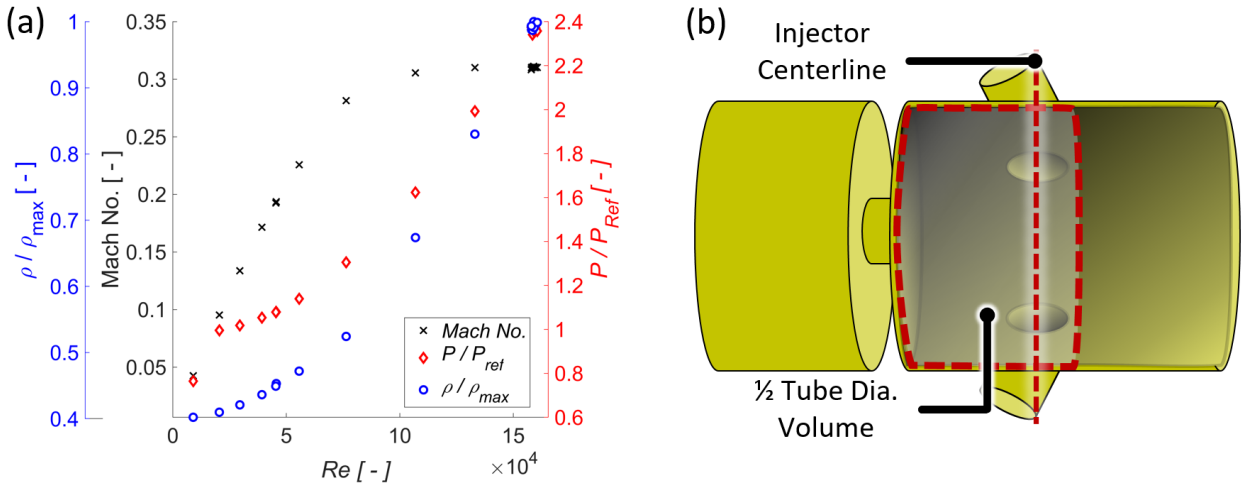


Figure 25 – (a) Flow properties versus Reynolds number for cold flow simulations; and (b) measurement locations for calculating local mixture ratios at (1) the injector centerline and (2) as a bulk property within one-half-tube diameter of the spark gap.

## Regression Analysis and Mixing Length Correlations

Mixing lengths are observed to be linearly related to the product of exponentiated geometric variables and the Reynolds number, with the Reynolds number being the primary factor. Bulk values of mixture ratio are discretized by spatial integration of the full $2\pi$ cross-sectional area (reference Figure 24c and Figure 25b). The domain is divided into quadrants along the x- and y-planes for analysis (Figure 26a). Quadrants are numbered one (1) to four (4), starting in the top right quadrant and moving counterclockwise with the oxygen injection site captured in quadrant one (1) and the fuel injection site captured in quadrant three (3). Mixing length is then quantified by the mixture ratio convergence of the mass fraction of methane (yCH4) between all quadrants and the local value of the full domain.

Bulk mixture ratios are calculated for each quadrant and for the full cross section illustrated in Figure 26a. The difference between local mixtures and the bulk mixture are calculated for each quadrant (shown in Figure 26b) to determine the respective L2-norms (Euclidean distances). They are averaged to create a mean L1-norm (i.e., deviation from perfectly mixed). A backward-moving average is taken to reduce noise. Mixing length is then measured by the percent difference of the mean L2-norm and the local bulk mixture ratio, the unmixed percentage, as shown in Figure 26c. This begs the question, “What quality of mixing is practically useful?” To address the needs of unknown application, predictors were tested across a wide range of mixing thresholds.

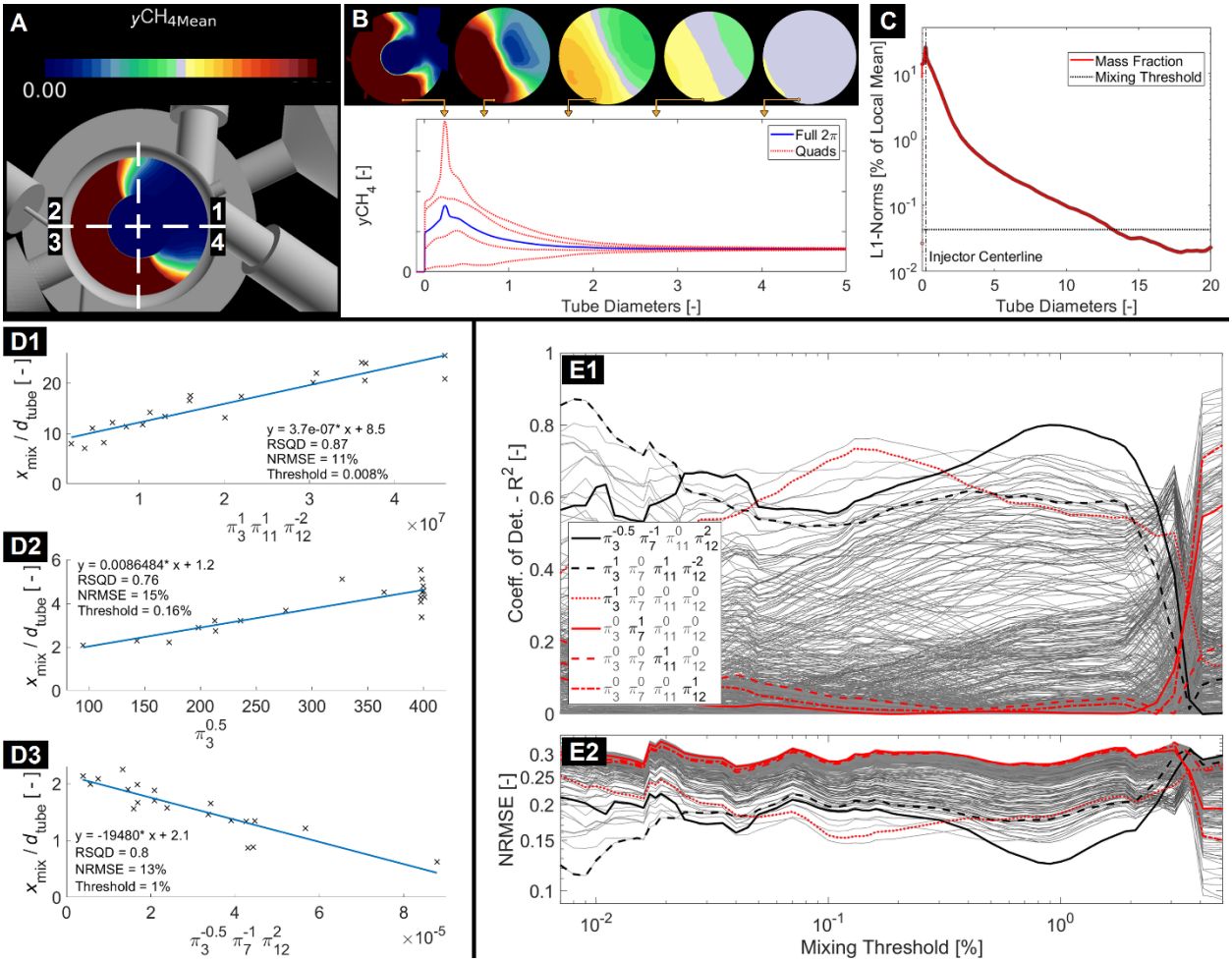


Figure 26 – (a) Torch tube cross section and quadrant division; (b) illustration of mixing at select axial locations and corresponding mixing plot; (c) mixing variation (L1-norm) with a mixing threshold (horizontal bar) shown at 0.04% variation; (d) mixing length predictions at local maxima of $R^2$ for select mixing thresholds; and (e) visualization of the regression analysis for mixing thresholds where $R^2$ and NRMSE are shown for predictor combinations (grey lines) across thresholds from 0.005% to 5% of unmixed species.

Table 3 – Nondimensional groups for determining mixing length across select mixing thresholds.

| **Index** | $\pi_3$ | $\pi_7$ | $\pi_{11}$ | $\pi_{12}$ | **Mixing Threshold** | **$R^2$** | **NRMSE** |
|---|---|---|---|---|---|---|---|
| | $[Re]$ | $[d_f/d_o]$ | $[d_f/d_s]$ | $[d_f/d_t]$ | [% unmixed] | [ - ] | [ - ] |
| 1 | 1 | 0 | 1 | -2 | 0.008 % | 0.87 | 11 % |
| 2 | 0.5 | 0 | 0 | 0 | 0.160 % | 0.76 | 15 % |
| 3 | -0.5 | -1 | 0 | 2 | 1.000 % | 0.80 | 13 % |

The threshold for what mixture constitutes “well-mixed” must be addressed here. The threshold for mixing is a practical choice, and a regression analysis is presented. Local peaks for the coefficient of determination ($R^2$) are listed in Table 3 and shown in Figure 26d for respective nondimensional groups. $R^2$

is plotted against unmixed thresholds ranging from 0.01% to 4% for products of exponentiated nondimensional groups in Figure 26e. For reference, coefficients for the slope-intercept form and the normalized root mean square error (NRMSE) are provided for each case. There is a sudden inversion of predictor accuracy beyond 2%, which approaches the mass percent of methane within the core flow. Inaccurate and nonsensical mixing lengths are predicted at higher threshold values. Values of error and fitting shown in Figure 26e are for illustrative purposes only.

For all predictor combinations shown in Figure 26d, the mixing lengths extend with the rising Reynolds number ($\pi_3$), with the direct correlation shown in Figure 26d2. The nonaxial advective forces are dispersed further down the tube with higher bulk flow rates. The like-doublet elements are the primary cause of radial and azimuthal advection. The central spark annulus flow adds to the effect by generating a low-pressure zone at the spark gap faceplate, which creates recirculation of the flows exiting the like-doublet elements. The extension of both the recirculation zone and nonaxial forces is captured largely by the Reynolds number.

For a low mixing threshold, 1% unmixed, the relative size of the doublet element orifices to the core diameter is a greater factor ($\pi_{12}$). Larger orifice sizes correlate to shorter mixing lengths, and larger tube sizes correlate to longer mixing lengths as shown in Figure 26d1 and 26d3. The jets exiting the wider doublet orifices have greater dispersion before impinging and have a lower axial momentum component forward. Recalling the low-pressure zone created (thus a bulk recirculation zone) by high-velocity flow from the spark annulus, the low-momentum doublet flows are more susceptible to being swept backward.

For a high mixing threshold, near one-hundredth of 1% unmixed, the most important rations are $\pi_{11}$ and $\pi_{12}$, which are, respectively, the fuel orifice diameter to the spark annulus width and the fuel orifice diameter to the core diameter. Once more, the recirculation zone caused by the spark annulus is a driving factor. In this case, the spark annulus width is the only variable undiscussed. As observed in Figure 26d1, increasing the width of the spark annulus (the denominator of $\pi$-group 11) decreases the mixing length and is unlike prior explanations. A larger spark annulus decreases the pressure differential causing recirculation, but is

hypothesized to be less disruptive to the dispersion of fluids from the doublet injectors. Due to this, off-axis turbulent diffusion is thought to be less influential for fine mixing than off-axis advection.

LOCAL MIXTURE RATIO CORRELATIONS

From the standpoint of ignition probability, local mixture ratios are of paramount importance. A delicate balance exists between maintaining permissible combustion temperatures and the high probability of ignition. The ability to determine local mixture ratios is presently limited to unsubstantiated analytics, meticulous experimental diagnostics, or computationally intensive simulations. Coupling of the simulations and analytics in this work shows promise to perform quick hand calculations, simplifying and accelerating the engineering design process.

Multiplicative combinations of select π-groups are used as the independent variables. Equations 12 and 13 represent the relations used where $MR_{local,mean}$ is the mixture ratio for the volume of fluid within one-half-tube diameter of the spark annulus, and $MR_i$ is the mixture ratio at the injector centerline (see Figure 25b).

$$MR_{local,mean} = f(\prod_3, \prod_7, \prod_{11}, \prod_{12}, \prod_{13}) = f\left(Re^a \left(\frac{d_f}{d_o}\right)^b \left(\frac{d_f}{d_{sp}}\right)^c \left(\frac{d_f}{d_t}\right)^d MR_i^e\right) \quad (12)$$

$$MR_{i,simulated} = f\left(Re^a \left(\frac{d_f}{d_o}\right)^b \left(\frac{d_f}{d_{sp}}\right)^c \left(\frac{d_f}{d_t}\right)^d MR_i^e\right) \quad (13)$$

The simplest result is to compare the actual mixture ratio ($MR_{local}$) and the analytic injector mixture ratio ($MR_i$). Good agreement between these mixture ratios (i.e., predicted versus simulated) is shown in Figure 27, where the NRMSE is 8% to 9% of the total range. The analytic prediction of the mixture ratio is not expected to correspond one-to-one with the bulk mixture ratios as it does not account for either the oxidizer from the spark annulus, the recirculation zones imparting bias, or the variation of injector densities. In its least refined form, it provides a qualitative basis to state that the actual mixture ratio trends with the analytic mixture ratio. The agreement is expected for the injector centerline but not necessarily for the entire volume of gas within one-half-tube diameter of the spark gap. The ability to predict a local volume of gas alone implies the value of the analytics as a predictive tool, but more analysis is required for verification.

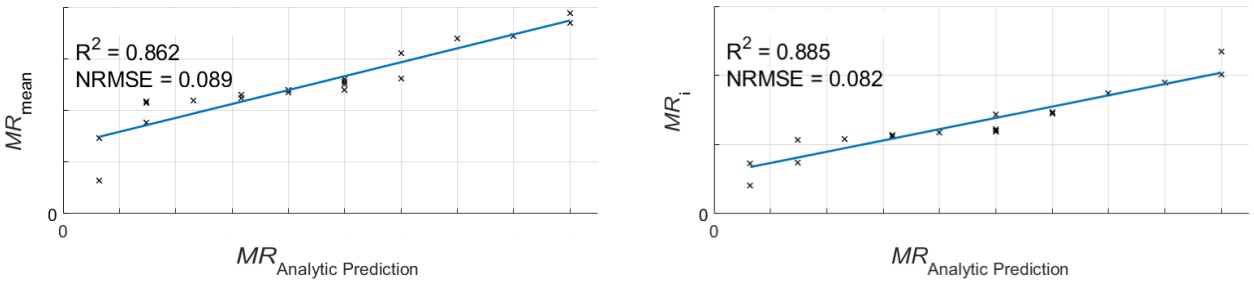


Figure 27 – Calculated mixture ratio versus analytic prediction of mixture ratio ($MR_i$) by Eq. 3 with the local mean mixture ratio shown on the left and simulated injector centerline mixture ratio on the right.

Exponent values (a, b, c, d, and e) for Equations 12 and 13 are varied from negative to positive four by one-half increments (-4:0.5:4). Due to the large number of iterations ($17^5$) and preliminary testing with coarse resolution, either the "a" or "e" exponent is tested over the full range while the other is set to zero. The number of total iterations is then reduced tenfold to a manageable quantity ($2*17^4$) for a 2.4-GHz 4-core processer to calculate.

It is assumed that a linear relationship exists for Equations 12 and 13. However, the mixture ratio by definition is asymptotic to the horizontal and vertical axes when plotted against fuel mass fractions or mixture fractions. Inversion of the mixture ratio, just as one inverts one of the simplest nonlinear expressions $x^{-1}$, results in a linear relation with the dependent variable. Practically, the inversion of the mixture ratio, when multiplied by a stoichiometric mass ratio, becomes the equivalence ratio ($\phi$) as shown in Equation 14. While also a nonlinear function, the equivalence ratio is closely emulated by a linear approximation between the flammability limits for methane.

$$\phi_{i,simulated} = \frac{4}{MR_{i,simulated}} = \frac{4}{f(\Pi_3,\Pi_7,\Pi_{11},\Pi_{12},\Pi_{13})} \tag{14}$$

With this assumption and inversion, strong linear correlations exist for a variety of combinations and equivalence ratios, indicated by high coefficients of determination ($R^2$). A high $R^2$ value indicates linearity but not necessarily that the correct independent variables (i.e., those that are causal over corollary) have been chosen. Recall that two sets of combinations were performed, one with geometric variables and the analytic mixture ratio and the other with geometric variables and the Reynolds number, for two methods of

determining the mixture ratio, a local volumetric mean and a planar slice at the injector centerline. Combinations of the π-groups and measurement zone produce four unique results to verify the relationship.

The bulk mixture ratio of the full cross section can easily and accurately be predicted by a select combination. The same combination (1) may not accurately depict local mixture ratios or (2) may not uniformly predict local mixture ratios. The former of the two cautions is expected as the fuel and oxidizer injectors are mirrored in location. Inconsistent local predictions, however, are a cause for concern. To combat the potential risk, a single combination was tested for each measurement zone across the full cross section and then for each of the four quadrants used to determine mixing (see Figure 26a). The resultant $R^2$ values across all five sectors were averaged and then used as the metric for prediction quality.

Linear fits for the $MR_i$ within each measurement zone are shown in Figure 28 for a select case. Here, one can see how local mixture ratios may be over- or underpredicted. It is also worth noting that mixture predictions within smaller areas (quadrants versus full cross section) are less accurate than that of the bulk mixture.

The top 10 results are listed in Table 4 across all π-group combinations. The columns denote the exponent variables, R2 values, NRMSEs, and coefficients for the slope-intercept form used to calculate the equivalence ratio. A common combination set (a=0, b=-2, c=0.5, d=4, and e=0) is found in the top 10 results for three of the four datasets (Table 4, Indexes 3b, 4c, and 1d). The same combination (Table 4, Index 30a) is the 30th most accurate for the outlying dataset and replaces the 10th-place row for completeness.

Nondimensional group 30a of Table 4 is a strong candidate for a quick calculation of mixture ratios (both local and centerline) due to a NRMSE below 4% and an $R^2$ greater than 0.98 for both locations. While these figures are promising, several other Buckingham Pi groups have similar statistics that denote strong linearity and low error. The value of multiple predictors is the ability to show model robustness. The π-groups resulting with a mean $R^2$ value greater than 0.975 are normalized (along the independent variable) and then plotted against both equivalence and mixture ratios, as shown in Figure 29. Standard deviation (σ) is shown for the slope (equivalence ratio only) and the y-intercept. For the equivalence ratio, the resulting coefficients of variation are 10–15% for the y-intercept, and 4–5% or less for the slope. For the mixture

ratio, the coefficient of variation is 12–19% for the y-intercept. One must not be misled into believing that either the mixture ratio or the equivalence ratio is more accurate than the other, and note that the variance differences are due to relative scales being used (MR, $\phi$) as compared to an absolute scale of mass fraction.

For Figure 29, cases A and B correspond to the first predictor variable set ($\pi_7$, $\pi_{11}$, $\pi_{12}$, $\pi_{13}$) for the $MR_{local,mean}$ and $MR_{i,simulated}$, respectively. Cases C and D correspond to the first predictor variable set ($\pi_3$, $\pi_7$, $\pi_{11}$, $\pi_{12}$) for the $MR_{local,mean}$ and $MR_{i,simulated}$, respectively. The mean predictors for A and C (viz., the slope and intercept of the linear equations) are nearly equal. The same is observed for the mean predictors for B and D. The distribution for each set is significantly different (as calculated with a 95% confidence interval), yet the absolute difference between either variable set (A vs. B or C vs. D) is likely inconsequential in comparison to the practical range targeted.

The importance of Figure 29 lies not in statistical (dis)similarity, but in the precision of the equivalence ratio predictions. The highest precision is observed as all cases approach stoichiometric conditions and near the upper flammability limit. The lowest precision is near the lower flammability limit. The variance is visually amplified by inverting the equivalence ratio, where mixture ratio models moving toward the lower flammability limit can vary by a factor of four. Even with the reduced precision near the lower flammability limit, only one model (within case A2) is observed outside of the flammable zone. The consistent predictions from these models are valuable, as they show that the local mixture ratio (be it averaged or a single cross section) is heavily dependent on geometric ratios of the injectors and torch tube ($\pi_7$, $\pi_{11}$, $\pi_{12}$).

Table 4 – Select nondimensional π-group combinations sorted by $R^2_{mean}$, mean normalized error for predicting associated mixture ratio across all slices, and slope-intercept-form constants solving for mixture ratio across a full 2π cross section.

**$MR_{i,\ simulated}$ Injector Centerline**

| Index | $\pi_{3\ or\ \pi_{13}}$ $[MR_i]$ | $\pi_7$ $[d_f/d_o]$ | $\pi_{11}$ $[d_f/d_s]$ | $\pi_{12}$ $[d_f/d_t]$ | $R^2_{mean}$ [ - ] | $NRMSE_{mean}$ [ % ] | $R^2_{2\pi}$ [ - ] | $NRMSE_{2\pi}$ [ % ] |
|---|---|---|---|---|---|---|---|---|
| 1a | 4 | 3 | -2 | 1.5 | 0.94 | 6.57 % | 0.97 | 4.20 % |
| 2a | 3 | 2 | -2 | 1.5 | 0.94 | 6.58 % | 0.97 | 4.23 % |
| 3a | 2 | 1 | -2 | 1.5 | 0.94 | 6.60 % | 0.97 | 4.25 % |
| 4a | -3 | -4 | -2 | 2 | 0.94 | 6.30 % | 0.97 | 4.28 % |
| 5a | 1 | 0 | -2 | 1.5 | 0.94 | 6.61 % | 0.97 | 4.29 % |
| 6a | -2 | -3 | -2 | 2 | 0.94 | 6.29 % | 0.97 | 4.27 % |
| 7a | -1 | -2 | -2 | 2 | 0.94 | 6.29 % | 0.97 | 4.26 % |
| 8a | 0 | -1 | -2 | 2 | 0.94 | 6.28 % | 0.97 | 4.26 % |
| 9a | 1 | 0 | -2 | 2 | 0.94 | 6.28 % | 0.97 | 4.25 % |
| 30a | 0 | -2 | 0.5 | 4 | 0.94 | 6.85% | 0.98 | 3.51% |

**$MR_{local,\ mean}$ 1/2 Tube Dia. from Spark Face**

| Index | $[MR_i]$ | $[d_f/d_o]$ | $[d_f/d_s]$ | $[d_f/d_t]$ | [ - ] | [ % ] | [ - ] | [ % ] |
|---|---|---|---|---|---|---|---|---|
| 1b | -2 | -4 | 0.5 | 4 | 0.94 | 5.96 % | 0.99 | 2.86 % |
| 2b | -1 | -3 | 0.5 | 4 | 0.94 | 5.97 % | 0.99 | 2.89 % |
| 3b | 0 | -2 | 0.5 | 4 | 0.94 | 5.98 % | 0.99 | 2.91 % |
| 4b | 1 | -1 | 0.5 | 4 | 0.94 | 5.99 % | 0.99 | 2.94 % |
| 5b | 2 | 0 | 0.5 | 4 | 0.94 | 5.99 % | 0.99 | 2.97 % |
| 6b | 3 | 1 | 0.5 | 4 | 0.94 | 6.00 % | 0.99 | 2.99 % |
| 7b | 4 | 2 | 0.5 | 4 | 0.93 | 6.01 % | 0.99 | 3.02 % |
| 8b | 4 | 3 | 0.5 | 2.5 | 0.93 | 6.36 % | 0.99 | 2.74 % |
| 9b | 3 | 2 | 0.5 | 2.5 | 0.93 | 6.37 % | 0.99 | 2.76 % |
| 10b | 2 | 1 | 0.5 | 2.5 | 0.93 | 6.39 % | 0.99 | 2.78 % |

**$MR_{i,\ simulated}$ Injector Centerline**

| Index | $[Re]$ | $[d_f/d_o]$ | $[d_f/d_s]$ | $[d_f/d_t]$ | [ - ] | [ % ] | [ - ] | [ % ] |
|---|---|---|---|---|---|---|---|---|
| 1c | 0 | -1 | -2 | 1.5 | 0.94 | 6.63 % | 0.97 | 4.32 % |
| 2c | 0 | -1 | -2 | 2 | 0.94 | 6.28 % | 0.97 | 4.26 % |
| 3c | 0 | -1.5 | -2.5 | 2.5 | 0.94 | 6.56 % | 0.98 | 3.42 % |
| 4c | 0 | -2 | 0.5 | 4 | 0.94 | 6.85 % | 0.98 | 3.51 % |
| 5c | 0 | -1 | -2.5 | 2 | 0.94 | 6.48 % | 0.99 | 2.89 % |
| 6c | 0 | -1.5 | -2.5 | 3 | 0.94 | 6.35 % | 0.98 | 3.77 % |
| 7c | 0 | -0.5 | -2 | 1 | 0.94 | 6.61 % | 0.98 | 3.56 % |
| 8c | 0 | -1 | -0.5 | 3 | 0.94 | 6.51 % | 0.98 | 3.52 % |
| 9c | 1 | -1.5 | 0.5 | 3.5 | 0.94 | 6.77 % | 0.98 | 3.29 % |
| 10c | 0 | -1 | -2.5 | 2.5 | 0.94 | 6.22 % | 0.98 | 3.78 % |

**$MR_{local,\ mean}$ 1/2 Tube Dia. from Spark Face**

| Index | $[Re]$ | $[d_f/d_o]$ | $[d_f/d_s]$ | $[d_f/d_t]$ | [ - ] | [ % ] | [ - ] | [ % ] |
|---|---|---|---|---|---|---|---|---|
| 1d | 0 | -2 | 0.5 | 4 | 0.94 | 5.98 % | 0.99 | 2.91 % |
| 2d | 0 | -1 | 0.5 | 2.5 | 0.93 | 6.42 % | 0.99 | 2.81 % |
| 3d | 0 | -1 | -2.5 | 1.5 | 0.93 | 5.99 % | 0.99 | 2.39 % |
| 4d | -2 | 2.5 | -4 | 1.5 | 0.93 | 6.42 % | 0.98 | 3.39 % |
| 5d | 1 | -1 | 0.5 | 2.5 | 0.93 | 6.31 % | 0.98 | 3.92 % |
| 6d | 0 | -0.5 | -2 | 0.5 | 0.93 | 6.19 % | 0.99 | 2.61 % |
| 7d | 0 | 0.5 | -0.5 | 1 | 0.93 | 6.15 % | 0.99 | 2.10 % |
| 8d | 0 | -1.5 | -2.5 | 2 | 0.93 | 6.44 % | 0.98 | 3.91 % |
| 9d | 0 | -0.5 | -2 | 0 | 0.93 | 6.71 % | 0.98 | 3.65 % |
| 10d | 0 | -1 | -2.5 | 1 | 0.93 | 6.58 % | 0.98 | 3.27 % |

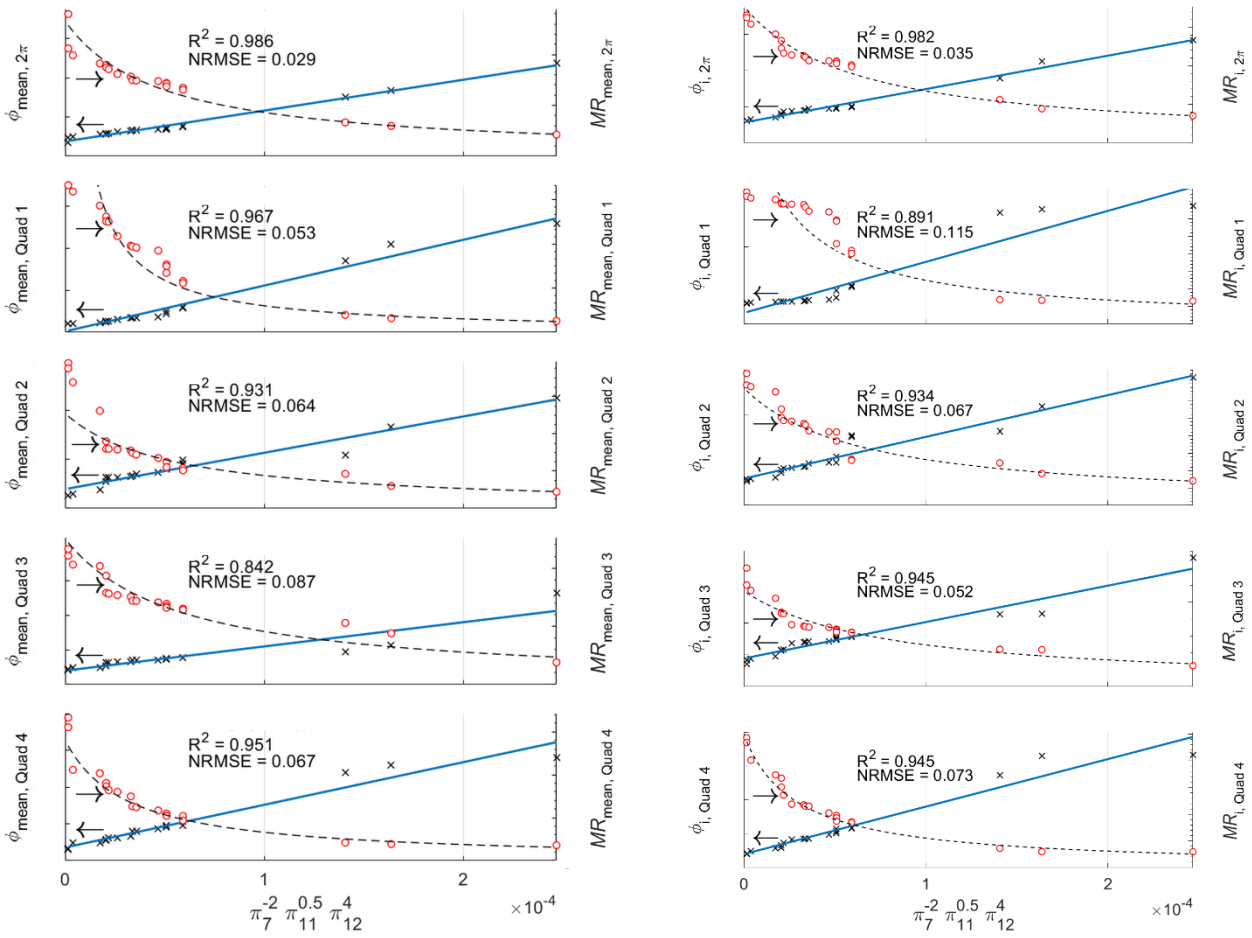


Figure 28 – Mean mixture ratio and equivalence ratio predictions averaged over one-half-tube diameter (left) and at the simulated injection centerline (right) for the full 2π cross section (top) and each quadrant (descending).

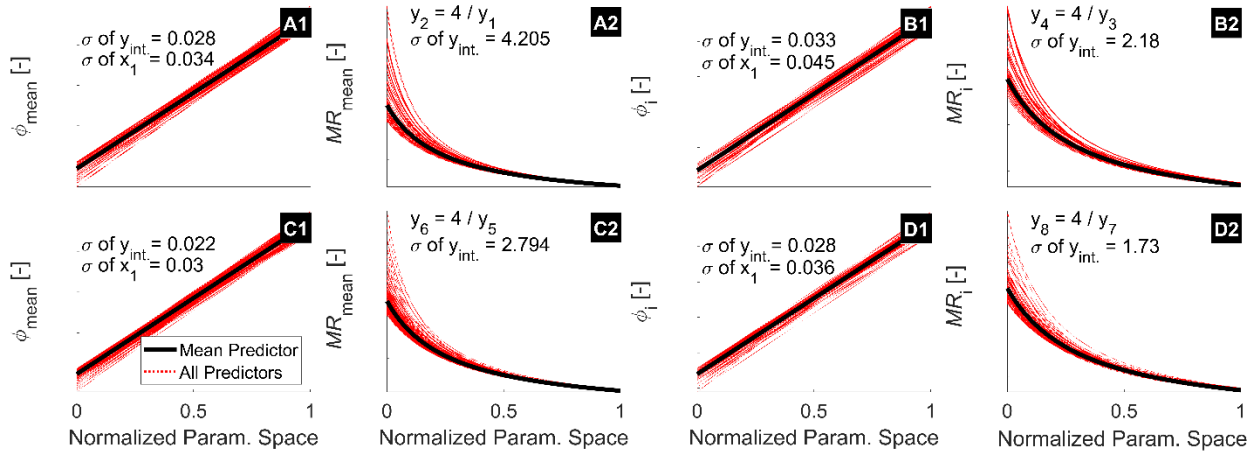


Figure 29 – Plots showing variation in predictor output and the mean output over a normalized axis for the independent variables. Cases A and B correspond to the first predictor variable set ($\prod_7, \prod_{11}, \prod_{12}, \prod_{13}$) for the MRlocal, mean and MRi, simulated, respectively. Cases C and D correspond to the first predictor variable set ($\prod_3, \prod_7, \prod_{11}, \prod_{12}$) for the MRlocal, mean and MRi, simulated, respectively. Similarity between (1) cases B and D and (2) cases A and C indicate that π-groups 3 and 13 are not important variables for mixture ratio predictions.

## CONCLUSIONS

A parametric study was performed for augmented spark igniter geometries over 20 nonreacting, gaseous flows within a constant-area tube using variable mass flow, geometric values, and local mixture ratios. Buckingham Pi analysis was used to determine correlations between mixing lengths and local mixtures as a function of select nondimensional groups. Strong linear relations were established between products of exponentiated $\pi$ variables and dependent variables. These relations provide the starting point for characterizing flow within an augmented spark impinging pseudo-pentad igniter.

Objective functions for design are derived from conservation of mass and momentum. The resulting equations are a function of system variables (viz., diameter and total mass flow), material and fluid properties (viz., mixture ignition probability and anticipated combustion temperatures), and impingement angles. The outputs of these relations are geometric variables and pertinent mixture ratios, which offer insight regarding mixing lengths and local mixture ratios via Buckingham Pi correlations. The combination of the analytics derived and models produced here is anticipated to minimize the need for computational resources during igniter development and reduce iterative experimental design methods.

The practical application of the design analytics is the greatest hypothesized value of this work. Designers of augmented spark impinging pseudo-pentad igniters have a preliminary verification of objective functions for a design correlating to the pertinent mixing properties. Optimizing features, such as the torch tube length necessary for mixing, will drastically reduce guesswork. Robust correlations provide a means to determine where the flow is fully mixed, which is essential for complete combustion. Correlations for the local mixture ratio at the base of the igniter have equal, if not greater, value as energy added by the spark igniter likely occurs within this region. As the flammability limits for methane-oxygen flames are substantially smaller than that of hydrogen-oxygen flames, one of the highest priorities should be the accurate and precise control of the mixture ratio where the activation energy is imparted.

Experimental validation is required for expansion of this work. It is anticipated that the relations shown apply to multiple fluids (viz., hydrogen-oxygen versus methane-oxygen), but it is advised that computational verification should occur before the assumption is substantiated.

# CHAPTER 4:
# INTERNAL FLOW OF AN AUGMENTED SPARK IMPINGING PSEUDO-PENTAD IGNITER

## INTRODUCTION

Spark-initiated torch igniters, often the preferred choice for igniting liquid rocket engines (LREs), have proven their reliability and reusability in many of NASA's human-rated vehicles. The Saturn V rocket that took Americans to the Moon, the Space Shuttles (i.e., the Space Transport System or STS) that ferried crews to the International Space Station, and the Space Launch System that will allow Americans once again to return to the Moon, all feature spark-initiated torch igniters in their liquid hydrogen/liquid oxygen engines. The igniters employed in these launch systems perform admirably as ignition sources for preburners and main combustion chambers in large core-stage and upper-stage engines. The success of these designs may give the impression that ignition phenomena in LREs is well understood by the propulsion community, but that is far from the case. Due to a lack of scientific understanding of rocket ignition phenomena, all the torch igniters utilized in these large-scale liquid hydrogen/liquid oxygen engines required years of trial-and-error testing and design iteration to perfect.

The propulsion community requires a better understanding of ignition devices to advance beyond the current iterative, incremental improvement stage. The torch igniter used at Marshall Space Flight Center for engine development testing is the compact augmented spark impinging (CASI) igniter, which has a strong record of accomplishment for reliable ignition of both hydrogen-oxygen and methane-oxygen propellants [67]. However, the design is still not well understood in terms of its flow phenomena and its sensitivity to changes in geometry and inlet flow conditions. The present study seeks to address these areas of critical interest through a three-dimensional, time-accurate computational fluid dynamics (CFD) analysis.

## AUGMENTED SPARK IGNITER DESIGN

The central oxygen injector of the igniter, collinear with the torch tube, uses a spark igniter to energize the gas flowing through it. Oxidizer flows past the electrode of the spark igniter in an annulus and impinges on the combustible mixture of fuel and oxidizer created by the remaining four injectors, which are in an

opposed like-doublet configuration on the chamber wall (see Figure 30). The internal injector configuration of the igniter is accordingly referred to as a pseudo-pentad configuration because it does not impinge on a single point as a true pentad would.

The sketches of Figure 30 are undoubtedly simple depictions of real-world phenomena and do not elucidate the complex and transient nature of fluid dynamics. Figures 30a–c depict the interaction of two impinging jets—a like-doublet injector [54, 55]. The front view shows the widest dispersion of the fluid to form a fan structure. A rotated perspective view and edge view follow. The fan has the widest dispersion along the injector centerline plane and smallest dispersion normal to the injector plane. Figure 30d shows a cutout of the region of interest from the CFD simulations. Two injectors, an instrumentation port, and prechamber injector are all out of plane to the image. The far-field boundary condition at the exit (right of image) is cropped for aesthetics.

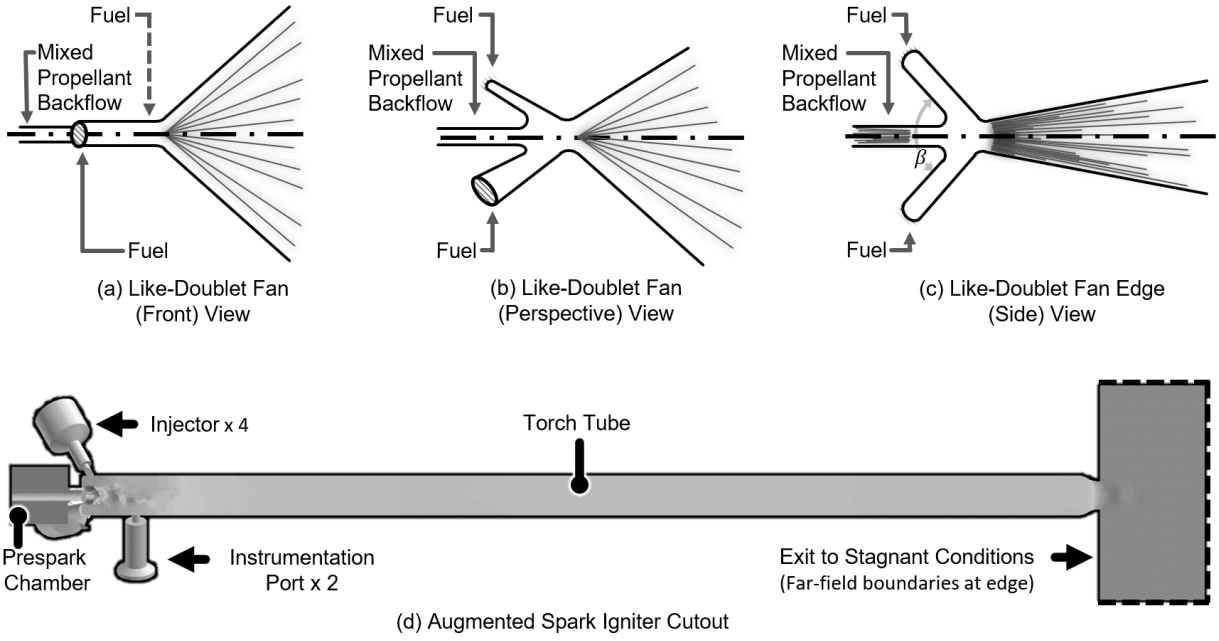


Figure 30 – Rotated sketches of like doublets (impinging jet injectors) are shown from (a) to (c).2,3 The relevant cutout of the flow domain is shown in (d).

A more detailed schematic of the igniter flow field and geometry is presented in Figure 31, with geometric distances represented by *d*. The fuel injector shown in Figure 30 correlates to subscripts 1 and 2 in Figure 31c. The oxidizer injector is represented by subscripts 3 and 4 in the same figure. Intraelement

spacing is denoted by subscripts 5 and 6, and the impingement point separation corresponds to subscript 7. The spark gap distance is represented by subscript 8, the torch tube diameter by 9, and the element height offset by 10. Two pairs of like-doublet injectors are used in the pseudo-pentad design shown in Figure 31. The fluid expansion in the sketch is overemphasized for reader clarity, and the real-world dispersion aligns with the flow fields depicted in Figure 30a–c. A central annular flow is shown in Figure 31 and acts as a fluid dynamic barrier (i.e., causing secondary impingement), widening dispersion of the fan in the plane normal to the injector centerlines. The polar angle of the injectors is represented by $\alpha$ and doublet impingement angle by $\beta$.

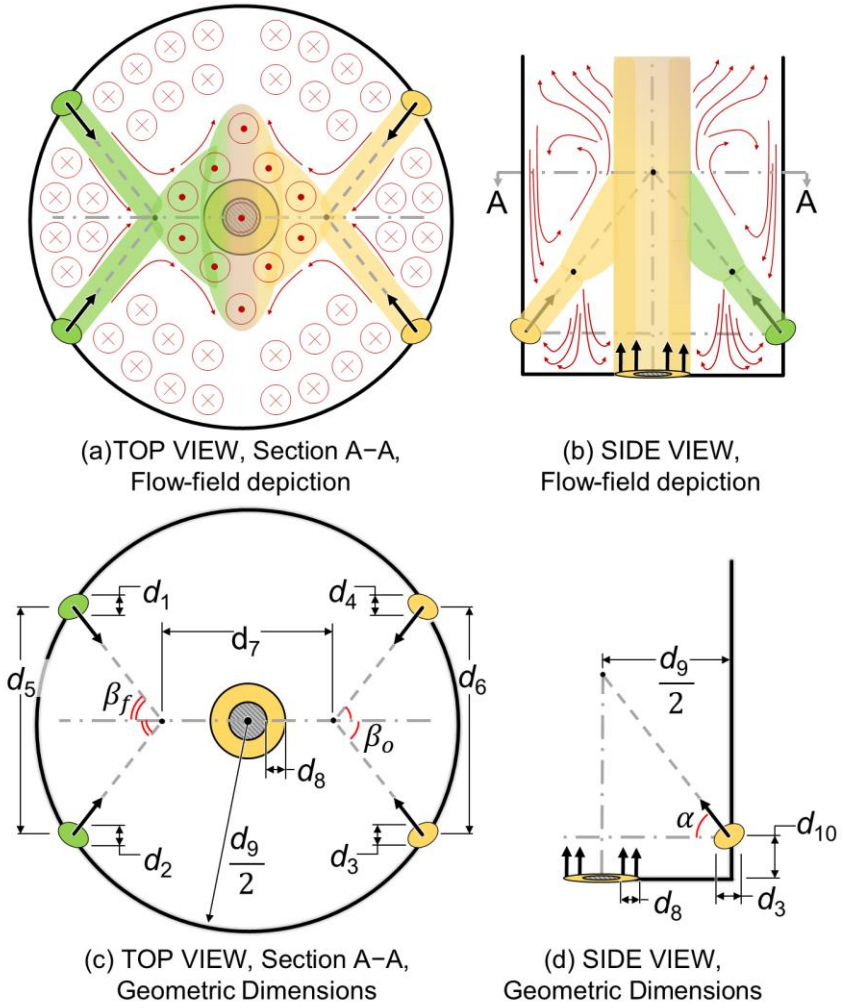


Figure 31 – The flow field is illustrated in (a) and (b) from a top-section and side view, respectively. Circles with a concentric point denote flow out of the page. Circles with a centered x denote flow into the page. Geometric dimensions are shown in (c) and (d) from the aforementioned perspectives.

An underexpanded jet exiting the central annulus is present when flow chokes within the spark gap. This is due to formation of a vena contracta, which creates a fluid dynamic nozzle that may be observed in high-pressure diesel injectors and other practical applications [71]. The diesel injectors referenced are constant-area circular tubes preceded by a large chamber. Flow in the chamber contracts to enter the tubes, leading to flow separation at the entrance. The separation and local recirculation zones cause flow contraction to an area smaller than the tube diameter, hence creating a fluid dynamic nozzle. The flow chokes and accelerates to supersonic conditions where expansion and contraction waves are observed up to the exit. This fluid dynamic pattern is also observed within the constant-area injectors for fuel and oxidizer for the augmented spark igniter. For both annular and constant-area tube flows that choke, an underexpanded jet forms at the channel (or tube) exit and develops supersonic structures.

The flow internal to the annulus channel affects not only downstream fluid dynamic properties but also, potentially, the electric discharge location of the spark gap. Both theoretical and experimental studies have shown that the breakdown voltage is influenced by the pressure-distance product [24, 48]. Due to the vena contracta and subsequent acceleration of the flow to supersonic velocities, the pressure is lowest part of the way down the spark gap channel. Oblique shocks standing within the spark gap create nonuniformity of pressure profiles, which is hypothesized to affect the spark location. The question of dominating factors arises: Is the concentration of charge at the corners [52, 72, 73] of the electrode and the igniter body (i.e., the exit and entrance) a greater influence for breakdown than the reduced pressure-distance product? A definitive answer requires substantial analysis and is outside the scope of work at hand. The effects of the pressure-distance product are examined here under the assumption that the pressure-distance product is influential due to the variability of installation tolerances, surface wear, and other factors that could mitigate the impact of electrical charge concentrations at corners of the electrode or igniter body.

## METHODOLOGY

Nonreacting simulations were performed with Loci/CHEM, a C++ density-based fluid solver [68, 69]. First-order backward Euler time integration with local time stepping was used for steady-state solutions,

followed by a second-order, three-point backward time integration scheme for time-accurate solutions. Menter's Shear Stress Transport (SST) model was used for modeling turbulence, and the Nichols-Nelson hybrid Reynolds-averaged Navier-Stokes/Large-Eddy Simulation (RANS/LES) model was used for SST models for multiscale calculations. A symmetric Gauss-Seidel fluid linear solver was employed. Full details of the numerical approaches and equation formulation are discussed in the Loci/CHEM user manual. The analysis in this paper is an extension of the previous chapter and relevant nondimensional variables are shown in Table 5. These Buckingham Pi ($\pi$) groups are largely dependent on geometric properties, except for the injector mixture ratio ($MR_i$). The injector mixture ratio is a pseudo-physical variable based on the mass flows solely from the doublet injectors and not the spark gap injector. It is calculated by Equation 15, which results from algebraic manipulation of radial momentum conservation. A full discussion of the methodology, numbering schemes, and variable derivations can be found in the Objective Functions for Design and Dimensional Analysis section of Chapter 3.

$$MR_i = \frac{\dot{m}_{o,i}}{\dot{m}_{f,i}} = \left(\frac{d_{o,i}}{d_{f,i}}\right)\left(\frac{\cos(\beta_f)}{\cos(\beta_o)}\,\frac{\rho_{o,i}}{\rho_{f,i}}\right)^{0.5} \tag{15}$$

Table 5 – Relevant $\pi$-groups used from Chapter 3.

| $\pi$-groups | | Subscript | Parameter |
|---|---|---|---|
| $\pi_{1}$ = | ~~$V$~~ / $d_f^3$ | $f$ | Fuel Stream |
| $\pi_{3}$ = | $(\rho_f V_f d_t)/\mu_f = Re$ | $i$ | Injectors |
| $\pi_{7}$ = | $d_f / d_o$ | $o$ | Ox Stream |
| $\pi_{11}$ = | $d_f / d_s$ | $s$ | Spark Gap Width |
| $\pi_{12}$ = | $d_f / d_t$ | $t$ | Tube Diameter |
| $\pi_{13}$ = | $MR_i$ | | |

Twenty cases were simulated with varying mass flow rates and injector geometries using the flow domain shown in Figure 30. All other geometries were held constant, and inlet and outlet conditions were at standard temperature. Simulation accuracy required convergence of mass flow rates for each inlet to be within 5% of the input target. A list of simulation parameters is found in Table 6, where d is diameter or distance, $MR_i$ is injector mixture ratio, *Re* is the analytic Reynolds number. Cases are sorted first by geometry (Gx.y, second column), which is based on the injector geometry (x) and spark gap width (y), and

second by flow rate (*Re* or $\pi_3$, third column). All cases were nonreacting. The fuel used was methane with oxygen as the oxidizer. Inlet conditions were ambient temperatures with a fixed mass flow rate and species concentration. All interelement geometries (spacing, angle, and offsets) were held as constants for this study. Mass flow rates from injectors were determined by momentum ratios. The momentum ratios were balanced to result in a purely axial flow between like-doublet injectors (injectors 1 versus 2 and injectors 3 versus 4) and the opposed like-doublet elements (like-doublet element 1, 2 versus like-doublet element 3, 4).

Table 6 – Geometry and flow rates for all simulations; a single asterisk denotes the compressible flow category without sonic velocities; two asterisks denote Mach ring core flow; cases without have Mach disk core flow. See Chapter 3, Objective Functions for Design and Dimensional Analysis for remaining Buckingham-pi variables.

| Case | Geo. | Re | $d_f/d_o$ | $d_f/d_s$ | $d_f/d_t$ | $MR_i$ / $MR_{ref}$ |
|---|---|---|---|---|---|---|
| [-] | [-] | [ $\pi_3$ ] | [ $\pi_7$ ] | [ $\pi_{11}$ ] | [ $\pi_{12}$ ] | [ $\pi_{13}$ ] |
| G1, *Re* 10k* | 1.0 | 10,000 | 0.28 | 0.54 | 0.05 | 0.125 |
| G1, *Re* 40k** | 1.0 | 40,000 | 0.28 | 0.54 | 0.05 | 0.125 |
| G1, *Re* 140k | 1.0 | 140,000 | 0.28 | 0.54 | 0.05 | 0.125 |
| G1.1, *Re* 140k | 1.1 | 140,000 | 0.28 | 0.24 | 0.05 | 0.125 |
| G2, *Re* 18k** | 2.0 | 18,000 | 0.23 | 0.43 | 0.04 | 0.150 |
| G2.1, *Re* 140k | 2.1 | 140,000 | 0.23 | 0.19 | 0.04 | 0.150 |
| G3, *Re* 26k** | 3.0 | 26,000 | 0.20 | 0.43 | 0.04 | 0.175 |
| G4, *Re* 34k** | 4.0 | 34,000 | 0.18 | 0.43 | 0.04 | 0.200 |
| G5, *Re* 40k** | 5.0 | 40,000 | 0.16 | 0.43 | 0.04 | 0.225 |
| G5, *Re* 140k | 5.0 | 140,000 | 0.16 | 0.43 | 0.04 | 0.225 |
| G6, *Re* 50k | 6.0 | 50,000 | 2.20 | 1.90 | 0.17 | 0.015 |
| G6.1, *Re* 140k | 6.1 | 140,000 | 2.20 | 0.84 | 0.17 | 0.015 |
| G7, *Re* 73k | 7.0 | 73,000 | 0.95 | 0.43 | 0.04 | 0.038 |
| G7, *Re* 140k | 7.0 | 140,000 | 0.95 | 0.43 | 0.04 | 0.038 |
| G7a, *Re* 140k | 7a.0 | 140,000 | 0.95 | 0.56 | 0.11 | 0.038 |
| G8, *Re* 96k | 8.0 | 96,000 | 0.61 | 0.43 | 0.04 | 0.058 |
| G9, *Re* 119k | 9.0 | 119,000 | 0.45 | 0.54 | 0.05 | 0.080 |
| G9, *Re* 140k | 9.0 | 140,000 | 0.45 | 0.54 | 0.05 | 0.080 |
| G10, *Re* 140k | 10.0 | 140,000 | 0.35 | 0.54 | 0.05 | 0.100 |
| G10.1, *Re* 140k | 10.1 | 140,000 | 0.35 | 0.24 | 0.05 | 0.100 |

## RESULTS AND DISCUSSION

For the igniter, the spark gap is not a linear volume between two planar conductors but instead an annular region (i.e., rod and cylinder). The annulus is formed by a solid cylindrical electrode located within a concentric region of the upstream torch igniter body. The chamber preceding the annulus contains the spark igniter and an entry port for the oxidizer. The air gap within the annulus electrically insulates the torch igniter body from the spark igniter electrode, which sits flush with the forward-end wall of the torch tube chamber as depicted in Figure 32a. Note that there is only one chamber inlet for the oxidizer. This creates an asymmetric pressure distribution and flow field prior to the fluid entering the spark gap channel that is located upstream of the annulus. To show this effect, cross sections of the spark channel are taken at six locations (Figure 32b) and discussed later. A streamline plot depicting the uneven flow paths in the prespark chamber is shown on the left-hand side of Figure 32c.

To aid reader internalization, the analysis is divided into three categories: (1) compressible, subsonic core flow; (2) Mach ring core flow; and (3) Mach disk core flow. Datasets are placed in each category based on the bulk Mach number. Compressible, subsonic flow is true to its name, and at no point are sonic conditions present within either the spark gap annulus or the torch tube. In contrast, local subsonic-to-supersonic flows may be present in the Mach ring and Mach disk categories, and the labels are pedantic misnomers. However, for the sake of analysis, these categories easily and neatly divide the unique flow structures observed.

A vena contracta is present in the annulus, and the flow accelerates through the virtual nozzle in the spark gap for all cases. For the compressible, subsonic flow category, neither the bulk flow nor the local regions reach sonic conditions. For both Mach ring and Mach disk categories, the flow chokes due to the vena contracta and accelerates to supersonic conditions, as noted in Figure 32b. Oblique shocks are observed throughout the remainder of the spark gap annulus until the fluid enters the torch tube chamber as an underexpanded, annular jet.

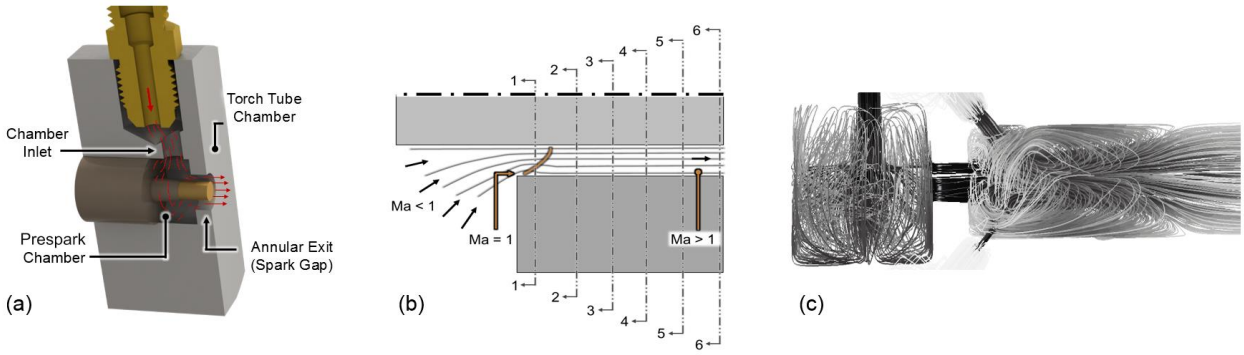


Figure 32 – (a) An illustration of the spark gap and associated spark igniter at the head of the torch tube; (b) cutout of the annular exit (spark gap channel), relevant section view locations (1-1 to 6-6), and sketch of vena contracta location where flow enters the spark gap; and (c) sample streamline plot depicting recirculation due to the low-pressure region at the head of the tube and flow asymmetry within the prespark chamber.

The Mach ring and Mach disk flows resemble periodic snapshots of the flow exiting a rotating detonation engine (RDE), where the flow exiting the annulus radially expands over the center body (viz., the inner electrode for the study at hand) and cowl base (viz., the outer electrode or igniter head) before coalescing into a normal shock [74, 75, 76]. Unlike in RDE applications, [REDACTED]. The flow from the spark gap annulus does not have a rotational component and is largely uniform in structure.

The flow within the spark gap is as important as the flow within the main torch tube chamber. Variance in pressure profile both azimuthally and longitudinally (see Figure 33) may have substantial impact on the spark discharge properties. The flow accelerates as it passes through the vena contracta to reach supersonic conditions for all cases except for the upper-left example. This is evident by the expansion and contraction waves that form downstream of the conical Ma 1 surface around the annulus. The waves are asymmetrically distributed along the azimuth due to the singular injector employed for the prespark chamber and the resulting pressure concentration.

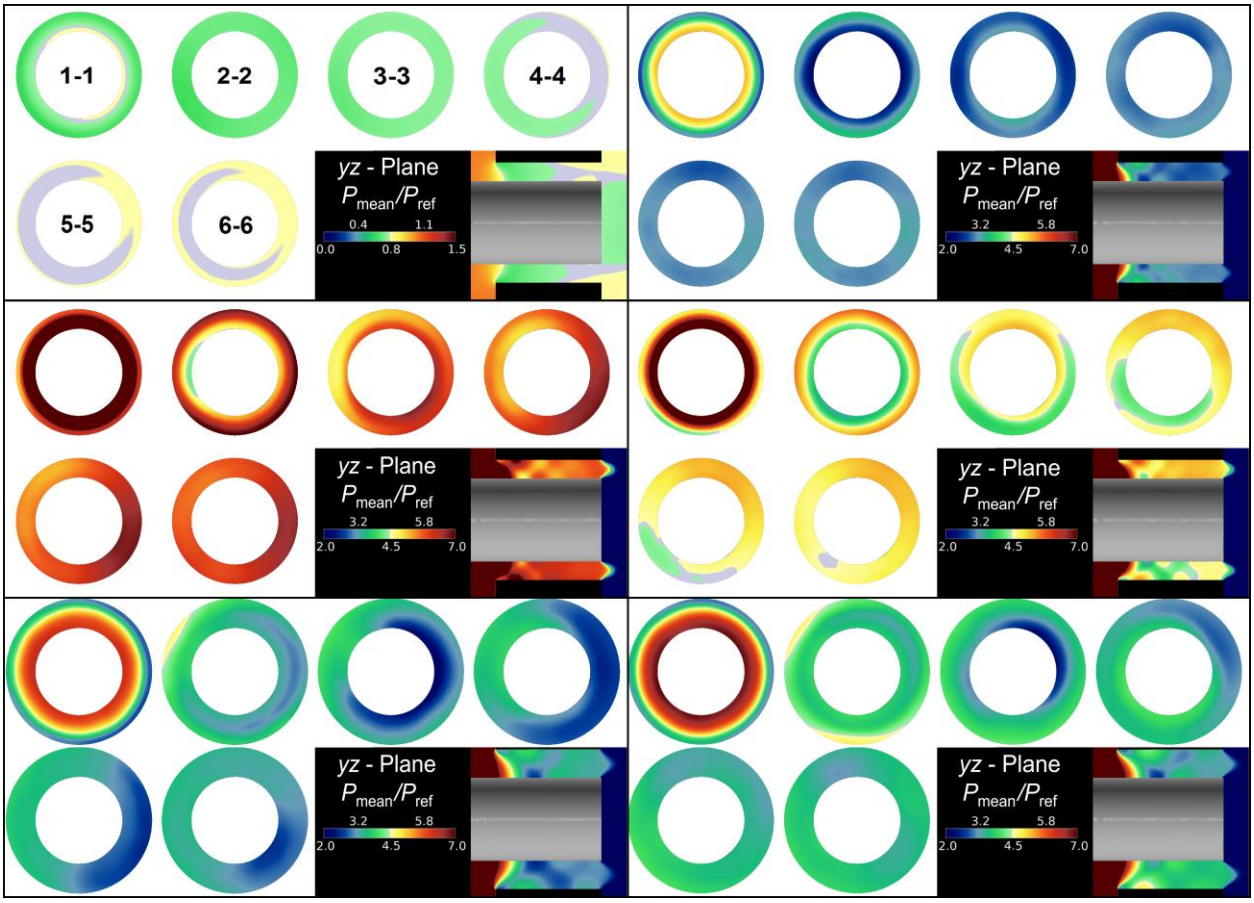


Figure 33 – Lateral cross-section views of the spark gap and a longitudinal cross section on the yz-plane. Axial locations (1-1 to 6-6) are referenced in Fig. 3b. Cases shown are (row 1) G1.0, Re 10k (left); G7.0, Re 73k (right); (row 2) G7.1, Re 140k (left), G9.0, Re 119k (right); (row 3) G10.1, Re 140k (left); and G6.1, Re 140k (right) from Table 2.

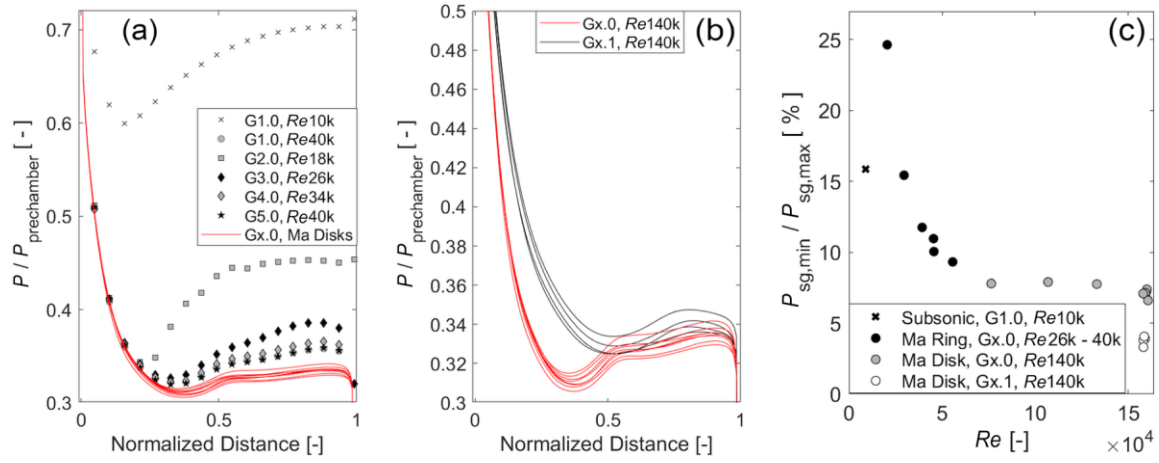


Figure 34 – (a) Normalized plots of spark gap pressures for cases with the baseline spark gap width; (b) comparison of normalized pressure curves for baseline spark gap width and enlarged spark gap width; and (c) min-max pressure ratio within the spark gap for all cases versus the Reynolds number.

Bulk pressure curves versus axial spark gap length are shown in Figure 34a and b, where the bulk pressure is an average of a cylindrical slice at a given longitudinal (z-axis) location. Zero distance is the entry to the spark gap, and pressures are normalized to the pressure of the prespark chamber. Cases appear to asymptotically approach a pressure ratio of 0.33 as the flow rate increases for a constant-width spark gap. Increasing the spark gap width decreases the effect of the vena contracta on the pressure variance but does not hinder the formation of a shock and supersonic flows. A comparison of the pressure ratios to Mach tables provides accurate results for bulk Mach numbers as expected. Based on these tables, the effective nozzle area for the spark gap at the vena contracta is [REDACTED] than the throat area.

One of the most important properties for spark discharge is the breakdown voltage, which is a function of the pressure-distance product of the spark gap. Using Paschen's curve as the baseline approximation, breakdown voltage increases linearly with the pressure-distance product for the practical operating conditions previously studied [24, 47]. Electrical discharge will occur across the lowest energy path (assuming equal charge concentrations) and consequently where the breakdown voltage is lowest. Logically, an asymmetric pressure distribution may cause spark discharge to occur more frequently at low-pressure regions and favor select locations within the annulus.

Depending on the electrical design of a spark exciter, the breakdown voltage could vary between and potentially outside of 4–8 kV as observed when using a capacitive-style exciter with spark gaps of 0.020–0.091 in. from 20 to 500 psia with oxygen [47]. Recalling the (local) linear relation between breakdown voltage and the pressure-distance product, a 1% change in pressure or distance would equate to a change of 40–80 V. Bulk pressure values within the spark gap vary between 5–25% (Figure 33 and 34c), which would translate to a difference of 200–400 V and 1000–1600 V at each end of the spectrum. Note the relative importance of high-cycle fatigue and manufacturing errors in comparison to this phenomenon. For a spark gap that is 0.030 in. wide, misalignment or erosion of a single thousandth of an in. equates to a 3% difference in width (difference of 120–240 V). Pressure variation within the spark gap is one of many variables and on an order of magnitude that should not be dismissed outright.

The supersonic structures exiting an annular channel have characteristics different from an underexpanded jet exiting a constant-area tube despite their resemblance. Underexpanded jets are well studied, and the resulting flow expansion and contraction, normal shocks, and oblique shocks to follow are common knowledge to the propulsion community. The flow exiting an annulus is less well studied, with the closest known example being RDEs with blunt center bodies. The flow exiting the channel forms a normal shock "line" downstream of the channel. The shock for an RDE is spatially transient as it follows the detonation wave within the channel [75]. The shock for the spark gap of the CASI is present at all locations following the channel and forms a Mach ring. The ring is concentric with the spark annulus, but at a slightly smaller radius as the flow cants toward the center body during expansion. This is due to the low-pressure region created over the center body by the surrounding high-velocity flow. The strength of the normal shock of the Mach ring dictates the downstream properties.

Two outcomes are observed. First, for lower flow rates studied, and therefore weaker shocks, the oblique shocks intersect and form additional Mach rings, each with a slightly smaller diameter than the previous ones. The second feature is observed for stronger shocks where the subsequent oblique shocks interact across the center body. The oblique shock waves following the Mach ring can coalesce and form a Mach disk farther downstream. Oblique shock trains follow the Mach disk much like those observed in underexpanded jets from constant-area tubes [77] and in supersonic plumes [78, 79]. Differences in flow structure are shown in Figure 35a (Mach ring) and b (Mach disk).

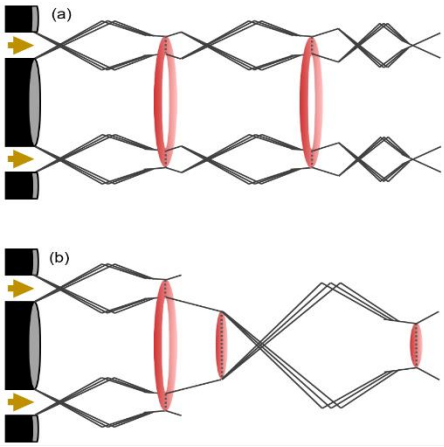


Figure 35 – Illustrations of the (a) Mach ring and (b) Mach disk flow structures observed.

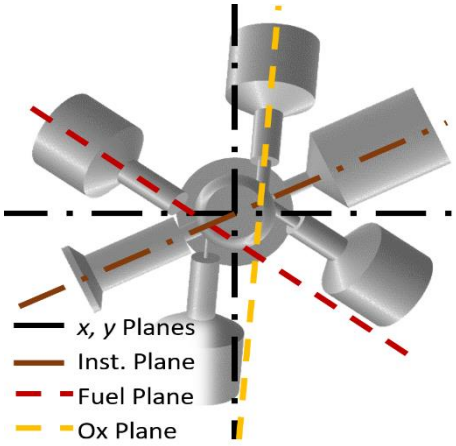


Figure 36 – Section views of the augmented spark igniter. The z-axis is normal to the page.

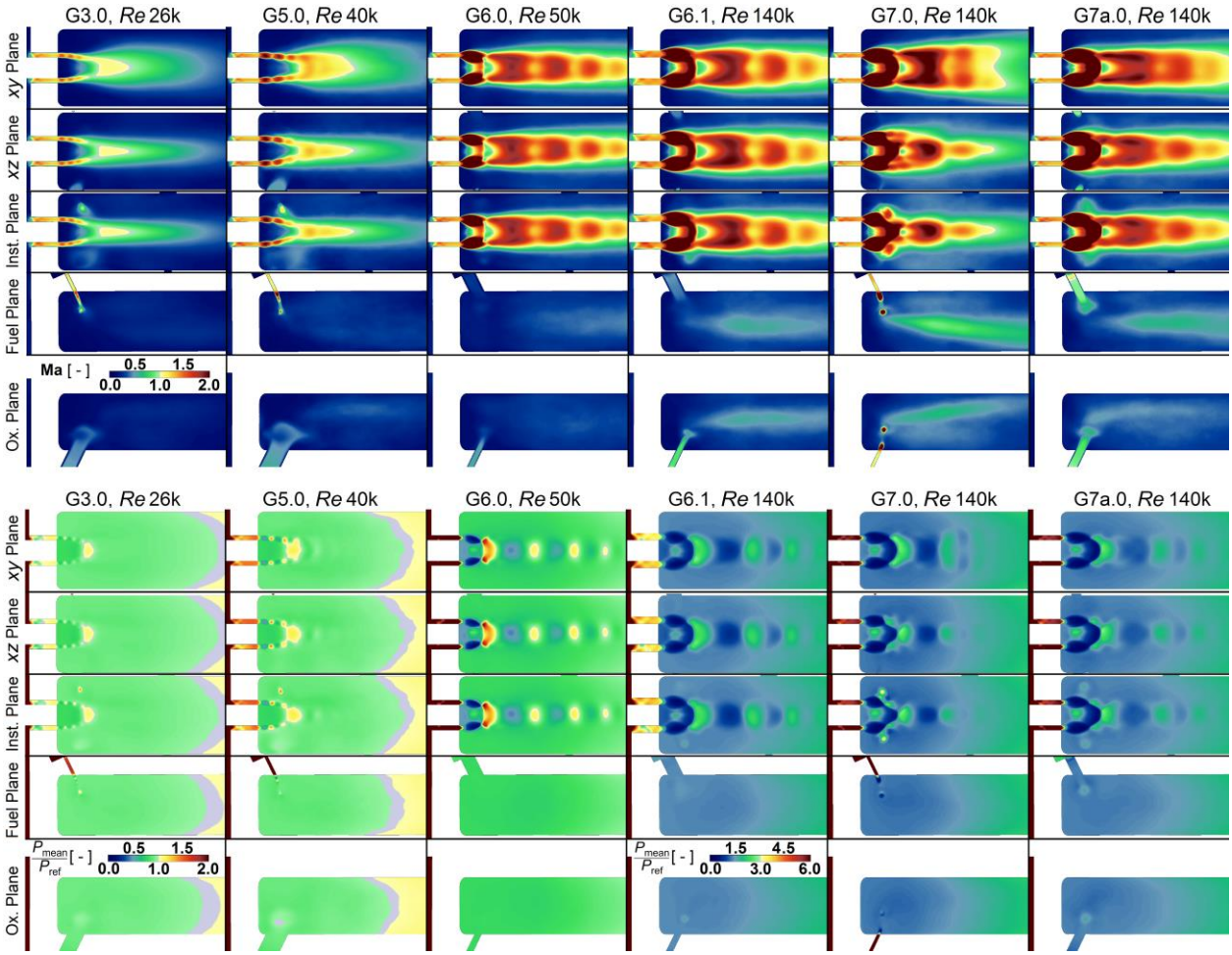


Figure 37 – Section views of select cases depicting Mach ring flow (left two columns) and Mach disk flow (right four columns) with both Mach plots (upper half) and normalized pressure plots (lower half).

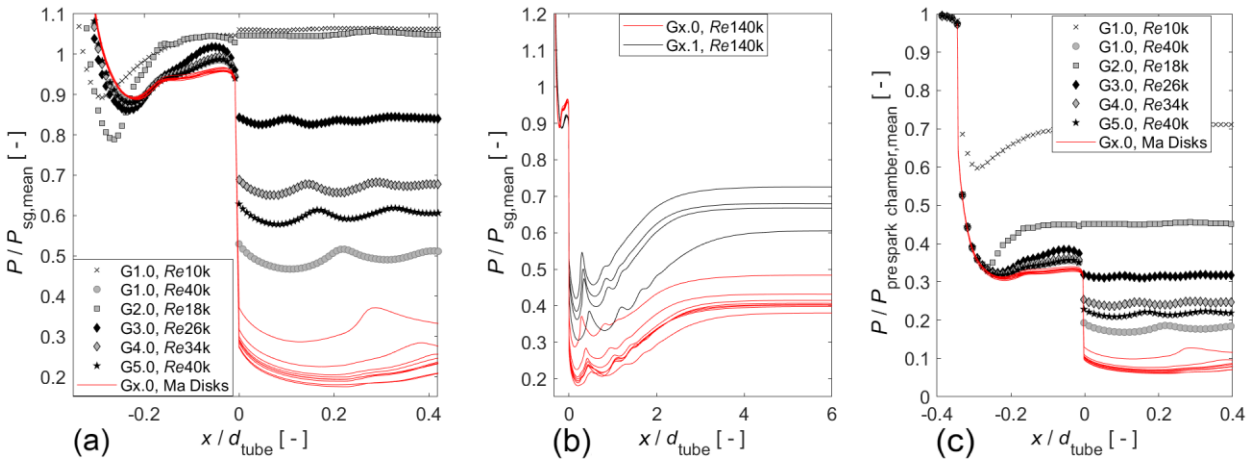


Figure 38 – (a, b) Comparison of pressure profiles normalized to the mean spark gap pressure and (c) to the mean prespark chamber.

The torch tube is divided into five cross sections as shown in Figure 36, and the Mach and pressure profiles of each are seen in Figure 37. Cases are arranged by increasing Reynolds number from left to right. Cases G3.0 and G5.0 have Mach ring flow structures, and all remaining cases contain Mach disk structures. The defining property between each structure is solely the mass flow rate through the spark annulus. Injector sizes and ratios affect the downstream plume, but do not cause a transition between Mach disks and Mach rings. The upper and lower bounds of the Mach plots are artificially limited to show subsonic flows as cool colors and supersonic flows as warm colors. All plots use the same Mach color bar. Local Mach numbers in the torch tube reach and surpass Mach 4 for higher flow rates. Within the spark gap for the flow rates simulated, Mach 1.2 is the typical ceiling.

The Mach ring structure is conical with the decreasing radius oriented downstream. As flow rate from the spark gap annulus increases, the Mach ring cone structure shrinks longitudinally. A transition occurs between *Re* 40k and 50k from the Mach ring structure to a Mach disk structure. The differences in structures are clearly shown through the pressure and Mach plots of Figure 37. After the transition to a Mach disk structure, increasing flow rate will cause the first Mach disk to change into a spherical dome shape. This is seen in G6.1, G7.0, and G7a.0 of Figure 37 for the instrumentation, yz- and xz-planes.

Pressure profiles for the smallest spark gap studied, normalized to the mean spark gap pressure, show an asymptotic relation to 20% of the spark gap pressure and roughly 10% of the mean prespark chamber pressure. This is observed in Figure 38a and c, respectively. The effects of increasing the spark gap width are shown in Figure 38b, where the pressure recovery is greater following the spark gap. Higher flow rates with larger spark gap widths are speculated to approach the same pressure limit (10% of prespark chamber) and retain similar flow structures.

The time-averaged shape of the Mach disk (plane, dome, or otherwise) would be perfectly symmetric without external perturbations. However, the fuel and oxidizer doublet elements impinge on opposing sides of the longitudinal Mach structures (c.f. Figure 31). The impingement plane between the injector elements is on the instrumentation plane (third row of Figure 37) and shows the greatest deformation in the structure of the Mach disk. Differences between G7.0 and G7a.0 show the effect of the injector diameters (smaller

injectors create larger distortions) on Mach disk structure as each are simulated with the same bulk flow rate (*Re* 140k).

Geometry 7x, *Re* 140 has the same mass flow rate for all injectors to the torch tube. The difference between geometries 7 and 7a represents a proportional increase in the size of both the oxidizer and fuel injector diameters. The smaller injectors (G7.0) are more disruptive to the central flow, compressing it in one plane and widening it in the perpendicular plane. This is best observed in the yz- and xz-planes shown in Figure 37, which are spatially referenced from Figure 35a. Smaller-diameter injectors pierce the central flow and retain a fair amount of their radial momentum. The impacted flow may then impinge on the opposing wall creating uneven local heating of the chamber walls downstream.

The size of the injectors and the total flow rates are equally important to mixing. Mixtures closer to stoichiometric conditions are inherently easier to ignite and have higher adiabatic flame temperatures. The adiabatic reaction temperature is plotted for reference in Figure 39 with the melting point of Inconel 625 as a function of the mass fraction of methane. The flammable zone of the mixtures is subdivided into three methane mass fraction regions with similar temperature ranges for analysis. As the core mixture is fuel lean for these simulations, skirting the lower flammability limit, the reaction temperature should be near 1500 K. Ignition in such a mixture is virtually impossible, [REDACTED].

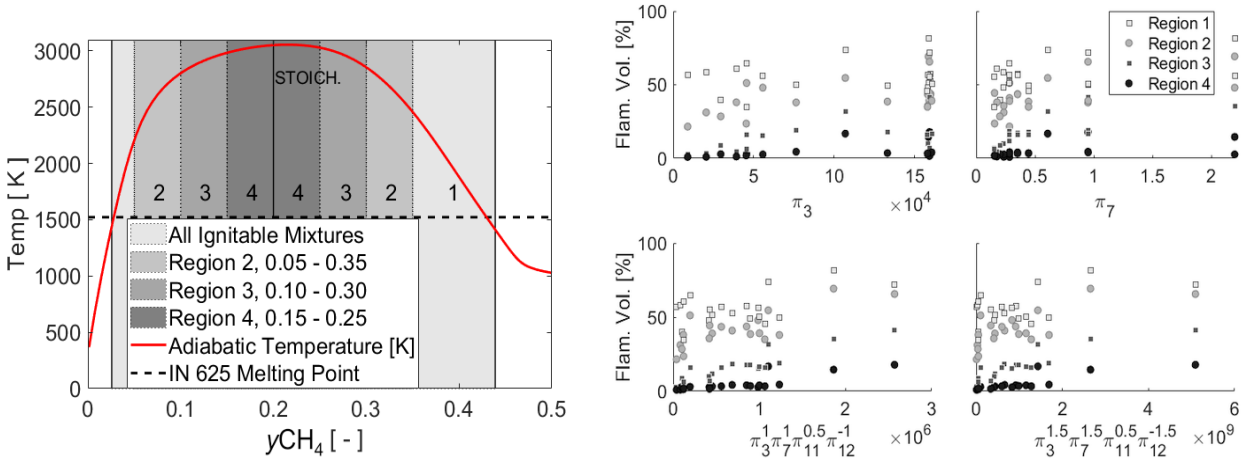


Figure 39 – Adiabatic equilibrium flame temperature and flammability zones used for analysis (left), and the flammable volume of fluid for each flammability zone (right) versus select variables within one-half-tube diameter of the spark face.

The volume of fluid within one-half-tube diameter of the spark face is then the most relevant location where ignitable mixtures are necessary based on prior examination of spark discharge studies [47]. The percentage of this volume within each region is plotted in Figure 39 (right) where π-groups are defined in Table 5. The flammable volume generally increases with the increasing Reynolds number ($\pi_3$), yet the plot shown is influenced by several other variables. The flammable volume appears to increase with higher ratios of fuel-to-oxidizer diameter ($\pi_7$). Other relevant variables are the ratio of the annular spark gap width to the fuel injector diameter ($\pi_{11}$), and the torch tube to the fuel injector diameter ($\pi_{12}$) ratio. The overall volume within the full flammability limits is largely unaffected, but select exponentiated combinations of these nondimensional groups lead to increased volumes of local, near-stoichiometric mixtures.

To provide a more intuitive sense of how mixing is affected by diameter ratios and the Reynolds number, select section views are provided for the mass fraction of methane in Figure 40. Injector size relative to tube size is clearly a dominating factor for fluid dispersion. Cases 7 and 7a are a perfect example of this. Again, both cases have the same mass flow rates from all injectors; however, the fuel injector size for 7a is larger and leads to a wider and more even dispersion of methane. This result aligns with the expectations for injector behavior when examining jets in a perpendicular crossflow, where jet penetration of a crossflow and mixing efficiency increase with the injector diameter [56]. While the spark gap width is different between cases 6 and 6.1, the larger flammability zone created by increasing the Reynolds number is readily observed.

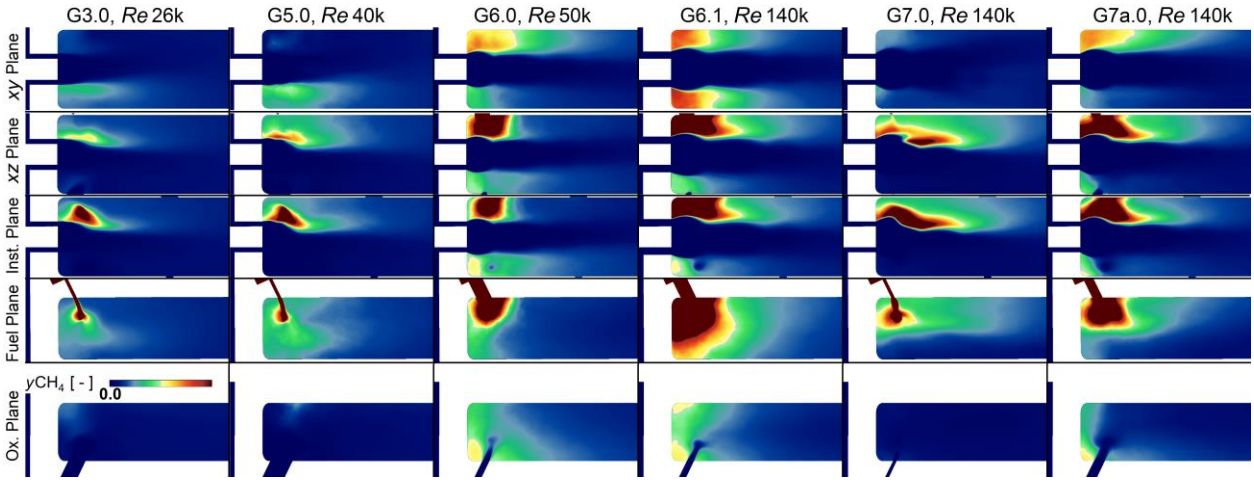


Figure 40 – Section views for the mass fraction of methane.

## CONCLUSIONS

Twenty nonreacting, gaseous flows were examined for a pseudo-pentad CASI igniter. Injector diameter ratios, local mixture ratios, and mass flow rates were varied to examine the effects on local mixing and internal flow structures. Three flow regimes were observed: compressible, subsonic flow; Mach ring flow; and Mach disk flow. The flow structures are primarily dependent on the mass flow rate from the spark gap annulus, and subsidiary differences are caused by relative sizes (and thus flow momentum) of doublet injector elements.

Pressure profiles within the spark gap are asymmetric along all dimensions (viz., radial, azimuthal, and longitudinal). Longitudinal and azimuthal differences potentially impact the spark discharge location in situ, leading to preferential spark locations on a specific side of the annulus or at a given distance spanning the spark gap axial length. The impact of irregular pressure distribution is on the order of magnitude of misalignment errors, machining tolerances, and high-cycle fatigue wear. Consequently, it is one of many factors impacting the spark discharge location and does not demand prioritization.

The region studied was within one-half-tube diameter of the spark gap face, as the location is where energy is (likely) imparted for ignition. The overall volume of flammable gas did not change significantly, as the total fuel/air ratio was held constant. Local mixture ratios, however, were conclusively affected by geometric dimensions and flow rates. In computational analysis, the volumes of local, near-stoichiometric

mixtures increased as a function of exponentiated nondimensional variables (viz., *Re* number and geometric ratios). These computational studies observed that higher flow rates and larger fuel orifices were the most influential factors for increasing local, near-stoichiometric mixtures, followed by smaller tube diameters and larger spark gap widths.

# CHAPTER 5:
# AUGMENTED SPARK IMPINGING PSEUDO-PENTAD IGNITER – AN EXPERIMENTAL IGNITION STUDY

## INTRODUCTION

Augmented spark (torch) igniters have been used to light liquid rocket engines ranging from small 445 N (100 lbf) thrust reaction control engines to the illustrious Space Shuttle main engine, which is rated at 2,090,000 N (470,000 lbf) thrust at vacuum [80, 81]. Their use was shown to improve the reliability of engines such as the RL10E-1 over traditional spark ignition methods [82], and they were used not only to light main combustion chambers but also preburners that provide energy to the turbine drive gases [81]. Unlike other combustion devices (nozzles, thrust chambers, injectors), where the design may be guided by analytical models derived from nontrivial test campaigns [15, 57], augmented spark igniters have lacked an analytic design guide and often rely on iterative engineering design cycles for advancement [67].

This dissertation has sought to fill this gap of knowledge by producing objective functions that provide a scalable solution to a specific style of igniters[3,4] - augmented spark impinging igniters. For this igniter, two sets of like-doublets (one set for the fuel, one for the oxidizer) are located on opposing walls of the igniter and impinge on a coaxial oxidizer flow. The coaxial injector is annular in shape with the inner rod formed by an electrode and the outer cylinder by the base of the torch tube.

Doublet injector elements are the simplest means to mix two fluids and consist of two streams impinging on a single point. These elements may have the same propellant from each orifice (like-doublets) or have one orifice for the fuel and oxidizer respectively (unlike-doublets). They are noted for their dependability, stability, mixing efficiency, and simplicity to manufacture [55]. Studies of these injector elements have produced an operational range of relevant variables (e.g., fan spacing, inclination angles,

[3] D. C. Tinker, B. R. Richardson, R. J. Osborne, R. W. Pitz and J. S. West, "Internal Flow of an Augmented Spark Impinging Pseudo-Pentad Igniter," *JANNAF Journal of Propulsion and Energetics*, vol. 20, no. 1, pp. 105-116, 2020.

[4] D. C. Tinker, B. R. Richardson, R. J. Osborne, R. W. Pitz and J. S. West, "Computational Verification of Objective Functions for the Design and Development of Nondimensional Mixing Correlations for a Liquid Rocket Engine Augmented Spark Impinging Pseudo-Pentad Igniter," *JANNAF Journal of Propulsion and Energetics*, vol. 11, no. 1, pp. 89-103, 2020.

orifice diameters) [54], design correlations for mixing efficiency, and relations to combustion efficiency [57]. Parallel studies were performed with the addition of a third, fourth, and fifth fluid stream to a single injector element with both like and unlike propellant configurations to characterize their relative effectiveness [55].

Injectors with five fluid streams are aptly named pentad injector elements and have been studied to elucidate combustion stability mechanisms and develop empirical formulas for mixing efficiency [57]. These injectors provide good mixing, excellent atomization, and were well-characterized decades prior; however, there were no known engines that relied on a grouping of pentad injector elements [55]. Unlike a traditional pentad injector element where the fluid streams converge on a single point, the injectors of the augmented spark impinging igniter discussed in this manuscript impinge in three unique points across a single plane. The like-doublet injector elements and their associated impingement points are mirrored across the centerline of the torch tube. The resultant fans then impinge on the central injector flow as shown in Figure 41. An accurate title for this device is therefore an augmented spark impinging *pseudo-pentad* igniter. However, for brevity, it will be referred to as an augmented spark impinging (ASI) igniter hereafter.

Ignition probability is dependent on a variety of factors for any combination of reactants alone and becomes more constrained with application. For ASI igniters, these variables include the reactants, reactant temperatures, pre-ignition chamber pressure, energy delivery (spark characteristics), propellant injection timing, core, and injector (local) mixture ratios, momentum ratios, and injector geometry.

The reactants examined are gaseous methane and oxygen due to the renewed interest for *in situ* propellant production, ease of cryogenic fluid management relative to hydrogen, and high bulk propellant density [83, 6, 84]. A significant difficulty with methane is the constrained flammability limits relative to hydrogen [5]. Fundamental studies of methane combustion by Fotache et al. showed decreased strain rate and higher pressures correlated to lower ignition temperatures [85] and would result in an easier ignition process. However, in application for an ASI igniter, these behaviors would counteract each other in part (viz. higher pressures equate to higher flows and larger strain rates) and likely lead to an insignificant change for the ignition temperature. Spark igniters are used to provide the catalyst for ignition, but the well-

known drawback is that ignition is stochastic in nature for these devices, relying not only on a flammable mixture to pass by but also one where the strain rate does not quench the flame [86]. The strain rate is not only dependent on non-reacting fluid dynamics but also the energy deposition from the spark igniter. A weak spark may not surpass the activation energy whereas an overly strong spark may cause a rapid expansion of gas leading to a shockwave, which quenches the spark by straining and extinguishing the flame kernel [20]. Microsecond spark discharges, as used for this igniter, have been researched in detail with respect to electrode geometry and varying electrical inputs for stagnant conditions to provide insight into fundamental phenomena [37, 39, 40, 41, 42, 43]. Spark studies of high-speed gaseous flows resembling those in annular electrodes, i.e., augmented spark igniters, have shown the spatiotemporal development of spark exhaust plumes [47] and their temperatures [87, 44]. Sforzo et al. provided ignition probability of sparks in stratified crossflow with varying reactant temperatures where the flow near the spark discharge is nonflammable [44]. The breadth of work on spark ignition systems alone shows their importance to ignition probability. The impact of applying spark igniters to a novel system must be reviewed and characterized as achievable.

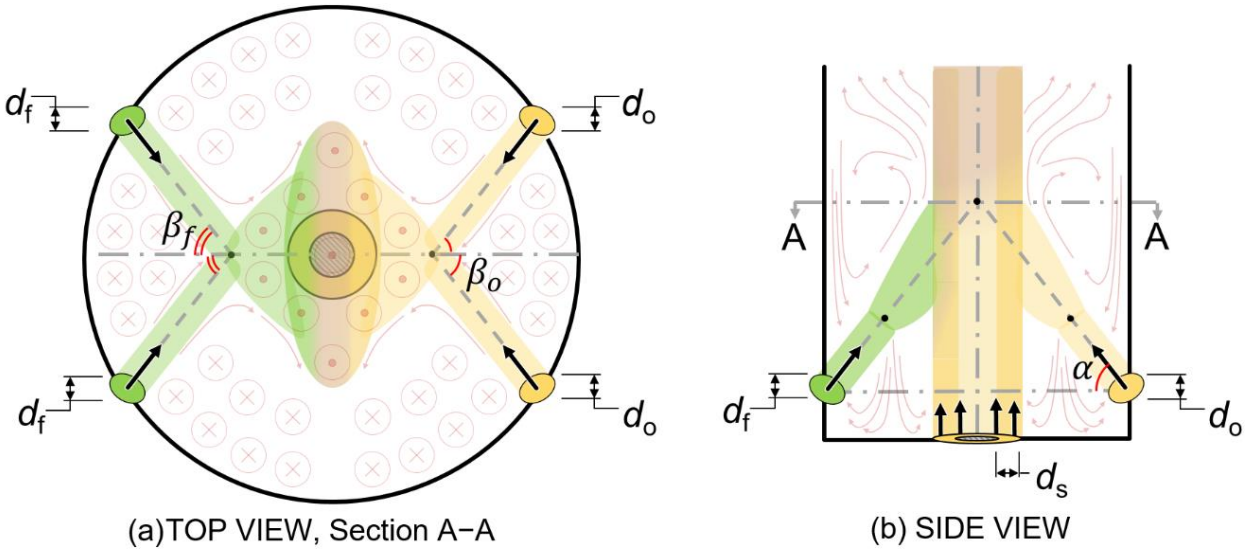


Figure 41 – Injector configuration schematic where yellow injectors (center, right doublet) represent oxygen and green represent fuel injectors (left doublet)

Standalone momentum conservation analyses are used for doublet injectors as a mismatch of the stream diameters and/or stream momentum flux negatively effects mixing and disbursement of the resultant fan [15]. Exponentiated versions of momentum balances have been empirically proven to describe mixing efficiency [55]. Simulations of non-reacting flow provided mixing and mixture length correlations that were functions of nondimensional ratios of injector geometry and fluid properties in the previous two chapters. The geometric and fluid property ratios are contributors to the momentum conservation as shown by Equation 16, which is calculated for the radial momentum factor ($\psi$) of the ASI injector (reference Figure 41) when excluding the central jet from the analysis.

$$\psi = \frac{\dot{m}_{f,i} V_{f,i} \cos(\beta_f)}{\dot{m}_{o,i} V_{o,i} \cos(\beta_o)} \tag{16}$$

The resultant direction of the doublets' secondary impingement is described by this equation, which is the cornerstone of the analytic approach and requires validation. The analytic relations and objective functions for the ASI igniter are developed from a lumped fluid approach to mass and momentum conservation laws coupled with practical constraints, yet are unconstrained with respect to the momentum ratios between injectors. For Equation 16, the value for $\psi$ may be intuitively assumed as one, which implies that the resultant fluid streams travel in a purely axial direction after collision, but presently lacks empirical validation for effectiveness. Similarly, the axial momentum ratio ($\eta$) is unconstrained and is shown in Equation 17 where the ratio is calculated between the central oxidizer flow from the annulus and the axial component of either a fuel or oxidizer injector.

$$\eta = \frac{2}{\sin(\alpha)} \frac{\dot{m}_{o,s}}{\dot{m}_{n,i}} \frac{V_{o,s}}{V_{n,i}} = \frac{2}{\sin(\alpha)} \frac{\rho_{n,\mathrm{i}}}{\rho_{o,\mathrm{s}}} * \frac{A_{n,i}}{A_s} \left( \frac{\dot{m}_{o,s}}{\dot{m}_{n,i}} \right)^2 \tag{17}$$

Unlike the radial momentum balance, where equal momentum resulting in axial flow is desired to prevent uneven heating and preserve hardware integrity, the axial momentum factor has no physical analog for guidance. As with the radial momentum ratio, the axial momentum ratio has not yet been constrained by empirical results. Due to these unknowns, the first aim of this manuscript is to provide experimental results demonstrating what momentum ratios provide increased ignition probability for an ASI igniter.

A comprehensive study of all factors affecting ignition is an ambitious and worthy goal, but realistically must be narrowed. The scope of this paper is limited to sweeps of the core and injector (local) mixture ratios, pre-ignition chamber pressure, momentum ratios, and injector geometry. Given the configuration of the ASI igniter, two mixture ratios are easily varied. The first is the *core* mixture ratio or the ratio of all the oxidizer to all the fuel within the torch tube shown in Equation 18. The second in Equation 19 is a pseudo-physical variable named the *injector* mixture ratio. Experimentally, it is the ratio of only the mass flow rates from doublet injector oxidizer versus the doublet injector fuel. Algebraic manipulation under the constraint that the radial momentum between the fuel and oxidizer injectors are balanced (Equation 4 or $\psi$=1 in Equation 16) gives rise to the injector mixture ratio in terms of the geometric constraints, and fluid properties (i.e., Equation 5). With $\psi$ unbound, the injector mixture ratio would analytically appear as shown in Equation 19.

$$MR_c = \frac{\dot{m}_{o,i}+\dot{m}_{o,s}}{\dot{m}_{f,i}} \tag{18}$$

$$MR_i = \frac{\dot{m}_{o,i}}{\dot{m}_{f,i}} = \left(\frac{d_{o,i}}{d_{f,i}}\right)\left(\frac{\cos(\beta_f)}{\cos(\beta_o)}\,\frac{\rho_{o,i}}{\rho_{f,i}}\frac{1}{\psi}\right)^{0.5} \tag{19}$$

Computational models in the Chapters 3 and 4 predict the effect of varying injector sizes on mixing lengths and flammable gas volumes; Results suggest that objective design functions (c.f., Figure 29) and relations derived from a lumped fluid approach to conservation law analysis (i.e., Equation 5 or Equation 19 for $\psi$=1, c.f. Figure 27) could be used to approximate local mixture ratios.

In this paper, we aim to show how ignition probability is affected by axial and radial momentum factors, effects of pre-chamber pressure, propellant injection timing, igniter geometry, and both core and injector (local) mixture ratios. The results are intended to provide insight into the optimal zone for these parameters and provide constraints for designers.

## METHODOLOGY

A modular torch igniter was designed to emulate the Marshall Space Flight Center (MSFC) in-house augmented spark igniter [17]. A pair of symmetric sets of like-doublets were located on opposing sides of the torch tube and their diameters were adjusted using removable copper inserts. Two injector sets were used to investigate nondimensional variables described in the introduction. The fuel-to-oxidizer injector diameter ratios were 0.45 and 0.25 for *injector set 1* $\left(\frac{MR_i}{MR_{ref}} < 0.15\right)$ and *injector set 2* $\left(\frac{MR_i}{MR_{ref}} > 0.15\right)$. The mixture ratios presented are normalized to the same reference mixture ratio, $MR_{ref}$, and the phrases "fuel-lean" and "fuel-rich" are used as relative terms. $MR_{ref}$ is not disclosed in the manuscript. The injector mixture ratios were fuel-rich for *injector set 1* and fuel-lean *injector set 2* relative to each other but had no effect on the total (core) mixture ratio for the igniter. In other words, for a given core mixture ratio, the same mass fraction of fuel was present in the torch tube regardless of the injector set used. The ratio of oxidizer flowing through the spark gap to the oxidizer flowing through the doublet injector was varied to satisfy the radial momentum balance with the fuel doublet.

The propellant delivery system developed for this experiment is shown in Figure 42. A single supply pressure is used for each of the respective oxidizer and fuel lines. Mass flow rates are regulated through choked flow venturis and allow delivery of propellants at a variety of pressures and mass flow rates to the ASI igniter. Pressure values are normalized to $P_{ref}$, which is not disclosed in the manuscript. Nominal pressure ratios and temperatures across venturis were used to calculate mass flow using the choked flow equation (Equation 20) when below the critical pressure ratio (calculated with Equation 21). When above the critical pressure ratio, mass flow was determined by Equation 22 for compressible flow through an orifice.

$$\dot{m} = \frac{A\,P_t}{\sqrt{T_t}}\sqrt{\frac{\gamma}{R}\left(\frac{2}{\gamma+1}\right)^{\frac{\gamma+1}{\gamma-1}}} \tag{20}$$

$$\frac{P_2}{P_1} \leq \left(\frac{2}{\gamma+1}\right)^{\frac{\gamma}{\gamma-1}} \tag{21}$$

$$\dot{m} = C_d\, A \sqrt{2\rho_1\, P_1 \left(\frac{\gamma}{\gamma-1}\right)\left[\left(\frac{P_2}{P_1}\right)^{\frac{2}{\gamma}} - \left(\frac{P_2}{P_1}\right)^{\frac{\gamma+1}{\gamma}}\right]} \qquad (22)$$

Pressure transducers (Omega PX603 series) were accurate to ±5 kPa upstream of the venturi and ±0.5 kPa downstream. Thermocouples were all exposed junction 1.575-mm Type-K air probes with Inconel 600 sheaths accurate to ±2.2℃. Uncertainty calculations for mass flow were 0.3% for choked flow and 0.2% for unchoked conditions, which were used to calculate mixture ratio uncertainty at 0.4%.

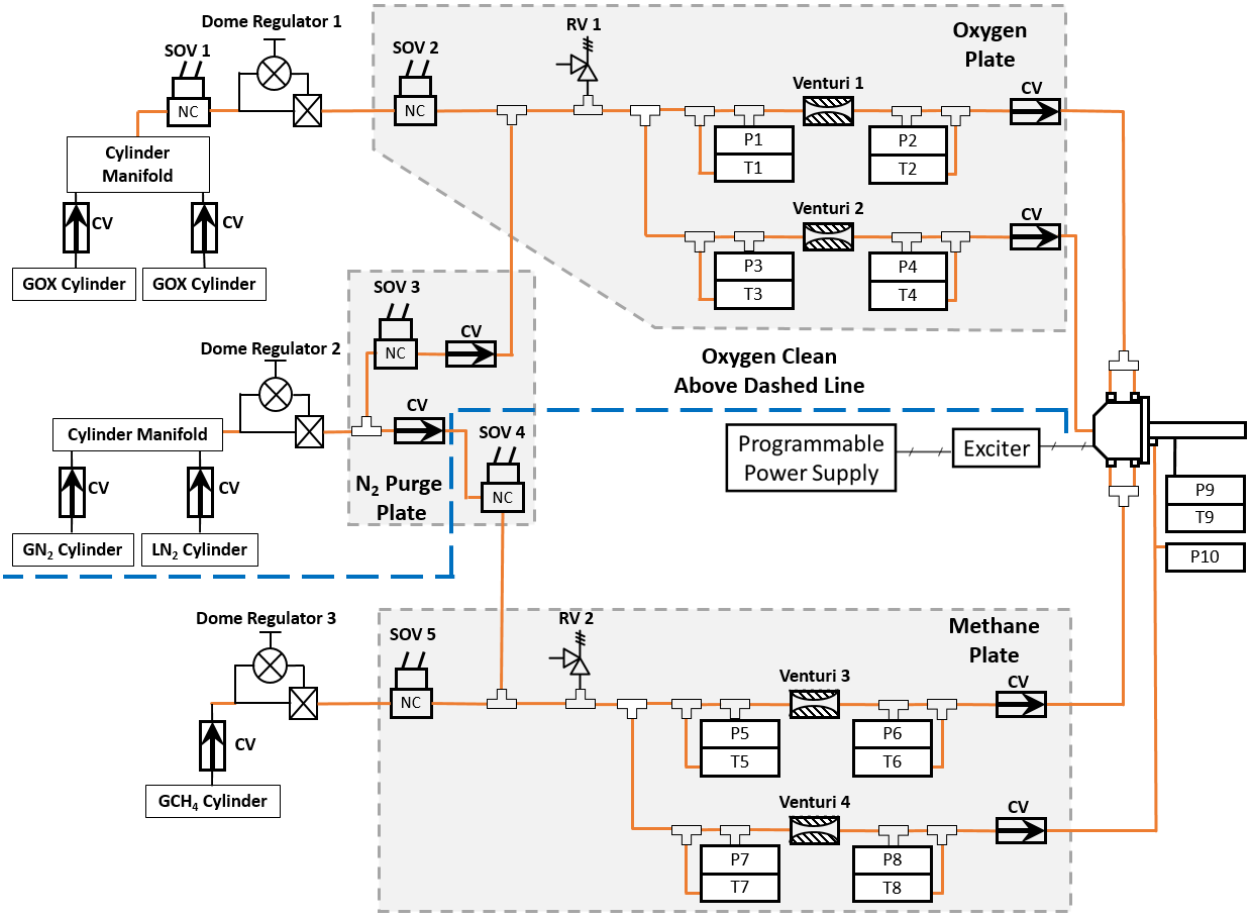


Figure 42 – Component test stand tubing schematic and instrumentation locations

The oxidizer was oxygen (99.98% purity) and the fuel was methane (99.97% purity). Once the system was pressurized, propellant flow was controlled by solenoid valves triggered by the NI-cRIO. The flow was split immediately downstream of the solenoid valves resulting in four gaseous propellant feedlines - two for fuel to the injectors and the coolant co-flow; two for oxidizer to the injectors and the spark gap annulus.

A rendering of the igniter is shown in Figure 43 to provide clarity on the feedlines, igniter modularity, and instrumentation placement for testing. The thermocouple and pressure transducer taps shown pierce the torch tube to provide data within the chamber.

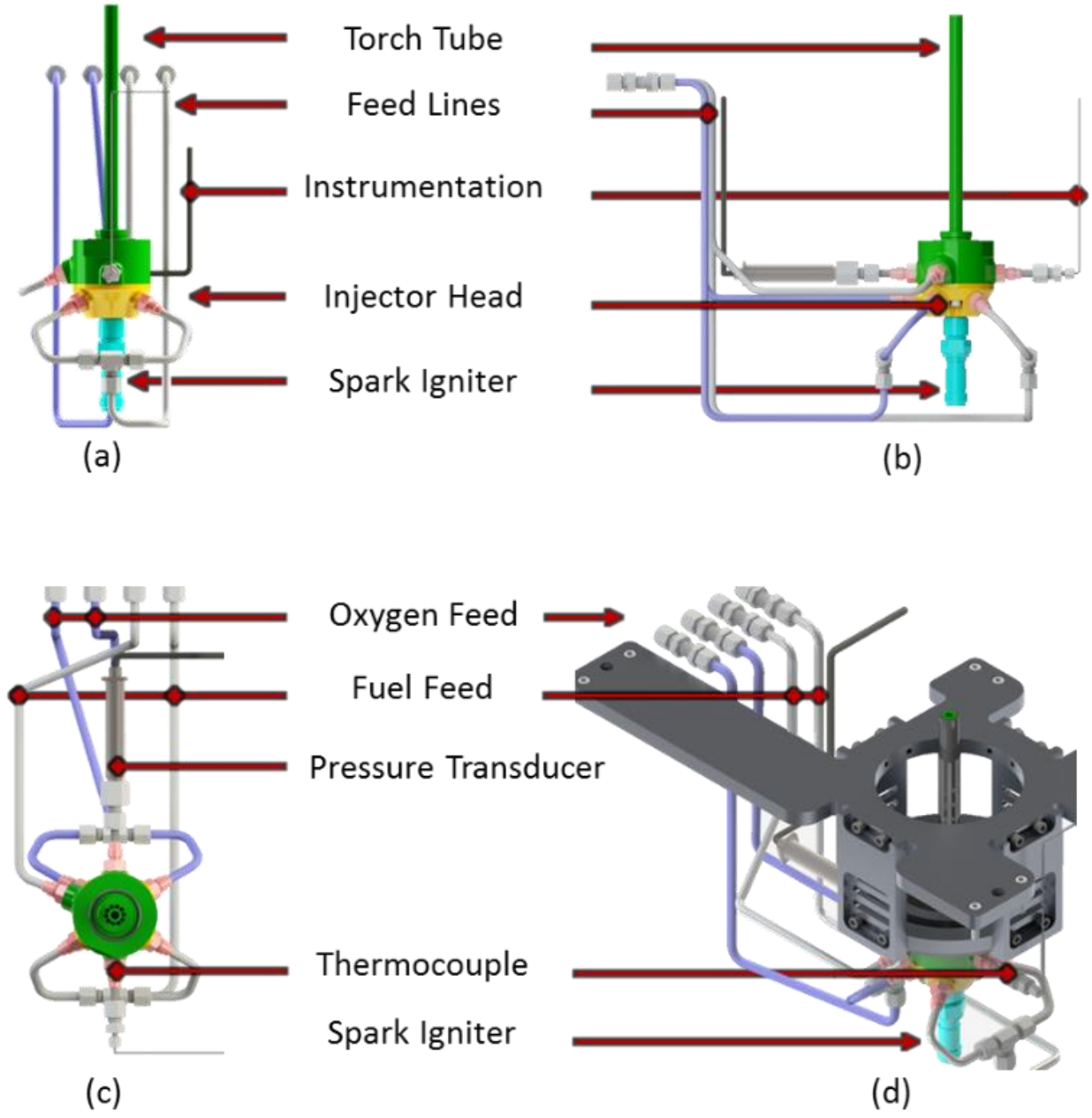


Figure 43 – Modular igniter, relevant instrumentation, tubing, table jig, and hardware

A nickel alloy electrode (center rod) and concentric Inconel 718 cylinder of the igniter injector head formed an annular spark gap. The axial, air-gap spark igniter (Champion Aerospace CH31887-3) was connected to a capacitive Unison exciter (unipolar exciter, 20 kV peak output, 200 Hz pulse rate) to generate sparks. The exciter was powered by 28 VDC and limited to 3 A. A current monitor (20 ns rise time with a 50 Ω termination, thus decreasing sensitivity by a factor of two) and a high voltage probe captured electrical signals that were then recorded by a 12-bit oscilloscope. Spatial uncertainty was ±32.8 V/bit (span of 16 kV), and ±0.156 A/bit (span of 160 A). The resulting Kline-McClintock calculations for spark discharge power, energy, and resistance uncertainty are 16%. Temporal resolution was 1 ns over a 100 μs duration with the triggering event set to +800 V on the high voltage lead. Measurements from various pressure transducers and thermocouples were recorded by a National Instruments compact RIO (NI-cRIO) at 100 Hz, which was connected to the master computer (CPU 1), as shown in Figure 44. The NI-cRIO was used to trigger the DC power supply connected to the spark exciter.

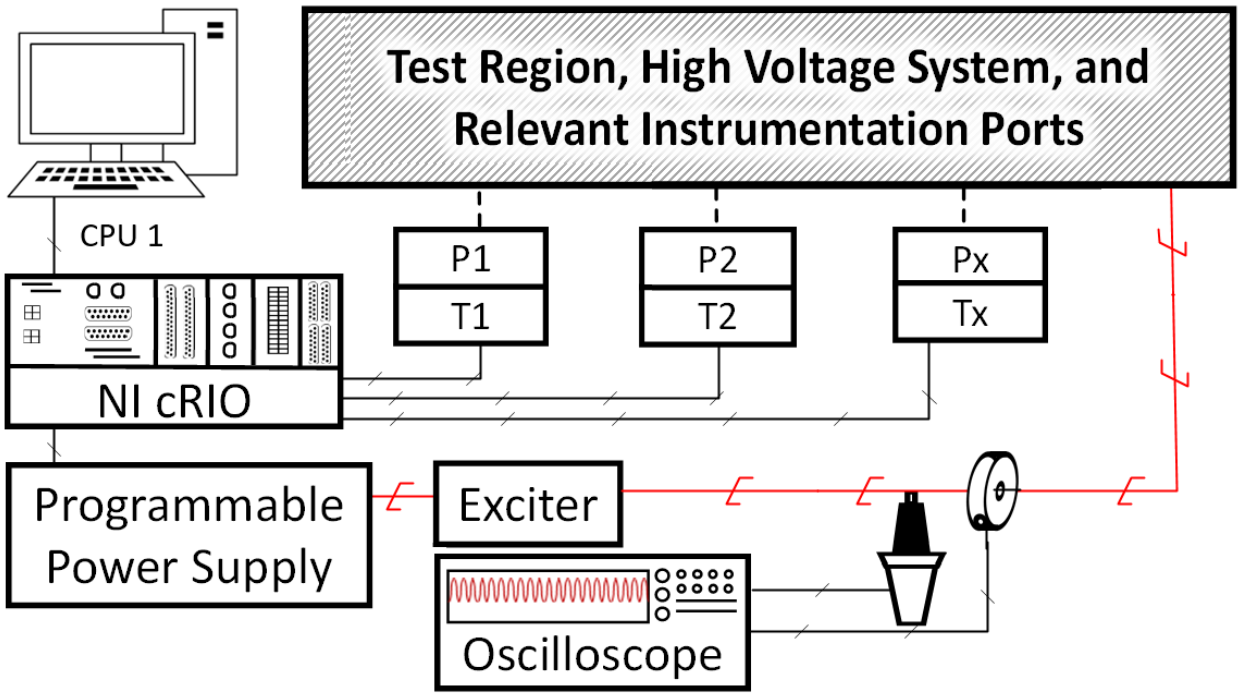


Figure 44 – Reduced data acquisition schematic for the component test stand

Three timing sequences were tested as shown in Figure 45. For all trials, the system was purged with nitrogen before and after testing. Post-test purges continued until the hardware reached ambient conditions

to ensure repeatability of results. The main difference between tests was the leading propellant configuration. The two simplest cases were a fuel lead and an oxygen lead (Figure 45, left and center respectively). The leading propellant valve opened followed by the lagging propellant after a set time interval. The spark exciter was activated with the lagging propellant valve and turned off after two seconds. Select cases continued to run without the spark for an additional second. The sparkless duration of the hot fire was to determine if the flame anchored within the tube or if the train of discrete sparks was the stabilizing factor.

A third timing sequence was explored where the purge gas was expelled from the lagging propellant's tubing to prime the system (Figure 45, right). The lagging propellant burst duration was equivalent to the transit time from the solenoid valve to the torch tube (~90 ms). Once complete, the fuel line was opened. The fuel was allowed sufficient time to reach the chamber, then the oxidizer valve opened while the spark exciter began firing simultaneously. Once more, the spark was cut off after one second to determine flame stability, and the system was subsequently purged and cooled to ambient conditions. Unless otherwise specified, all data presented in this work were collected using a fuel-lead timing configuration. A concise evaluation of timing sequence effects for select mixture ratios and pressures is presented at the end of the results.

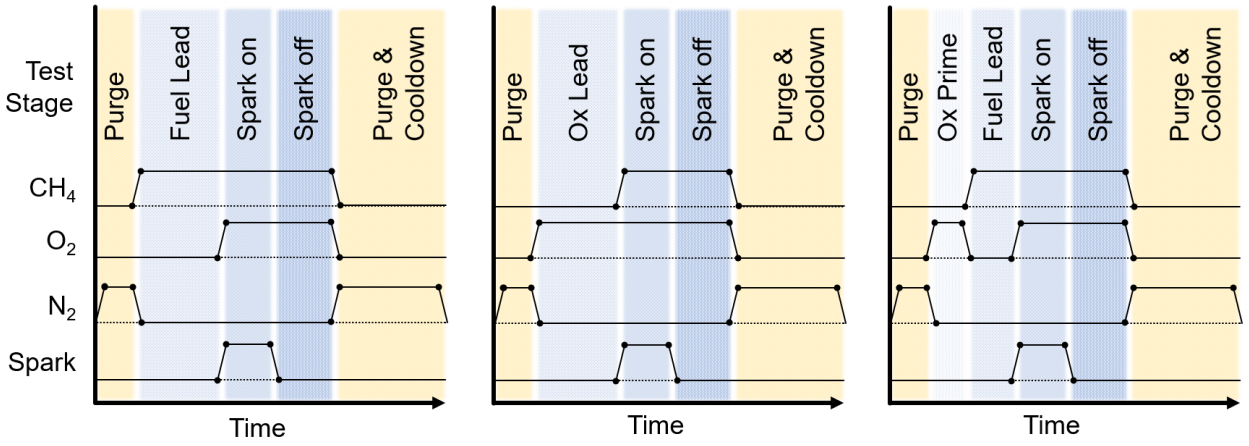


Figure 45 – Timing sequences used for this test campaign: fuel lead (left), oxygen lead (center), oxygen prime and fuel lead (right)

## RESULTS

The time and presence of ignition were marked with a 3 K rise in temperature over 10 ms, which was the minimum temperature difference verified to capture all ignition events. For mean chamber temperatures, the time zero index was the ignition event and is referenced near the melting point of the hardware. The mean temperature traces that are shown in Figure 46 largely represent physical results. Anomalies include select cases for *injector set 2* where the core flow extinguished the flame ($MR_{c,1\text{-}3}$), where instrumentation was damaged ($MR_{c,5}$), where long ignition delays prevented further data collection ($MR_{c,6}$), and where multiple ignition phenomena were averaged together ($MR_{c,3}$ and $MR_{c,7}$).

Two ignition phenomena were observed. The first was ignition of a fuel-lean kernel within a fuel-lean core mixture. This resulted in a steady temperature rise over time and was most likely to occur for low pressures or after a significant ignition delay. The second phenomenon was ignition of a fuel-rich kernel within a fuel-lean core mixture. A fuel-rich mixture near the spark gap is only present within the first scores of milliseconds of startup for timing sequences with a fuel-lead and was readily ignitable with the excited oxidizer leaving the spark gap. The transition from a fuel-rich kernel through stoichiometric to fuel-lean conditions created a sharp and sudden increase in pressure and temperature. The transient and fuel-rich flame burned hotter than steady-flow conditions, almost instantaneously heating both the hardware and the instrumentation. Regardless of which ignition phenomena occurred, the temperature asymptotically approached an equilibrium flame temperature between adiabatic conditions and heat losses. The adiabatic flame temperature over the core mixture ratio range tested is shown in Figure 47. The target core mixture ratios are divided into seven target groups ($MR_{c,1}$ - $MR_{c,7}$) that span subsections of this test range approximately 0.1 $MR/MR_{ref}$ in width. The steady-flow temperature did not reach equilibrium for the results shown and was observed for select cases after upwards of 20-30 seconds. The margin of error of temperature to a 95% confidence interval (CI) is also shown in Figure 46 for successful ignition cases. Adiabatic temperature uncertainties were calculated based on the standard deviation of the core mixture ratio for each case. Blank uncertainty columns (ex. subfigure 6, Case 3, $MR_{c,4}$) indicate that no successful ignitions occurred.

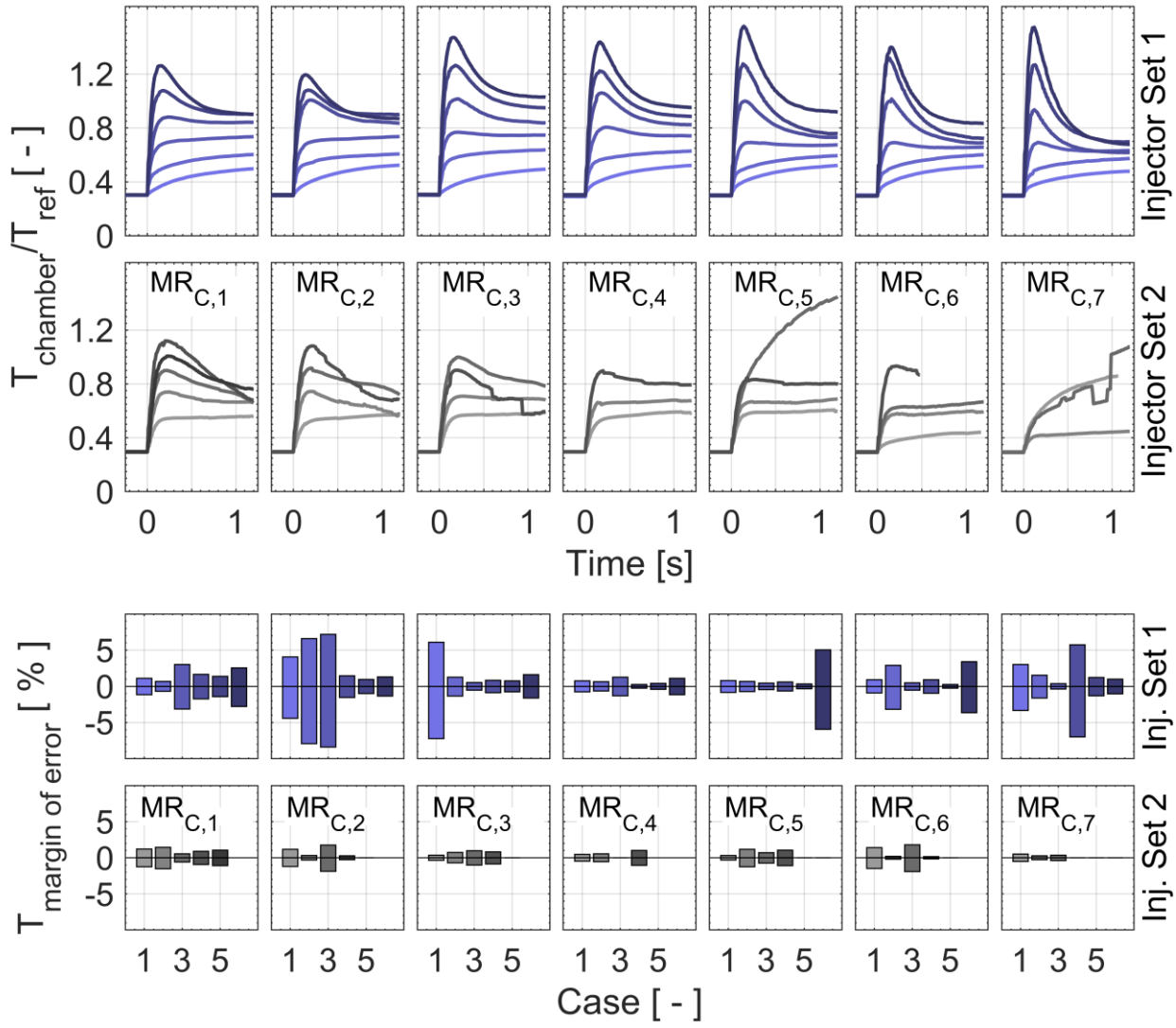


Figure 46 – Mean values of chamber temperature ratios vs. time for successful ignitions and associated uncertainty values where time zero is the ignition event

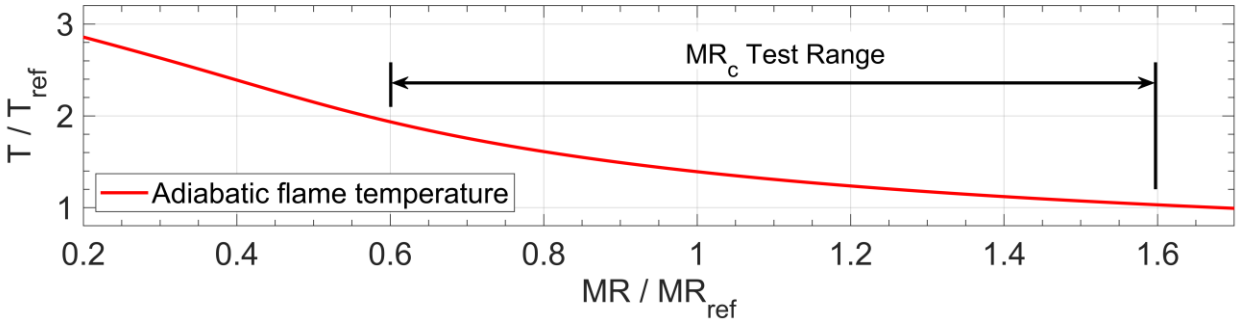


Figure 47 – Adiabatic flame temperatures versus normalized mixture ratio

Figure 48 compares ignition probability between *injector sets 1* and *2*. The same nominal core mixture ratio targets were used. When a complete dataset failed to ignite, no further measurements were recorded for higher feed pressures for the spark annulus ($P_s$ or $P_4$), resulting in a smaller range and quantity of datasets for *injector set 2* $\left(\frac{MR_i}{MR_{ref}} > 0.15\right)$.

The contrast between probability of each hardware set is evident where the injector mixture ratio is used (Figure 48a-c). Due to the normalization with a reference mixture, the phrases "fuel-lean" and "fuel-rich" are relative to other data points shown and are not to be used as an indication of the actual mixture ratio at any point within this manuscript. Fuel-rich injector mixtures have a consistently higher ignition probability and are more likely to ignite at higher pressures than fuel-lean mixtures as shown in Figure 48a. When examining pressure-independent results, the ignition probability is highest for fuel-rich injector mixture ratios with variability toward fuel-lean conditions as seen in Figure 48b-c.

Similarities between ignition probability are better illustrated when plotted solely against the core mixture ratio (Figure 48d-f). When examining ignition probability versus the core mixture ratio, fuel-lean cases at lower pressures have the highest likelihood to ignite with decreasing probability toward high pressure, fuel-lean conditions in Figure 48d. Pressure independent results (Figure 48e-f) show a clear decrease in ignition probability moving from fuel-rich to fuel-lean conditions.

For *injector set 1*, ignition probability was consistently lower beyond a reference pressure ratio of seven whereas *injector set 2* showed a sharp drop to zero probability near the same conditions as shown in Figure 49. A minimum of thirty tests were performed to create each data point and calculate the 95% confidence intervals. On average, the uncertainty band for ignition probability was ±14%.

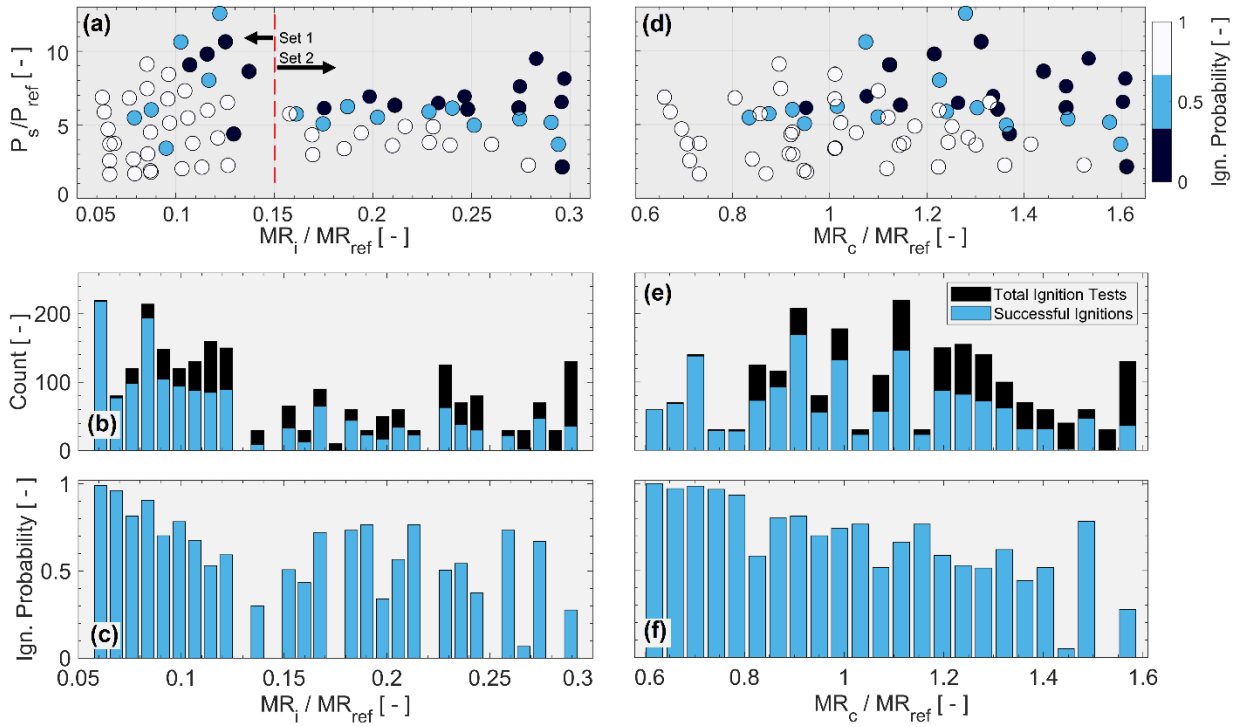


Figure 48 – Effects of mixture ratio (injector and core) and pressure versus ignition probability. The ignition probability legend applies to subfigures (a) and (d). The total vs. successful ignition legend applies to subfigures (b) and (e).

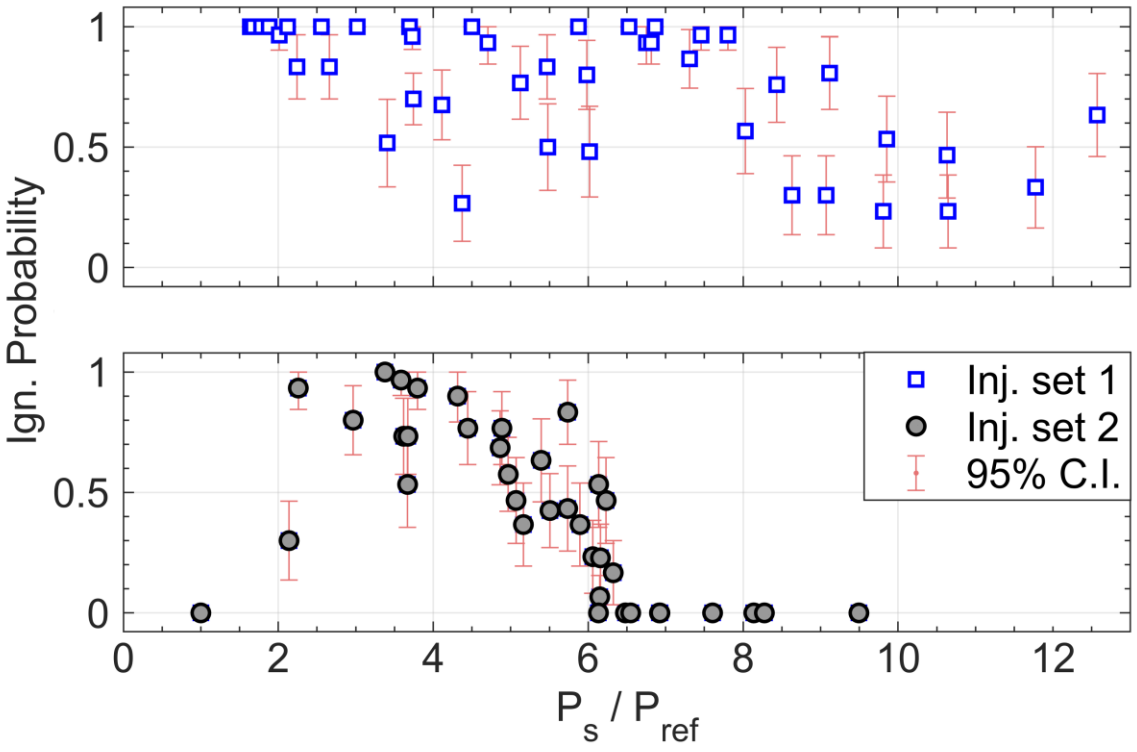


Figure 49 – Ignition probability versus spark chamber feed pressure

Mean chamber pressure traces are provided for successful ignition tests in Figure 50 to show the relative ignition delays. Data is divided into seven nominal core mixture ratio groups that are tested at select pressures. Time zero is set when the first spark is fired, which coincides with the opening of the lagging propellant (oxidizer) valve.

The mean pressures shown in the top half of Figure 50 are for the fuel-rich injector set and had the shortest ignition delay (but not necessarily high ignition probability) for higher chamber pressures (therefore higher feed pressures and mass flow rates) where ignition is said to occur when temperature begins to rise. The same data is shown in Figure 51 versus the feed pressure of the spark annulus. Ignition for almost all these cases occurred with cold flow (non-reacting) pressures near the reference pressure and had ignition delays between 0.06 and 1.0 seconds as shown in Figure 50. The mean pressures for the fuel-lean injector set (*injector set 2*) show longer ignition delays and significant variance within core mixture ratio groups. Cold flow ignition pressure ratios range from 1-3 and ignition delays from 0.5 - 1.8 seconds.

Irregular pressure rises (i.e., not smooth), as observed for *injector set 2* of Figure 50, are nonphysical. These variances are caused by the reference time for averaging data being the ignition event. Data to the left of the ignition point may not correlate to the same conditions. Pressure traces for results with high ignition delay may be either the transient rise or steady cold flow chamber pressure whereas the pressure data with low ignition delay may only be the transient rise.

The core mixture ratio showed similar trends with the ignition delay as seen in Figure 51. Fuel-rich mixtures at higher pressures had the shortest ignition delay. Ignition delay increases for fuel-lean mixtures with lower pressure ratios (< 5). However, the core mixture ratio is a poor indicator of ignition delay. Differences between ignition delay zones for each hardware set are clearly seen when injector mixture ratio is considered instead in Figure 51.

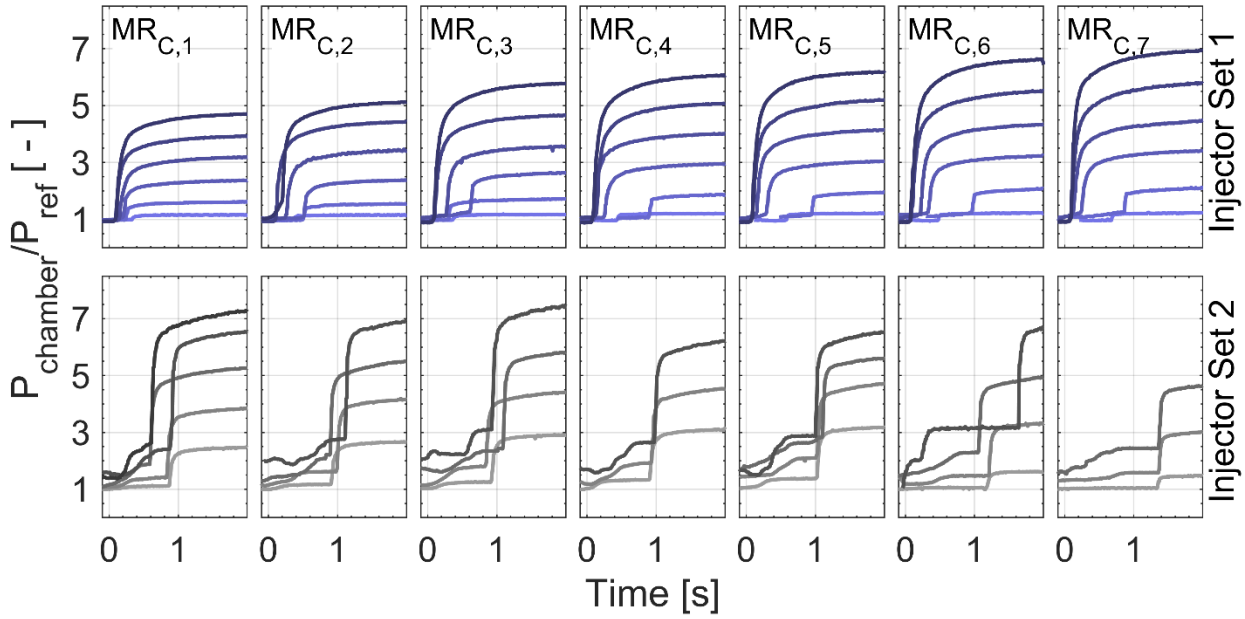


Figure 50 – Mean values of nondimensionalized chamber pressure vs. time for successful ignitions where time zero is the first spark

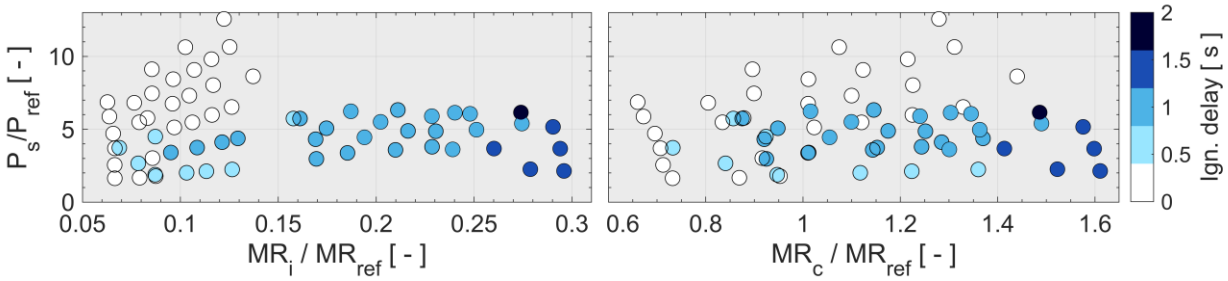


Figure 51 – Effects of mixture ratio (injector and core) and pressure versus ignition delay

The effects of valve timing (propellant delays) were investigated for select cases as described in methodology with Figure 45, and the results are tabulated below in Table 7. The comparisons are listed in the table in order of ascending mass flow rate (feed pressure). Since the ignition delays have been shown dependent on both pressure and the mixture ratio, they are then grouped by the core and injector mixture ratios. Results with oxidizer leads typically showed the lower ignition probability and longest ignition delays. A fuel lead improved ignition probability and reduced ignition delay under most conditions. The highest ignition probability and shortest ignition delays were observed for the oxidizer prime, fuel lead sequence.

Table 7 – Timing sequence effects on ignition delay and ignition probability (CI=confidence interval)

| Lead | Prime | Tests | $\frac{P}{P_{ref}}$ | $\frac{MR_c}{MR_{ref}}$ | $\frac{MR_i}{MR_{ref}}$ | Delay [s] | Ignition Probability ± 95% CI |
|---|---|---|---|---|---|---|---|
| Ox | - | 60 | 0.6 | 0.7 | 0.07 | 1.21 | 1.00 ± 0.00 |
| Fuel | - | 30 | 0.6 | 0.7 | 0.07 | 0.35 | 1.00 ± 0.00 |
| Fuel | - | 30 | 1.1 | 1.6 | 0.30 | 1.37 | 0.30 ± 0.16 |
| Fuel | Ox | 30 | 1.4 | 1.6 | 0.29 | 0.20 | 1.00 ± 0.00 |
| Ox | - | 30 | 1.5 | 0.7 | 0.07 | 0.87 | 0.97 ± 0.03 |
| Fuel | - | 30 | 1.6 | 0.7 | 0.07 | 0.26 | 1.00 ± 0.00 |
| Ox | - | 30 | 2.6 | 1.1 | 0.11 | 1.21 | 0.80 ± 0.14 |
| Fuel | - | 70 | 2.7 | 1.2 | 0.11 | 0.97 | 0.70 ± 0.11 |
| Ox | - | 30 | 2.8 | 0.7 | 0.07 | 0.68 | 1.00 ± 0.00 |
| Fuel | - | 30 | 2.7 | 0.7 | 0.07 | 0.23 | 1.00 ± 0.00 |
| Ox | - | 30 | 3.8 | 0.8 | 0.08 | 1.09 | 0.57 ± 0.18 |
| Fuel | - | 30 | 3.7 | 0.7 | 0.07 | 0.18 | 0.93 ± 0.07 |
| Fuel | - | 40 | 4.0 | 1.4 | 0.25 | 1.05 | 0.58 ± 0.15 |
| Fuel | Ox | 30 | 3.3 | 1.6 | 0.30 | 0.10 | 1.00 ± 0.00 |
| Fuel | - | 30 | 5.1 | 1.3 | 0.25 | 1.02 | 0.23 ± 0.15 |
| Fuel | Ox | 30 | 5.3 | 1.6 | 0.29 | 0.13 | 1.00 ± 0.00 |
| Ox | - | 63 | 5.5 | 0.7 | 0.07 | 0.79 | 0.79 ± 0.14 |
| Fuel | - | 60 | 5.9 | 0.7 | 0.06 | 0.12 | 1.00 ± 0.00 |
| Ox | - | 30 | 7.7 | 1.1 | 0.10 | 1.75 | 0.03 ± 0.06 |
| Fuel | Ox | 35 | 7.6 | 0.9 | 0.16 | 0.11 | 0.86 ± 0.12 |
| Fuel | - | 30 | 8.1 | 1.1 | 0.11 | 0.11 | 0.30 ± 0.16 |
| Fuel | Ox | 62 | 8.0 | 1.1 | 0.10 | 0.07 | 1.00 ± 0.00 |

## DISCUSSION

While not all-encompassing of the phenomena that affect mixing of the reactants, correlations for ASI igniters were developed to accelerate the design process by relating input variables to ignition probability – $MR_c$, $MR_i$, $\eta$, $\psi$. The injector geometry has nontrivial effects on the location, size, and composition of the reactant mixture based on computational efforts, but ignition probability itself requires validation from experimental tests.

Ignition probability was observed to increase for fuel-rich mixtures (both $MR_c$ and $MR_i$), at lower pressures, and with a valve sequence where the lagging propellant line was primed immediately before test. Figures 48a and 48d shows approximate probability values for each test condition. The lower two-thirds of Figure 48, subfigures b, c, e, and f, shows the total number of tests, the number of successful ignitions, and

the associated ignition probability for a given mixture ratio. Ignition probability has a clear downward trend as $MR_c$ increases, while $MR_i$ demands further examination. The trend for the first injector set $\left(\frac{MR_i}{MR_{ref}} < 0.15\right)$ shows decreasing probability moving toward fuel-lean conditions. Results for the second injector set $\left(\frac{MR_i}{MR_{ref}} > 0.15\right)$ have greater variability and appear to have higher probability values at first glance. However, no tests were recorded for higher pressure levels for *injector set 2* as tests surpassing pressure ratios of 6.5 failed to ignite. If more tests were recorded above pressure ratios of 6.5, the trend observed for *injector set 1* (decreasing probability toward fuel-lean conditions) would likely continue for results from *injector set 2*. This conjecture is supported by ignition probability results versus pressure for each injector set shown in Figure 49.

The momentum factors, as described by Equation 16 and 17, were expected to affect ignition probability, but to an unknown degree. The *fuel-to-oxidizer* radial and axial momentum ratio ($\psi$ and $\eta$ respectively) are shown in Figure 52. When using the area of the spark annulus to determine the oxidizer momentum, the axial momentum ratio ranged between 6 - 18. Ignition probability plateaued for $\eta$ values between 10 - 14 for both injector sets. No clear optimal zone was observed for radial momentum ratios, though the ignition likelihood appeared to increase toward $\psi$ values approaching one.

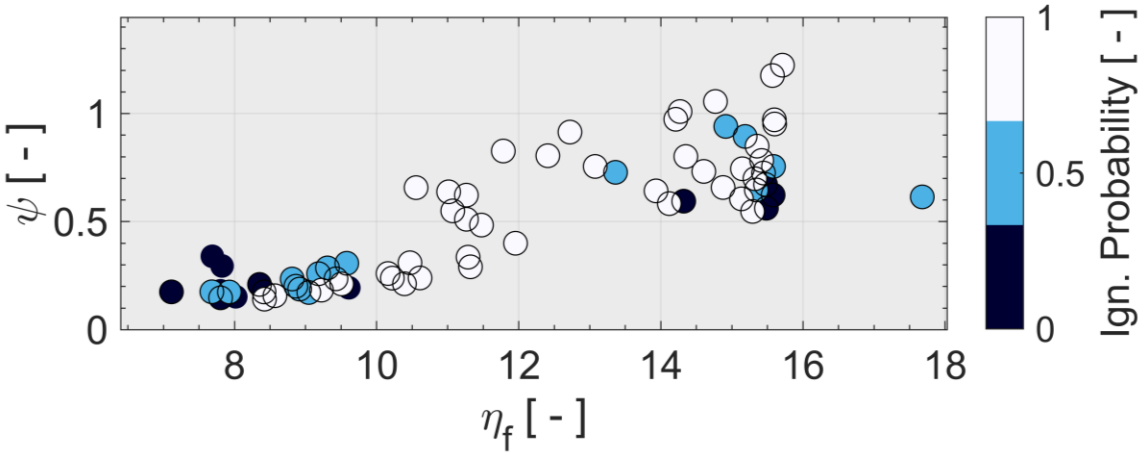


Figure 52 – Ignition probability versus the axial momentum ratio ($\eta$) and the radial momentum ratio ($\psi$)

By comparing the ignition probability of each injector set against a single momentum ratio (Figure 53), unique results become more apparent. For the fuel-rich injectors (set 1), ignition probability increased for lower values of the axial momentum ratio ($\eta$). For stratified flows, ignition is highly dependent on a flammable mixture being present near the spark igniter [45]. Here, the spark annulus flow comprises most of the mass flow and is therefore traveling at high velocity. The high velocity creates a low-pressure zone, encouraging backflow of fuel from the doublets. Should the jet be traveling at too low of a speed, recirculation may be nonexistent, preventing the spark from reaching the flammable mixture. A high speed, conversely, strains the flame kernel to the point of quenching.

Not only does the spark annulus flow rate influence reactant mixing, it also affects spark energy. As the total flow rate changes, the energy deposition changes with respect to temperature [87, 44, 88], duration, flow penetration and shape [47] [44]. Returning to Figure 53, a clear optimal zone exists between values of 10-14 for $\eta$. For radial momentum ratios ($\psi$) ignition probability tends to rise approaching one. In contrast, the ignition probability was independent of the $\psi$ range tested for the fuel-lean injectors (set 2) and increased for higher values of $\eta$ (nearing 10) as seen on the left of Figure 53.

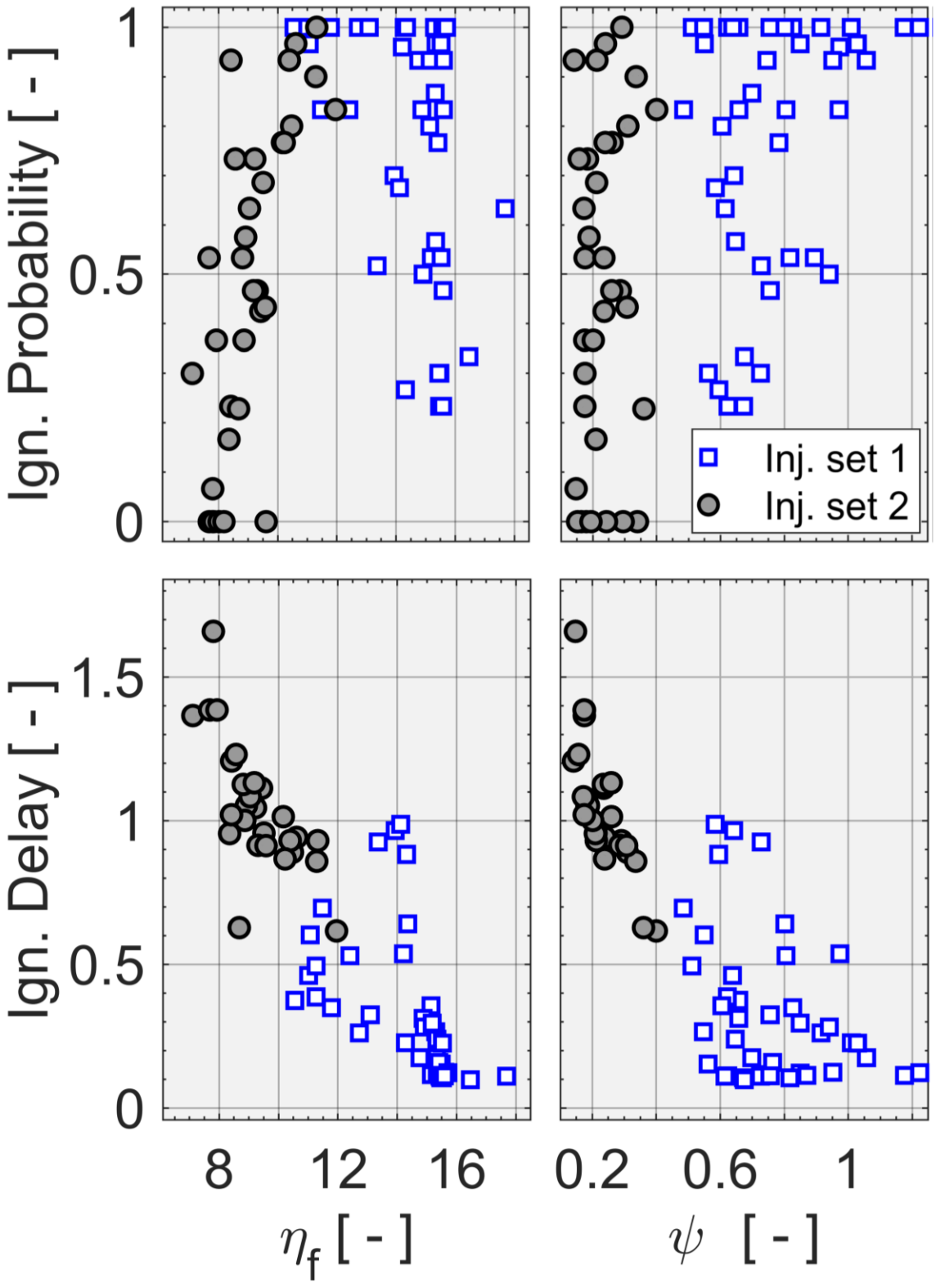


Figure 53 – Ignition probability and ignition delay versus the axial momentum ratio ($\eta$) and the radial momentum ratio ($\psi$)

The substantially shorter ignition delays for the fuel-rich *injector set 1* as shown in the lower half of Figure 53 are attributed to the increased likelihood of a flammable mixture reaching the spark plume. For the fuel-rich injectors, ignition delay was shorter for higher pressure tests with fuel-rich conditions as observed in both Figure 50 and 51. Similar results were shown for *injector set 2* (shorter delays for fuel-rich conditions). For the fuel-lean *injector set 2*, which was less likely to have an ignitable mixture present during the transient pressure rise, ignition probability was reduced and variability increased with higher pressures. Variability in ignition delay was in part attributed to quenching of the spark. At high-pressure conditions, the spark event is quenched within a few hundred milliseconds of the trainset pressure rise. If no flammable mixture is near the spark gap in this window, the ignition attempt fails. Thus, it is possible to have low ignition delays with low ignition probability (c.f. Figure 48 and 51). Ideal settings have low ignition delays and high ignition probability. These results were consistently observed when a priming valve sequence was used and under no other conditions.

## CONCLUSIONS

Ignition probability and delays are investigated for an augmented spark impinging igniter as a function of axial and radial momentum ratios, effects of pre-chamber pressure, propellant injection timing, igniter geometry, and both core and injector (local) mixture ratios. The results provide insight into the optimal values for these parameters.

Ignition probability was highest for radial momentum factors approaching one (theoretically resulting in purely axial flow of resultant streams) and for axial momentum ratios between 10-14. Ignition delays decreased with increasing radial momentum ratios and increasing axial momentum ratios. Short ignition delays were repeatably and reliably caused by a fuel-rich kernel of gas igniting prior to reaching the steady chamber pressure for cold flow. Ignition probability dropped substantially after a reference pressure ratio of six because of spark quenching. If an ignitable mixture of gas did not reach the spark discharge during the transient pressure rise before this point, there was effectively no chance of ignition occurring. *Injector*

*set 1* (fuel-rich in relative terms) maintained higher probabilities beyond this pressure level because it was more likely to create a fuel-rich kernel near the spark gap during the transient pressure rise. The same phenomenon is responsible for shorter ignition delays, which often correlate to higher feed pressures. As a result, it is possible to have low ignition delays with low ignition probability.

Two ignition mechanisms were observed – ignition of a fuel-rich mixture and ignition of a fuel-lean mixture. The first led to sharp increases in temperature above the equilibrium flame temperature of the core mixture ratio. The second led to a steady rise in temperature. Both ignition events resulted in similar pressure rises and asymptotically approached an equilibrium flame temperature between adiabatic flame conditions and heat losses to hardware.

The most repeatable and reliable ignition probability occurred for a timing sequence that primed the oxidizer lines and then used fuel as the leading propellant. This was for both the fuel-lean and fuel-rich injector sets. Ignition delays were no greater than a few tens of milliseconds in comparison to delays that ranged from 100 - 2000 ms for fuel-lead and oxidizer-lead timing sequences. Fuel-lead sequences had higher probability and shorter delays than oxidizer-lead sequences for fuel-lean core mixture ratios. The inverse is anticipated for fuel-rich core mixture ratios.

# CHAPTER 6:
# DISSERTATION CONCLUSIONS

Augmented spark impinging igniters are easily overlooked combustion devices that must function without flaw, yet rely on the stochastic success of a multiphysics process to start a chemical reaction in a hostile environment. This hostile setting contains elevated pressures that may quench spark discharges before a flammable mixture is present, potential shockwaves and fluid expansion that self-extinguish the flame kernel formed by a spark discharge that too quickly deposited energy, and crossflows that can strain and quench flames that have not yet anchored or stabilized. Failure mechanisms are plentiful, and the only risk mitigation is characterization and understanding of each step of the ignition process.

This dissertation has discussed the practical nuances of spark discharge ignition that have not been the focus of other studies – quenching, electromagnetic interference, and false signals. Dissemination of these results prevents others from repeating mistakes during experimental testing or data recording, and provides a basis to determine if their results are physically impacting their media or are simply artifacts of their data collection method. The finding that discharge properties for annular-electrode spark gaps are tied to the pressure-distance quotient instead of the traditional pressure-distance product changes analysis methods for future efforts. Coalescence of electrical and fluid dynamic properties (e.g., channel resistance, spark duration, and plume velocity) to the pressure-distance quotient sets groundwork for nondimensional analysis that may better characterize annular-electrode spark gap discharges.

Simulations in this work provide a foundation for a simple, bulk-flow analysis that results in objective design functions. The combination of fluid dynamic variables (mass flow, density, etc.) and igniter geometry (injector ratios and diameters) may now be used to predict local mixture ratios with great accuracy. Fluid dynamic structures are shown across sub, trans, and supersonic regimes that affect mixing and flow recirculation, and may act as a stabilizing anchor for the flame. Dissemination of these results will lead to an accelerated design process, saving time, schedule, and material. The broad and parametric results of this work eliminate waste of future computational campaigns by providing a nondimensional basis for cold-flow fluid dynamics, flammable fluid volumes, mixing lengths, and mixing efficiency.

The full-scale testing demonstrates that ignition probability is tied to variables (local and core mixture ratios, radial and axial momentum ratios) of design functions derived from computational results. Results provide insight into torch igniter function across a broad range of mixture ratios near and beyond fuel-lean flammability limits. The transient pressure rise may be rapid, as observed in this work, and prevent spark ignition from occurring after the first scores of milliseconds (due to spark quenching as shown in the first section of this body of work). Consequently, the timing sequence is critical with regards to ignition probability, and this work demonstrates the need to understand the subjective differences that facility and test rig design may impose on hardware. These results show the importance of prior sections as they are unmistakably dependent on spark discharges and the design variables that develop an ignitable mixture.

While meticulous and systematic as schedule, finance, and manpower allow, these results are by no means the end of augmented spark igniter research. This body of work establishes footing for, and will help mitigate risk for future efforts.

# CHAPTER 7:
# FUTURE WORK

## ANNULAR GAP SPARK DISCHARGES

This dissertation presents answers for many questions associated with augmented spark impinging igniters for liquid rocket engines, yet many questions remain, and further phenomena should be examined. Annular-gap spark igniters with flowing media should continue to be studied. There is still a need to optimize the means to deliver the activation energy. A similar experimental setup can be used to examine the dissociation and excitation of chemical species, measure gas temperature, and show the unique benefits of exciting either the fuel or oxidizer. The relation between the pressure-distant quotient and discharge properties should be examined in more detail for different styles of spark exciters (inductive), which have longer discharge periods than their capacitive counterparts. Spark quenching, effects of electromagnetic interference, and hardware erosion should be studied to characterize failure mechanisms for designers of ignition hardware.

## COMPUTATIONAL FLUID DYNAMICS SIMULATIONS

Simulations for augmented spark impinging igniters are by no means trivial and demand further work. Future simulations of these igniters should vary the chamber diameter while keeping geometric ratios proportional to the simulations in this work. Doing so will dispel the concern that transport effects are appropriately captured, and further verify the analytic relations derived. Reacting flow should be simulated to determine where the flame anchors during steady-flow conditions. Present understanding is limited to hypotheses based on the current models and previous efforts on injector studies, which may not have refinement in the region of interest for ignition.

In addition, all the simulations in this work focused on the internal flow and mixing of a spark igniter. Simulations of the external flow, coupled with experimental testing, may provide understanding of flame standoffs, quantify off-axis turbulent diffusion, and the influence of supersonic structures in flame stability.

## EXPERIMENTAL TESTING

### INTERNAL FLOW

Future experimental studies should aim to validate or disprove the objective design functions as a quick analytic tool to predict ignition probability and accelerate the design process. Varied hardware configurations (injector diameter ratios, torch tube lengths, torch tube diameters, or injector patterns) should expand the ignition probability map for local mixture ratios, core mixture ratios, radial and axial momentum factors, and operating pressures. The overall goal is to find the bounds of high ignition probability while creating a sustainable core flame that does not cause damaging, localized heat loads.

### EXTERNAL FLOW

The experimental ignition tests here are restricted to internal flow of the igniter and do not consider the external flame that would be used to ignite a gas generator or main combustion chamber. There is a need to study highly turbulent inverse diffusion flames (oxidizer as the central flow, fuel as the co-flow) to determine mixing lengths, flame dispersion (axial and radial), and stabilizing phenomena. Practically, a torch igniter may be in a confined space (i.e., gas generator) and a long flame may damage hardware on the opposing wall. Therefore, the flame length can be a critical element. Flame robustness is equally important, and blowoff limits due to crossflow and coaxial strains should be studied as there is no use for a torch igniter that can light itself but no other device.

## REFERENCES


[1] J. R. Santiago, "Evolution of Pratt & Whitney's Cryogenic Rocket Engine RL-10," in *AIAA, ASME, SAE, and ASEE, 32nd Joint Propulsion Conference and Exhibit*, Lake Buena Vista, 1996, AIAA-96-3013.

[2] L. H. Nave and G. A. Coffey, "Sea-Level Side-Loads in High Area Ratio Rocket Engines," in *9th Propulsion Conference*, Las Vegas, (05-07 November 1973), AIAA-73-1284, https://doi.org/10.2514/6.1973-1284.

[3] G. Hagemann, C. A. Schley, E. Odintsov and A. Sobatchkine, "Nozzle Flowfield Analysis with Particular Regard to 3D-Plug-Cluster Configurations," in *32nd Joint Propulsion Conference and Exhibit*, Lake Buena Vista, 1996, AIAA-96-2954, https://doi.org/10.2514/6.1996-2954.

[4] Rocketdyne Propulsion and Power, "Space Transportation System Training Data: Space Shuttle Main Engine Orientation," June 1998. [Online]. Available: http://www.lpre.de/p_and_w/SSME/SSME_PRESENTATION.pdf. [Accessed 01 03 2020].

[5] H. F. Coward and G. W. Jones, "Limits of Flammability of Gases and Vapors," United States Bureau of Mines, Bulletin 503, Washington D.C., 1952.

[6] T. Brown, M. Klem and P. McRight, "Foundational Methane Propulsion Related Technology Efforts, and Challenges for Applications to Human Exploration Beyond Earth Orbit," in *Space Propulsion, Paper ID: SP2016_AP4*, Rome,, (2-6 May 2016).

[7] NASA, "NASA and Virgin Orbit 3D Print, Test Rocket Combustion Chamber," NASA, 16 May 2019. [Online]. Available: https://www.nasa.gov/centers/marshall/news/news/releases/2019/nasa-and-virgin-orbit-3d-print-test-rocket-combustion-chamber.html. [Accessed 03 2020].

[8] NASA, "NASA Marshall Advances 3-D Printed Rocket Engine Nozzle Technology," NASA, 19 03 2018. [Online]. Available: https://www.nasa.gov/centers/marshall/news/releases/2018/nasa-marshall-advances-3-d-printed-rocket-engine-nozzle-technology.html. [Accessed 03 2020].

[9] T. McMahan, "Successful NASA Rocket Fuel Pump Tests Pave Way for 3-D Printed Demonstrator Engine," NASA, 26 08 2015. [Online]. Available: https://www.nasa.gov/centers/marshall/news/news/releases/2015/successful-nasa-rocket-fuel-pump-tests-pave-way-for-3-d-printed-demonstrator-engine.html. [Accessed 01 03 2020].

[10] J. Buck and T. McMahan, "Sparks Fly as NASA Pushes the Limits of 3-D Printing Technology," NASA, 28 August 2014, Release 14-233. [Online]. Available: https://www.nasa.gov/press/2014/august/sparks-fly-as-nasa-pushes-the-limits-of-3-d-printing-technology/.

[11] A. Lanz, J. Heffel and C. Messer, "Hydrogen Fuel Cell Engines and Related Technologies: Rev 0," College of the Desert, Energy Technology Training Center, Palm Desert, 2001.

[12] H. P. Trinh, "Liquid Methane/Liquid Oxygen Injectors for Potential Future Mars Ascent Engines," in *American Inst. of Aeronautics and Astronautics Joint Propulsion Conference*, Huntsville, 1999, https://doi.org/10.2514/6.2000-3119.

[13] T. Neill, D. Judd, E. Veith and D. Rousar, "Practical uses of Liquid Methane in Rocket Engine Applications," *Acta Astronautica*, vol. 65, no. 5-6, pp. 696-705, 2009, https://doi.org/10.1016/j.actaastro.2009.01.052.

[14] G. Landis, S. Oleson, T. Packard, D. Linne, J. Woytach, M. Martini, J. Fittje, J. Gyekenyesi, A. Colozza, J. Fincannon, K. Bury, H. Domniguez, R. Jones, D. Smith, S. Miller and D. Vento, "Design Study of a Mars Ascent Vehicle for Sample Return using In-Situ Generated Propellant," in *AIAA Scitech Forum, 10th Symposium on Space Resource Utilization*, Grapevine, TX, 2017, AIAA 2017-0424, https://doi.org/10.2514/6.2017-0424.

[15] D. K. Huzel and D. H. Huang, Modern Engineering for Design of Liquid-Propellant Rocket Engines, Washington DC: Progress in Astronautics and Aeronautics, Vol. 147, 1992, https://doi.org/10.2514/4.866197.

[16] T. J. Rudman and K. L. Austad, "The Centaur Upper Stage Vehicle," in *4th International Conference on Launcher Technology "Space Launcher Liquid Propulsion"*, Liege, (Belgium), 3-6 December 2002.

[17] W. M. Marshall, R. J. Osborne and S. E. Greene, "Development of Augmented Spark Impinging Igniter System for Methane Engines," in *AIAA Propulsion and Energy Forum, AIAA 2017-4665*, Atlanta, (10-12 July 2017), https://doi.org/10.2514/6.2017-4665.

[18] E. A. Hurlbert, R. J. Moreland and S. Candel, "Propellant Ignition and Flame Propagation," in *Liquid Rocket Thrust Chambers: Aspects of Modeling, Analysis, and Design*, edited by M. Popp, J. Hulka, V. Yang and M. Habiballah, Vol 200, Progress in Astronautics and Aeronautics, AIAA, Reston, 2004, pp. 405-436.

[19] J. Kleinhenz, C. Sarmiento and W. Marshall, "Spark ignition characteristics of a $LO_2/LCH_4$ engine at altitude conditions," in *48th AIAA/ASME/SAE/ASEE Joint Propulsion Conference*, Atlanta, 2012, AIAA 2012-4129, https://doi.org/10.2514/6.2012-4129.

[20] C. Soares, "Gas Turbines: A Handbook of Air, Land, and Sea Applications, 2nd Edition," Oxford, U.K., Butterworth-Heinemann, 2014, pp. 423-426.

[21] E. Breuser, "Spark plugs," in *Gasoline Engine Management*, Wiesbaden, Springer Vieweg, Bosch Professional Automotive Information, 2015, pp. 178-211.

[22] M. S. Naidu and V. Kamaraju, "High Voltage Engineering," in *2nd Edition*, New York, McGraw-Hill 1996, 1996.

[23] N. Nugent, "Breakdown Voltage Determination of Gaseous and Near Cryogenic Fluids with Application to Rocket Engine Ignition," Ph.D. Dissertation, Mechanical Engineering Department. Purdue University, West Lafayette, IN, 2009.

[24] D. R. Ballal and A. H. Lefebvre, "The Influence of Spark Dischage Characteristics on Minimum Ignition Energy in Flowing Gases," *Combustion and Flame*, vol. 24, no. 1, pp. 99-108, 1975, https://doi.org/10.1016/0010-2180(75)90132-7.

[25] Y. Ju and W. Sun, "Plasma Assisted Combustion: Dynamics and Chemistry," *Progress in Energy and Combustion Science*, vol. 48, no. 1, pp. 21-83, 2015, https://doi.org/10.1016/j.pecs.2014.12.002.

[26] Y. Ju and W. Sun, "Plasma Assisted Combustion: Progress, Challenges, and Opportunities," *Combustion and Flame*, vol. 162, no. 3, pp. 529-532, 2015, https://doi.org/10.1016/j.combustflame.2015.01.017.

[27] C. C. Swett, "Investigation of Spark Gaps Subjected to Altitude and Air-Velocity Conditions," NACA Lewis, Cleveland, 1948, NACA RM E8I17.

[28] C. C. Swett, "Spark Ignition of Flowing Gases I - Energies to Ignite Propane-Air Mixtures in Pressure Range of 2 to 4 inches Mercury Absolute," NACA Lewis, Cleveland, 1949, NACA RM-E9E17.

[29] C. C. Swett, "Spark Ignition of Flowing Gases," NACA Lewis, Cleveland, 1956, NACA-TR-1287.

[30] C. C. Swett, "Effect of Gas Stream Parameters on the Energy and Power Dissipated in a Spark and on Ignition," *Symposium on Combustion and Flame, and Explosion Phenomena*, vol. 3, no. 1, pp. 353-361, 1948, https://doi.org/10.1016/S1062-2896(49)80042-0.

[31] C. C. Swett, "Spark Ignition of Flowing Gases using Long-Duration Discharges," *Symposium (International) on Combustion*, vol. 6, no. 1, pp. 523-532, 1957, https://doi.org/10.1016/S0082-0784(57)80069-1.

[32] D. R. Ballal and A. H. Lefebvre, "The Influence of Flow Parameters on Minimum Ignition Energy and Quenching Distance," *Symposium (International) on Combustion*, vol. 15, no. 1, pp. 1473-1481, 1975, https://doi.org/10.1016/S0082-0784(75)80405-X.

[33] D. R. Ballal and A. H. Lefebvre, "Ignition and Flame Quenching in Flowing Gaseous Mixtures," *Proceedings of the Royal Society London*, vol. 357, no. 1689, pp. 163-181, 1977, https://doi.org/10.1098/rspa.1977.0161.

[34] M. Kono, K. Hatori and K. Iinuma, "Investigation on Ignition Ability of Composite Sparks in Flowing Mixtures," *Symposium (International) on Combustion*, vol. 20, no. 1, pp. 133-140, 1985, https://doi.org/10.1016/S0082-0784(85)80496-3.

[35] I. Glassman, "Combustion," New York, 3rd ed, Academic Press, 1996, pp. 325-347.

[36] T. Yuasa, S. Kadota, M. Tsue, M. Kono, H. Nomura and Y. Ujiie, "Effects of Energy Deposition Schedule on Minimum Ignition Energy in Spark Ignition of Methane/Air Mixtures," *Proceedings of the Combustion Institute*, vol. 29, no. 1, pp. 743-750, 2002, https://doi.org/10.1016/S1540-7489(02)80095-5.

[37] S. Bane, J. Ziegler and J. Shepherd, "Investigation of the Effect of Electrode Geometry on Spark Ignition," *Combustion and Flame*, vol. 162, no. 2, pp. 462-469, 2015, https://doi.org/10.1016/j.combustflame.2014.07.017.

[38] N. Kawahara, S. Hashimoto and E. Tomita, "Plasma Temperature of Spark Discharge in a Spark-Ignition Engine using a Time Series of Spectra Measurements," in *18th International Symposium on the Application of Laser and Imaging Techniques to Fluid Mechanics*, Lisbon, 2016, https://doi.org/10.4271/2019-01-2158.

[39] M. Kono, S. Kumagai and T. Sakai, "The Optimum Condition for Ignition of Gases by Composite Sparks," *Symposium (International) on Combustion*, vol. 16, no. 1, pp. 757-766, 1977, https://doi.org/10.1016/S0082-0784(77)80369-X.

[40] S. Bane, "Spark Ignition: Experimental and Numerical Investigation with Application to Aviation Safety," in *Dissertation, California Institute of Technology*, Pasadena, 2010, https://doi.org/10.7907/W1NB-5W06.

[41] S. Stepanyan, N. Minesi, A. Tibere-Inglesse, A. Salmon, G. D. Stancu and C. O. Laux, "Spatial Evolution of the Plasma Kernel Produced by Nanosecond Discharges in Air," *Journal of Physics D: Applied Physics*, vol. 52, no. 29, pp. 295-303, 2019, https://doi.org/10.1088/1361-6463/ab1ba4.

[42] M. Kono, K. Niu, T. Tsukamoto and Y. Ujiie, "Mechanism of Flame Kernel Formation Produced by Short Duration Sparks," *Symposium (International) on Combustion,* vol. 22, no. 1, pp. 1643-1649, 1989, https://doi.org/10.1016/S0082-0784(89)80176-6.

[43] D. Blunck, B. V. Kiel, L. Goss and A. Lynch, "Spatial Development and Temperature of Spark Kernels Exiting into Quiescent Air," *Journal of Propulsion and Power,* vol. 28, no. 3, pp. 458-465, 2012, https://doi.org/10.2514/1.B34131.

[44] B. Sforzo, A. Lambert, J. Kim, J. Jagoda, S. Menon and J. Seitzman, "Post Discharge Evolution of a Spark Igniter Kernel," *Combustion and Flame,* vol. 162, no. 1, pp. 181-190, 2015, https://doi.org/10.1016/j.combustflame.2014.07.024.

[45] B. Sforzo, J. Kim, J. Jagoda and J. Seitzman, "Ignition Probability in a Stratified Turbulent Flow with a Sunken Fire Igniter," *Journal of Engineering for Gas Turbines and Power,* vol. 137, no. 1, p. 011502, 2015, https://doi.org/10.1115/1.4028208.

[46] S. N. Okhovat, J. M. Hauth and D. L. Blunck, "Temperatures of Spark Kernals Discharging into Quiescent or Crossflow Conditions," *Journal of Thermophysics and Heat Transfer,* vol. 31, no. 1, pp. 120-129, 2017, https://doi.org/10.2514/1.T4927.

[47] D. C. Tinker, M. P. Pullen, R. J. Osborne and R. W. Pitz, "Examination of Annular-Electrode Spark Discharges in Flowing Oxygen – Experimental Nuances," in *AIAA SciTech 2019 Forum, AIAA 2019-0466,* San Diego, (7-11 January 2019), https://doi.org/10.2514/6.2019-0466.

[48] D. C. Tinker, R. J. Osborne and R. W. Pitz, "Examination of Annular-Electrode Spark Discharges in Flowing Oxygen - An Overview," in *AIAA Propulsion and Energy Forum and Exposition (AIAA 2018-4776)*, Cincinnati, OH, (9-11 July 2018), https://doi.org/10.2514/6.2019-0466.

[49] Y. P. Raizer, Gas Discharge Physics, Berlin, Germany: Springer-Verlag Berlin and Heidelberg GmbH & Co. KG, 1987.

[50] R. Maly and M. Vogel, "Initiation and Propagation of Flame Fronts in Lean $CH_4$-Air Mixtures by the Three Modes of the Ignition Spark," *Symposium (International) on Combustion,* vol. 17, no. 1, pp. 821-831, 1979, https://doi.org/10.1016/S0082-0784(79)80079-X.

[51] A. Trujillo-Pino, K. Krissian, M. Aleman-Flores and D. Santana-Cedres, "Accuate Subpixel Edge Location Based on Partial Area Effect," *Image and Vision Computing,* vol. 31, no. 1, pp. 72-90, 2013, https://doi.org/10.1016/j.imavis.2012.10.005.

[52] Y. Zhang and A. H. Zemanian, "A Simple Formula for the Concentration of Charge on a Three-Dimensional Corner of a Conductor," *IEEE Transactions on Microwave Theory and Techniques,* vol. 44, no. 6, pp. 975-979, 1996, https://doi.org/10.1109/22.506640.

[53] J. Rager, A. Flaig, G. Schneider, T. Kaiser, F. Soldera and F. Mucklick, "Oxidation Damage of Spark Plug Electrodes," *Advanced Materials Engineering,* vol. 7, no. 7, pp. 633-640, 1995, https://doi.org/10.1002/adem.200500025.

[54] A. Y. Falk and R. J. Burick, "Injector Design Guidelines for Gas/Liquid Propellant Systems," NASA-CR-120968, R-8973-3, Rocketdyne, Canoga Park, May 1973.

[55] G. S. Gill and W. H. Nurick, "Liquid Rocket Engine Injectors," NASA-Lewis, NASA-SP-8089, Cleveland, March 1976.

[56] R. E. Walker and D. L. Kors, "Multiple Jet Study - Final Report," Aerojet Liquid Rocket Company, Sacramento, 1973, NASA CR-121217 (N73-26286).

[57] D. F. Calhoon, D. L. Kors and L. H. Gordon, "An Injector Design Model for Predicting Rocket Engine Performance and Heat Transfer," in *AIAA/SAE 9th Propulsion Conference, AIAA-73-1242*, Las Vegas, (5-7 Nov 1973), https://doi.org/10.2514/6.1973-1242.

[58] D. L. Kors and D. F. Calhoon Sr., "Gaseous Oxygen/Gaseous Hydrogen Injector Element Modeling," in *7th Propulsion Join Specialist Conference*, Salt Lake City, 1971, https://doi.org/10.2514/6.1971-674.

[59] G. Zheng, W. Nie, S. Feng and G. Wu, "Numerical Simulation of the Atomization Process of a Like-Doublet Impinging Rocket Injector," *Procedia Engineering,* vol. 99, no. 1, pp. 930-938, 2015.

[60] M. Arienti, X. Li, M. C. Soteriou, C. A. Eckett, M. Sussman and R. J. Jensen, "Coupled Level-Set/Volume-of-Fluid Method for Simulation of Injector Atomization," *Journal of Propulsion and Power,* vol. 29, no. 1, pp. 147-157, 2013, https://doi.org/10.2514/1.B34198.

[61] Z. Huiqiang, Z. Lixin and C. K. Chan, "Numerical Simulation of Internal Flow Fields of Swirl Coaxial Injector in a Hot Environment," *Journal of Computational and Applied Mathematics,* vol. 235, no. 13, pp. 3783-3790, 2011, https://doi.org/10.1016/j.cam.2011.01.025.

[62] J. West, D. Westra, B. R. Richardson and P. K. Tucker, "Designing Liquid Rocket Engine Injectors for Performance, Stability, and Cost," in *International Conference for High Performance Computing, Networking, Storage and Analysis*, New Orleans, 2014.

[63] J. West, D. Westra, J. Lin and K. Tucker, "Accuracy Quantification of the Loci-CHEM Code for Chamber Wall Heat Fluxes in a $GO_2/GH_2$ Single Element Injector Model Problem," in *3rd International Workshop on Rocket Combustion Modeling*, Paris, 2006.

[64] D. G. Westra, J. S. West and B. R. Richardson, "Unsteady Three-Dimensional Simulation of a Shear Coaxial $GO_2/GH_2$ Rocket Injector with RANS and Hybrid-RAN-LES/DES using Flamelet Models," in *62nd JANNAF Propulsion Meeting*, Nashville, 2015.

[65] B. R. Richardson, K. Braman and J. West, "Predictive Evaluations of Oxygen-Rich Hydrocarbon Combustion Gas-Centered Swirl Coaxial Injectors using a Flamelet-Based 3-D CFD Simulation Approach," in *9th JANNAF LPS Meeting*, Phoenix, 2016.

[66] Y. J. Kim, C. H. Sohn, M. Hong and S. Y. Lee, "An Analysis of Fuel–Oxidizer Mixing and Combustion Induced by Swirl Coaxial Jet Injector with a Model of Gas–Gas Injection," *Aerospace Science and Technology,* vol. 37, no. 1, pp. 37-47, 2014, https://doi.org/10.1016/j.ast.2014.05.006.

[67] R. J. Osborne, S. K. Elam and W. P. Peschel, "Igniter Testing and Development for Liquid Oxygen/Liquid Methane ($LOX/LCH_4$) and Liquid Oxygen/Gaseous Hydrogen ($LOX/GH_2$) Injectors," in *4th Spacecraft Propulsion Joint Subcommittee Meeting, M10-0204*, Colorado Springs, (3-7 May 2010).

[68] E. A. Luke, "Loci: A Deductive Framework for Graph-Based Algorithms," *ISCOPE: Computing in Object-Oriented Parallel Environments, Lecture Notes in Computer Science,* vol. 1732, no. 1, pp. 142-153, 1999, https://doi.org/10.1007/10704054_15.

[69] E. A. Luke, X.-L. Tong, J. Wu, L. Tang and P. Cinnella, "CHEM: A Chemically Reacting Flow Solver for Generalized Grids," AIAA, 2003, Tetra Research Report, Last Verified 15 May 2020, Accessed 15 May 2020, Available at http://www.tetraresearch.com/locichem/about-locichem/.

[70] D. L. Marcum, "Advancing-Front/Local-Reconnection (AFLR) Unstructured Grid Generation," *Computational Fluid Dynamics Review,* vol. 2, no. 1, pp. 140-157, 1998, https://doi.org/10.1142/9789812812957_0008.

[71] F. Brusiani, S. Falfari and G. M. Bianchi, "Definition of a CFD Multiphase Simulation Straegy to Allow a First Evaluation of the Cavitation Erosion Risk Inside High-Pressure Injector," *Energy Procedia,* vol. 81, no. 1, pp. 755-764, 2015, https://doi.org/10.1016/j.egypro.2015.12.081.

[72] S. Marchetti and T. Rozzi, "Electric Field Singularities at Sharp Edges of Planar Conductors," *IEEE,* vol. 39, no. 9, pp. 1312-1320, 1991, https:/doi.org/10.1109/8.99039.

[73] E. T. Ong and K. M. Lim, "Three-Dimensional Singular Boundary Elements for Corner and Edge Singularities in Potential Problem," *Engineering Analysis with Boundary Elements,* vol. 29, no. 2, pp. 175-189, 2005, https://doi.org/10.1016/j.enganabound.2004.10.004.

[74] A. J. Harroun, S. D. Heister, S. V. Sardeshmekh and J. H. Ruf, "Effects of Areospike Nozzles on Rotating Detonation Engine Performance for Rocket Applications," in *AIAA SciTech Forum, AIAA 2019-0197,*, San Diego, (7-11 January 2019), https://doi.org/10.2514/6.2019-0197.

[75] A. J. Harroun, *Investigation of Nozzle Performance for Rotating Detonation Rocket Engines,* West Lafayette: Purdue University, MS Thesis, 2019.

[76] J. R. Codoni, K. Y. Cho, J. L. Hoke and F. R. Schauer, "Mach Disk Pressure Measurement Technique within Rotating Detonation Engine," in *52nd AIAA/SAE/ASEE Joint Propulsion Conference (AIAA 2016-4877)*, Salt Lake City, UT, 2016, https://doi.org/10.2514/6.2016-4877.

[77] A. J. Ruggles and I. W. Ekoto, "Ignitability and Mixing of Underexpanded Hydrogen Jets," *International Journal of Hydrogen Energy,* vol. 37, no. 1, pp. 17549-17560, 2012, https://doi.org/10.1016/j.ijhydene.2012.03.063.

[78] J. D. Anderson, Modern Compressible Flow: With Historical Perspective (Edition 3), New York City: McGraw-Hill Higher Education, 2002.

[79] S. Crist, D. R. Glass and P. M. Sherman, "Study of the Highly Underexpanded Sonic Jet," *AIAA Journal,* vol. 4, no. 1, pp. 68-71, 1966, https://doi.org/10.2514/3.3386.

[80] J. Kleinhenz, C. Sarmiento and W. Marshall, "Experimental Investigation of Augmented Spark Ignition of a $LO_2/LCH_4$ Reaction Control Engine at Altitude Conditions," NASA Glenn Research Center, NASA TM 2012-217611, Cleveland, June 2012.

[81] R. E. Biggs, "Space Shuttle Main Engine the First Ten Years," in *History of Liquid Rocket Engine Development in the United States, 1955-1980,* S. E. Doyle, Ed., Springfield, American Astronautical Society History Series, 1992, Vol. 13, pp. 69-122.

[82] W. M. Lerberghe, J. L. Emdee and R. R. Foust, "Enhanced Reliability Features of the RL10E-1 Engine," *Acta Astronautica,* vol. 41, no. 4, pp. 197-207, 1997, https://doi.org/10.1016/S0094-5765(98)00077-0.

[83] R. L. Sackheim, "Overview of United States Space Propulsion Technology and Associated Space Transportation Systems," *Journal of Propulsion and Power,* vol. 22, no. 6, pp. 1310-1333, 2006, https://doi.org/10.2514/1.23257.

[84] T. Percy, T. Posgrove, L. Alexander and J. Turpin, "Design and Development of a Methane Cryogenic Propulsion Stage for Human Mars Exploration," in *AIAA Space Forum, AIAA 2016-5492*, Long Beach, (13-16 September 2016), https://doi.org/10.2514/6.2016-5492.

[85] C. G. Fotache, T. G. Kreutz and C. K. Law, "Ignition of Counterflowing Methane versus Heated Air under Reduced and Elevated Pressures," *Combustion and Flame,* vol. 108, no. 4, pp. 442-470, 1997, https://doi.org/10.1016/S0010-2180(97)81404-6.

[86] E. Mastorakos, "Ignition of Turbulent Non-Premixed Flames," *Progress in Energy and Combustion Science,* vol. 35, no. 1, p. 57–97, 2009, https://doi.org/10.1016/j.pecs.2008.07.002.

[87] S. N. Okhovat, J. M. Hauth and D. L. Blunck, "Temperatures of Spark Kernels Discharging into Quiescent or Crossflow Conditions," *Journal of Thermophysics and Heat Transfer,* vol. 31, no. 1, pp. 120-129, 2017, https://doi.org/10.2514/1.T4927.

[88] B. Sforzo and J. Seitzman, "Modeling Ignition Probability for Stratified Flows," *Journal of Propulsion and Power,* vol. 33, no. 5, pp. 1294-1304, 2017, https://doi.org/10.2514/1.B36413.

## APPENDIX A – PH.D. NARRATIVE
## SO, YOU WANT TO LIGHT A ROCKET?

The following narrative poem translates my dissertation for all audiences. It is devoted to anyone who has had interest in a complex subject (rocket science as the obvious example), yet has not had years of training, immersion, or formal education. When this project began, I had minimal experience with the subject matter and spent countless hours reading, researching, and discussing to master it. Along the way, I refused to forget the challenges of learning this new lexicon and how many conversations required deciphering before I could begin to understand the heart of the material. This narrative is one example of how a complex subject can be distilled to an easily digestible level without losing the flavor that makes it unique, intriguing, and a basis for deeper discussion. I encourage you to always have the patience and motivation to share your work with a novice audience.

Illustrations created by Rachel Gravil.

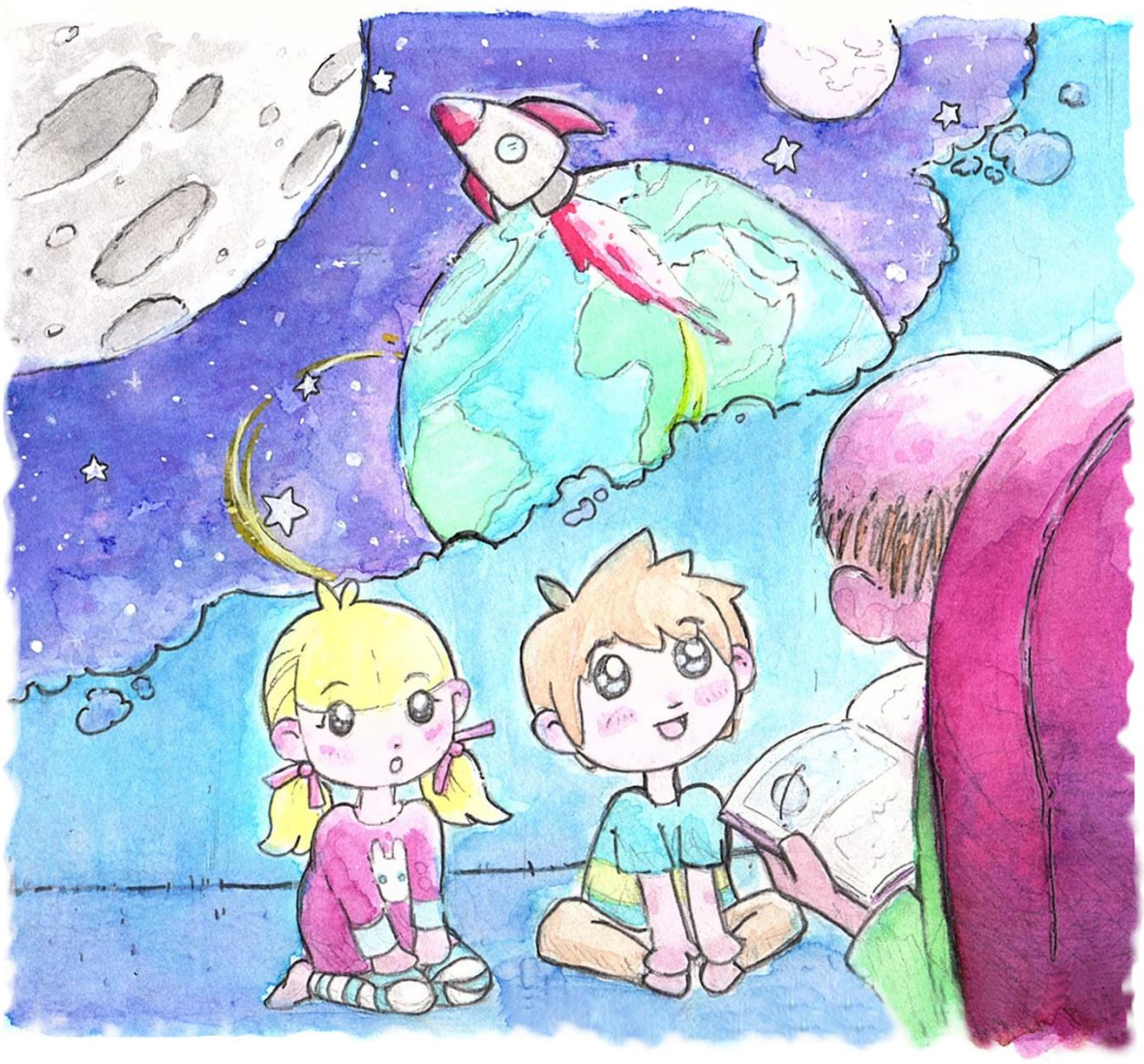

**If you want to build a rocket, or travel to the moon,**

**Or fly away to distant stars and circle ‘round Neptune,**

**If you want to go to space or any other stellar place,**

**I’ve made a tool to help you meet the challenges you’ll face.**

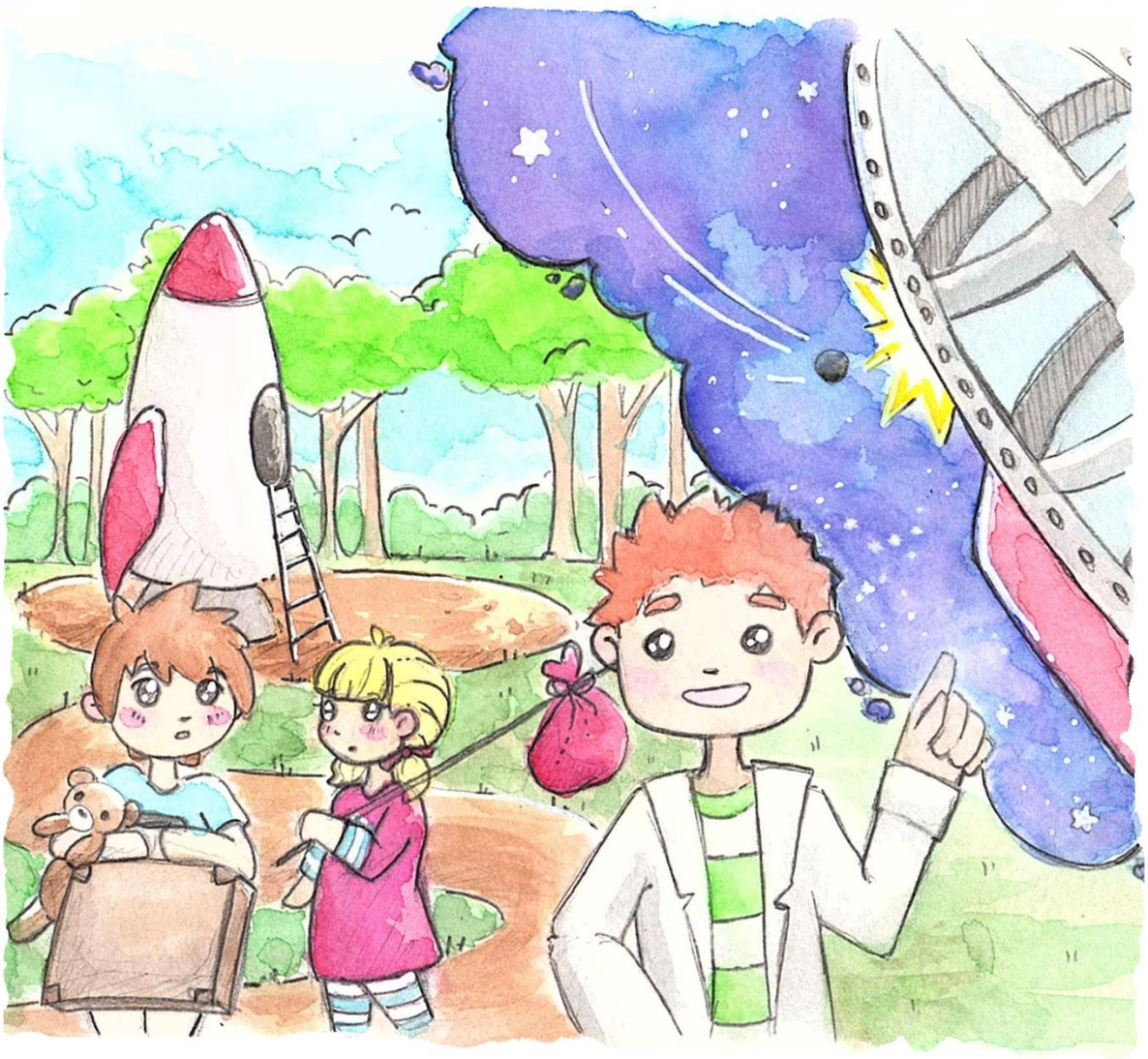

**If you want to build a rocket to go up in the sky,**

**You first require rocket parts and likely wonder why.**

**The structure or the body will hold it all together.**

**It’s made from neat materials for holding out space weather.**

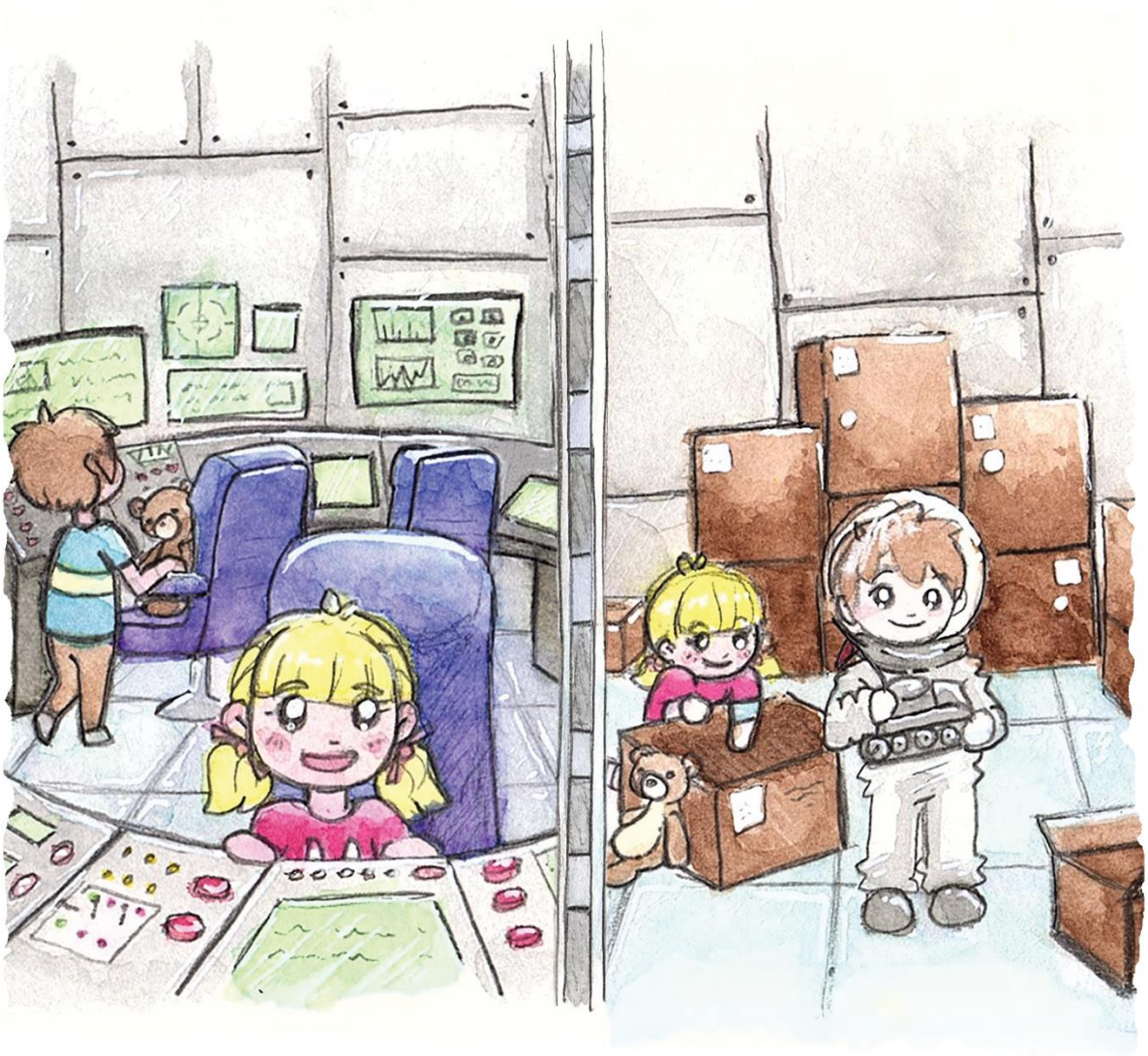

**Now our rocket needs some sensors to tell us where we are**

**And very fancy circuitry so we don’t go too far.**

**Rockets also need to hold things, like food and our supplies.**

**And last, we need to launch from Earth and soar into the skies.**

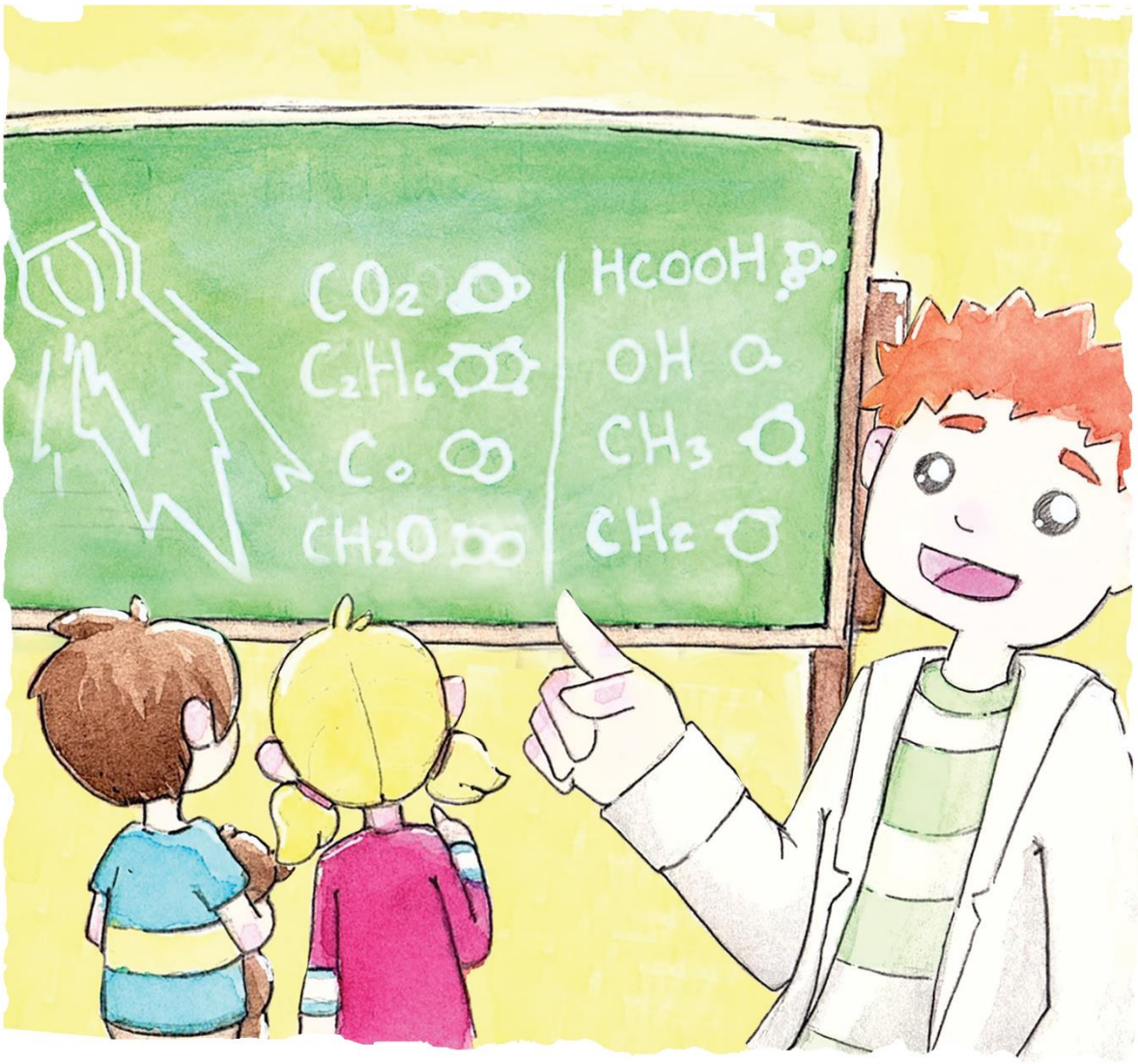


**Propulsion is a word that describes a rocket's thrust,**

**But to put it very simply, it sends a rocket up.**

**The thrust comes from the engines that burn oxygen and fuel.**

**It's a chemical reaction with lots of molecules.**


**Our next word is ignition: it's how we light the flame.**

**And no matter how we do it, the goal is just the same.**

**We want to make it safe when humans dance between the stars.**

**We want them to come home after mapping all of Mars.**

**Rocket engines are perplexing, perhaps a work of art,**

**And planning is a problem if you don’t know where to start.**

**From turbopumps to preburners, the parts all seem to blend.**

**So, let’s just focus on the chamber where fire is our friend.**


**One way to light an engine is by using hypergolics.**

**This doesn’t sound too simple, rather strange and quite symbolic.**

**It's when two things mix together and suddenly ignite,**

**Like vinegar and baking soda, or Mentos in a Sprite.**

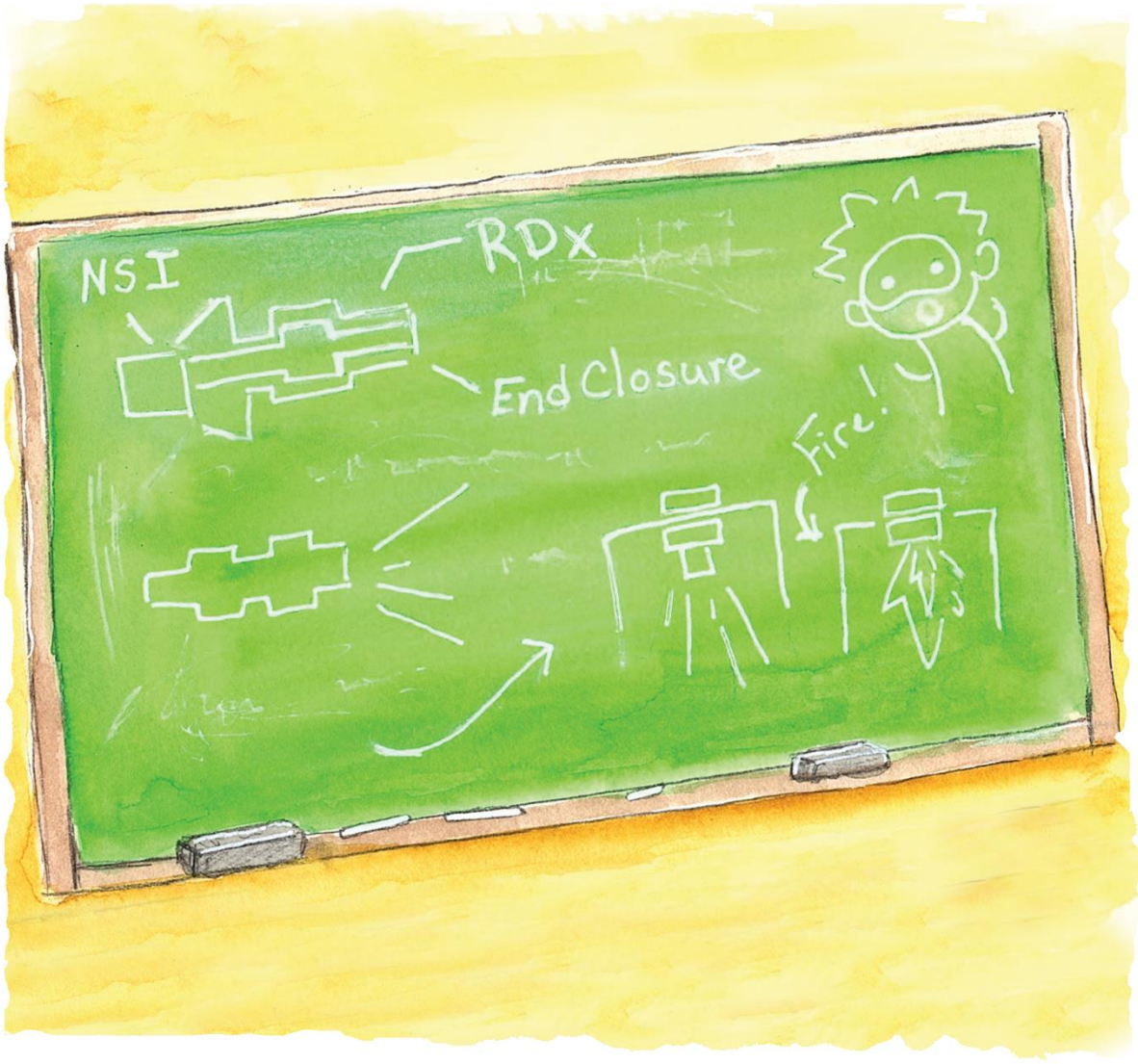


**Next are pyrotechnics, or gigantic fireworks.**

**Just as every other method, these also have their perks.**

**They block instabilities of fire and vibrations,**

**But just like hypergolics, they have their limitations.**

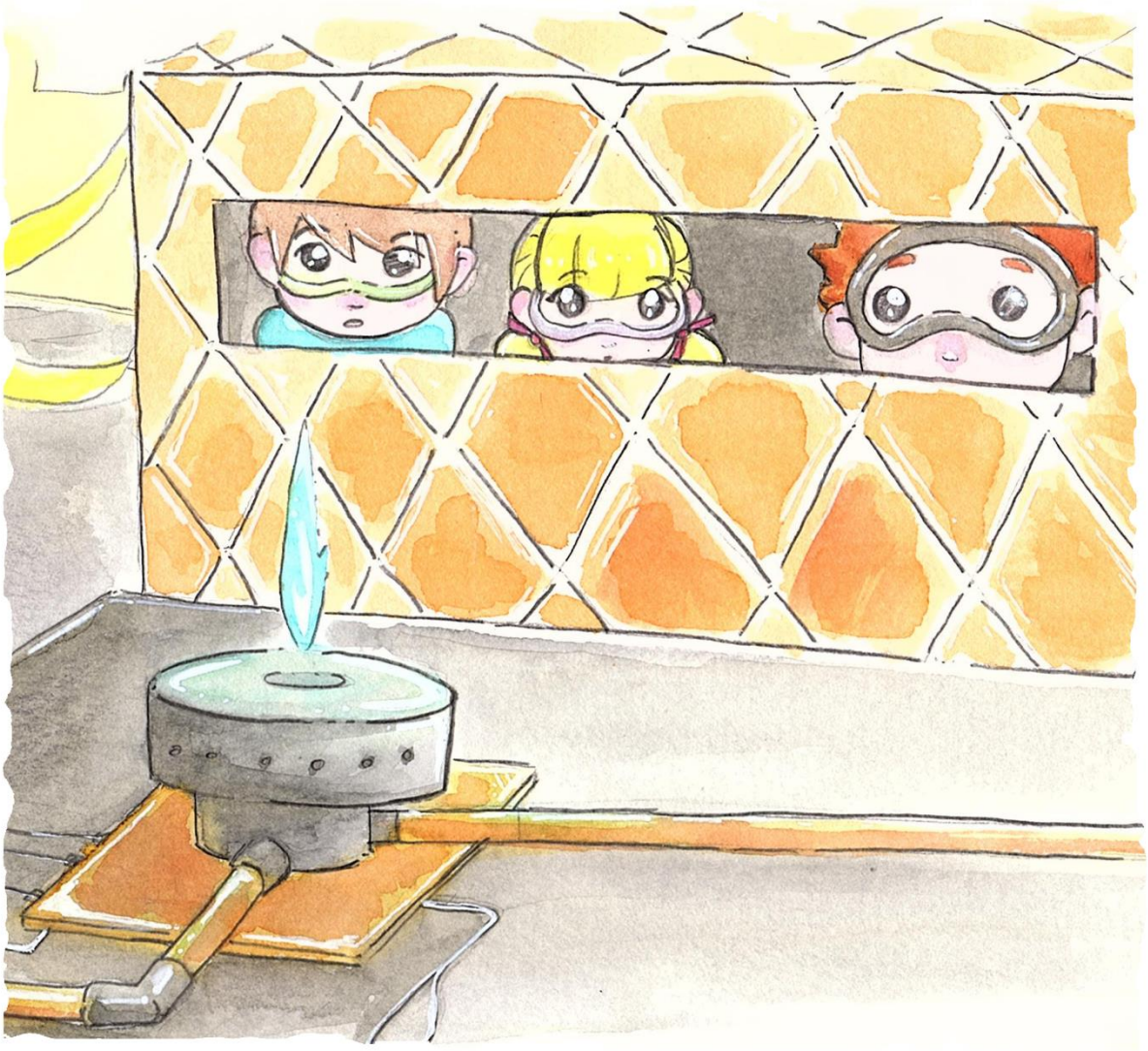

**The tried-and-true electric spark has a nice appeal,**

**But under a high pressure, they’re simply not ideal.**

**So with a little tweak, an augmentation some would say,**

**We have a new design that behaves a different way.**

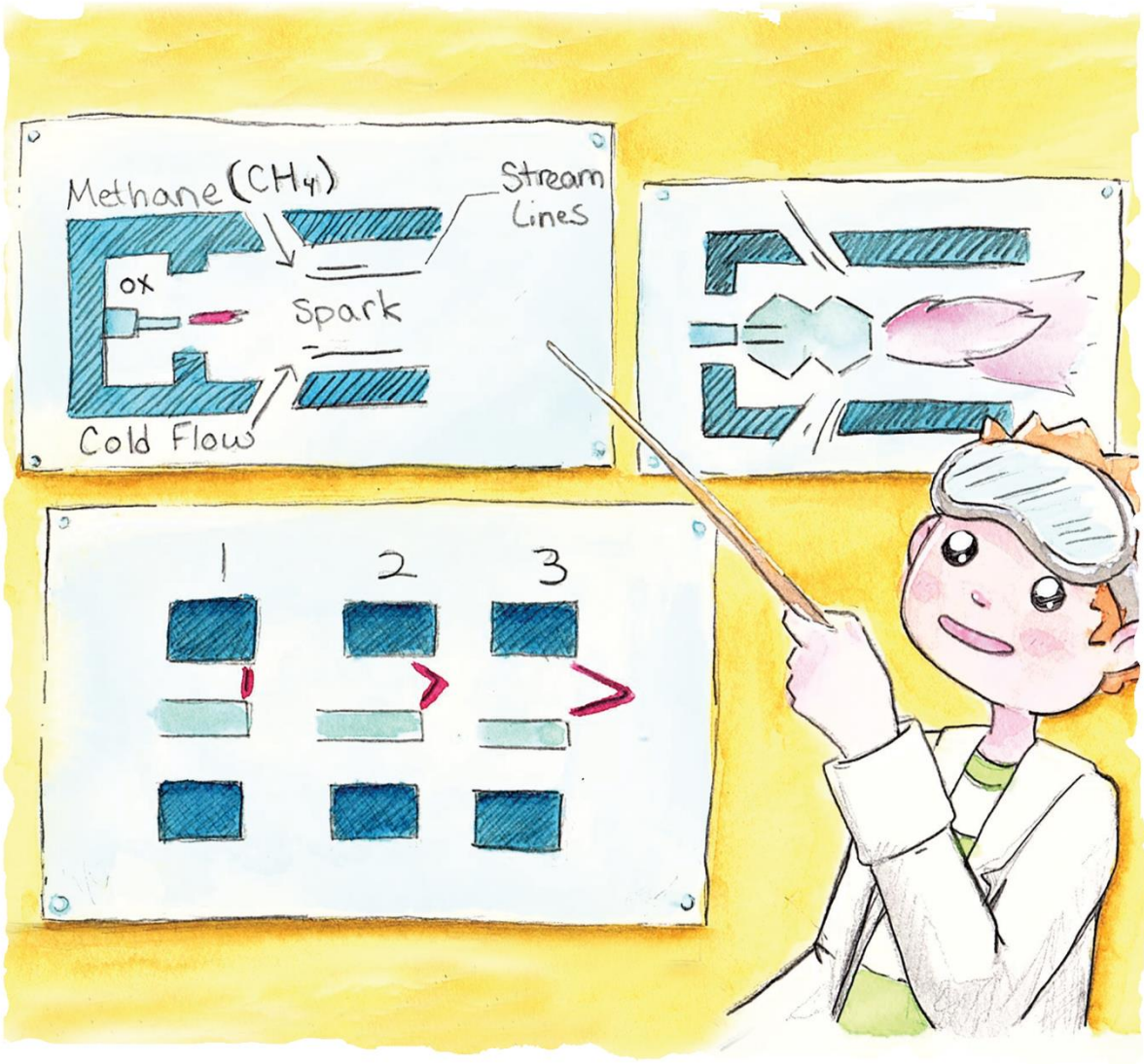


**The chamber for combustion is hard to light directly,**

**So we make a smaller tube that doesn't light complexly.**

**The tiny spark is pushed and pressed, it stretches and it grows.**

**It heats and it excites the gas! We even see it glow!**

**The oxygen we heated up bumps into our methane.**

**The molecules make much more heat! It's what we call our flame!**

**This little flame, this tiny torch, flies into the chamber.**

**In a blink, it all ignites! It grows to be much greater.**

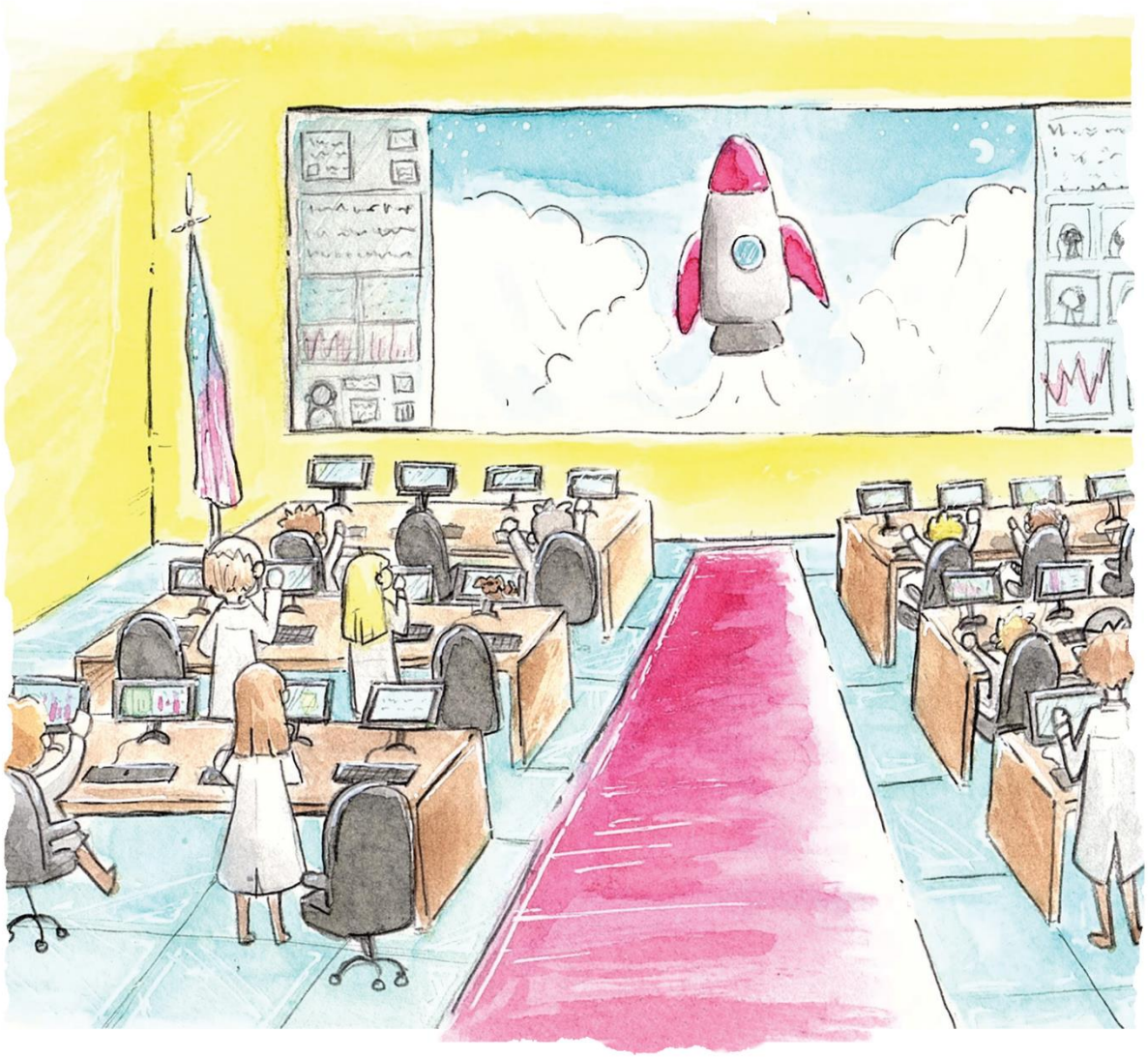

**A hot inferno races forth, a marvel to our eyes.**

**We have lift off! The ship ascends and radios good-bye!**

**In the control room on the ground, people cheer and celebrate.**

**All their work and all their effort has led to something great.**


**My work was the igniter and to try to make it better,**

**But the task was not too easy and was a lot of pressure.**

**It took a lot of math and a lot of calculations.**

**We had to have a simpler tool with fewer permutations.**

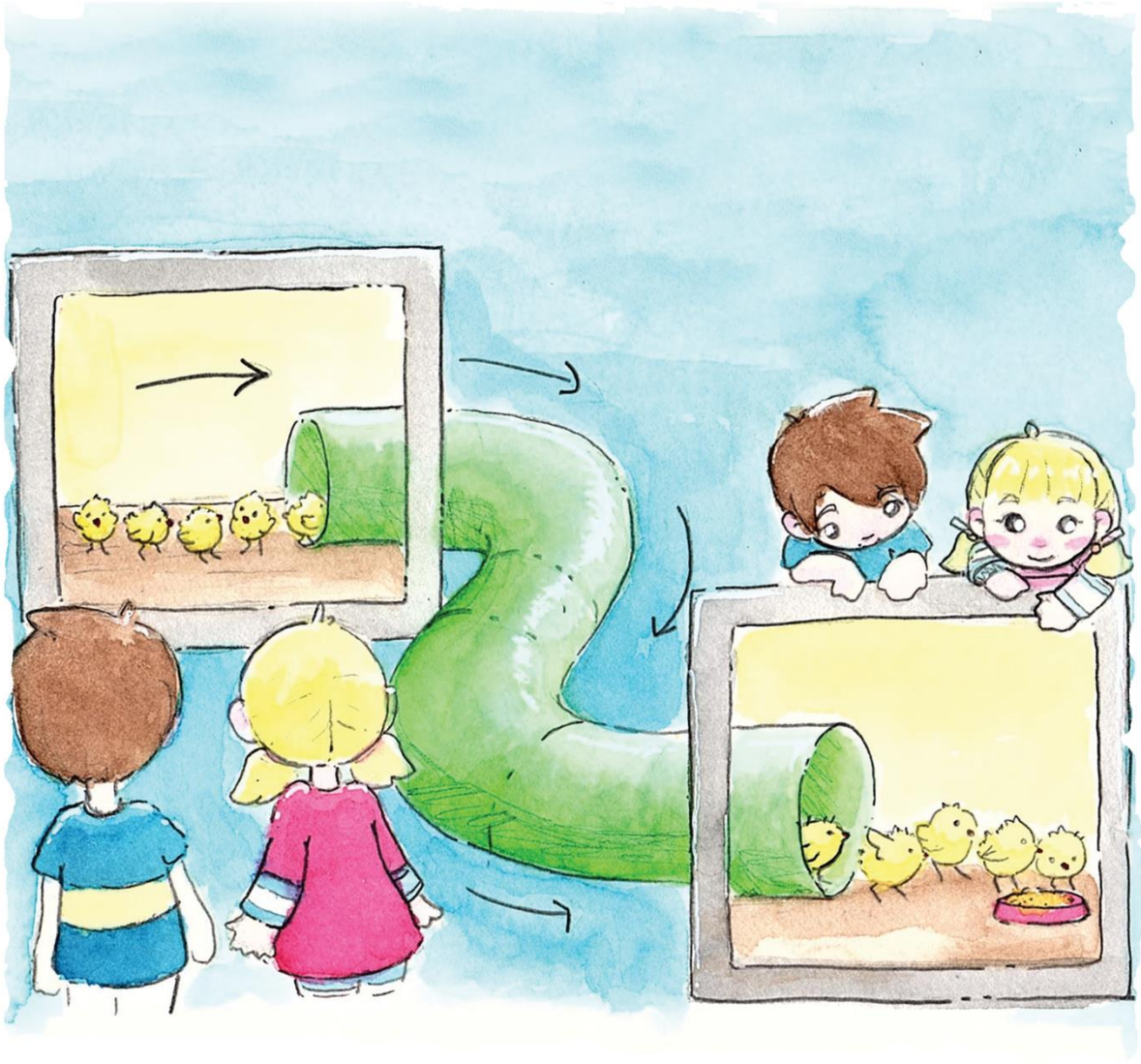

**I began with simple questions on how things bounce around.**

**We call these conservation laws! They're nothing too profound.**

**The first rule is on mass: it declares it stays the same.**

**What goes in, is what goes out! There's nothing more to claim.**

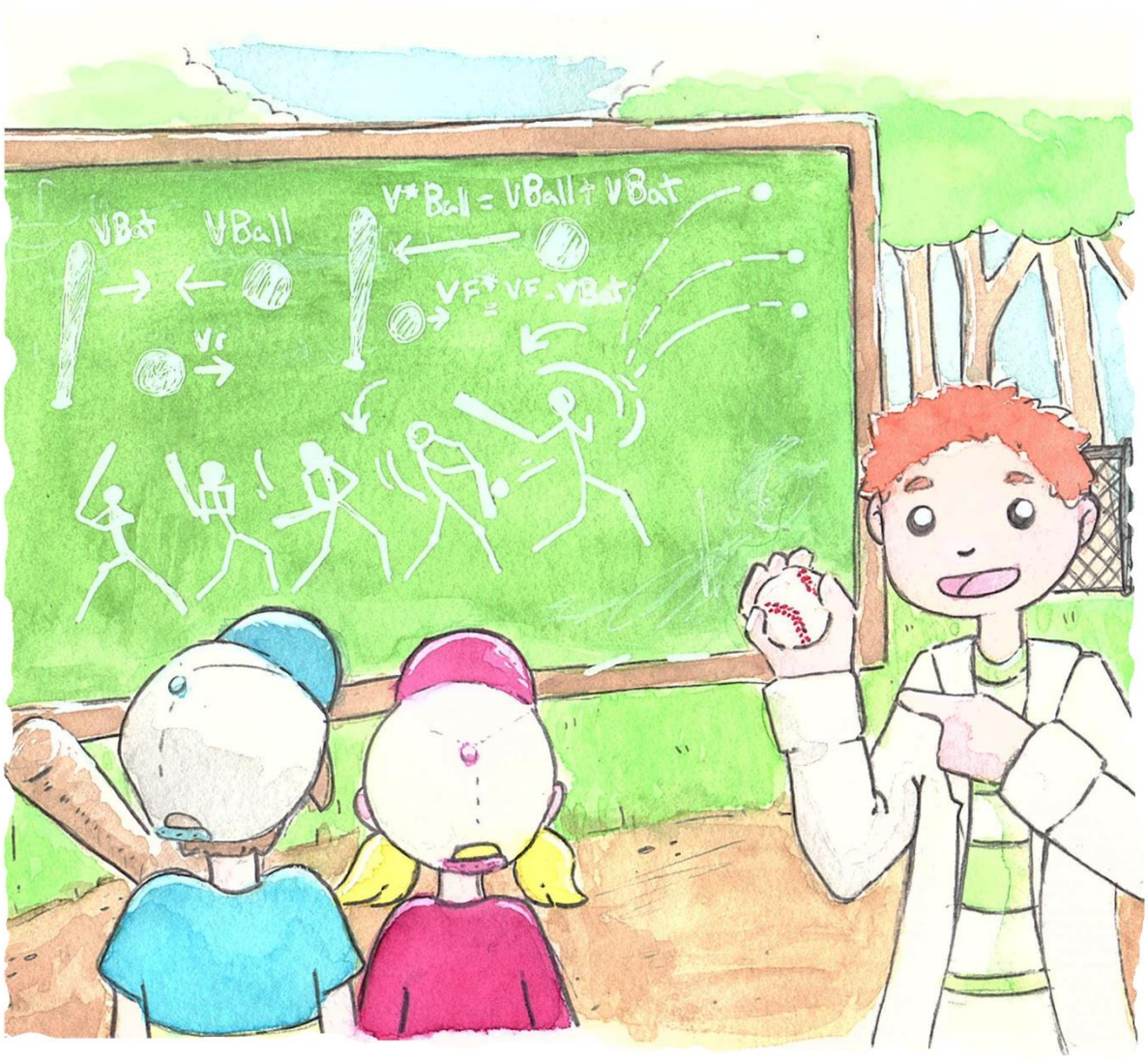


**The second is momentum. Again, things balance out.**

**When you push a thing, it pushes back and sometimes changes route.**

**Once I stated rules on how all the fluids would behave,**

**I rearranged equations until a simple one remained.**

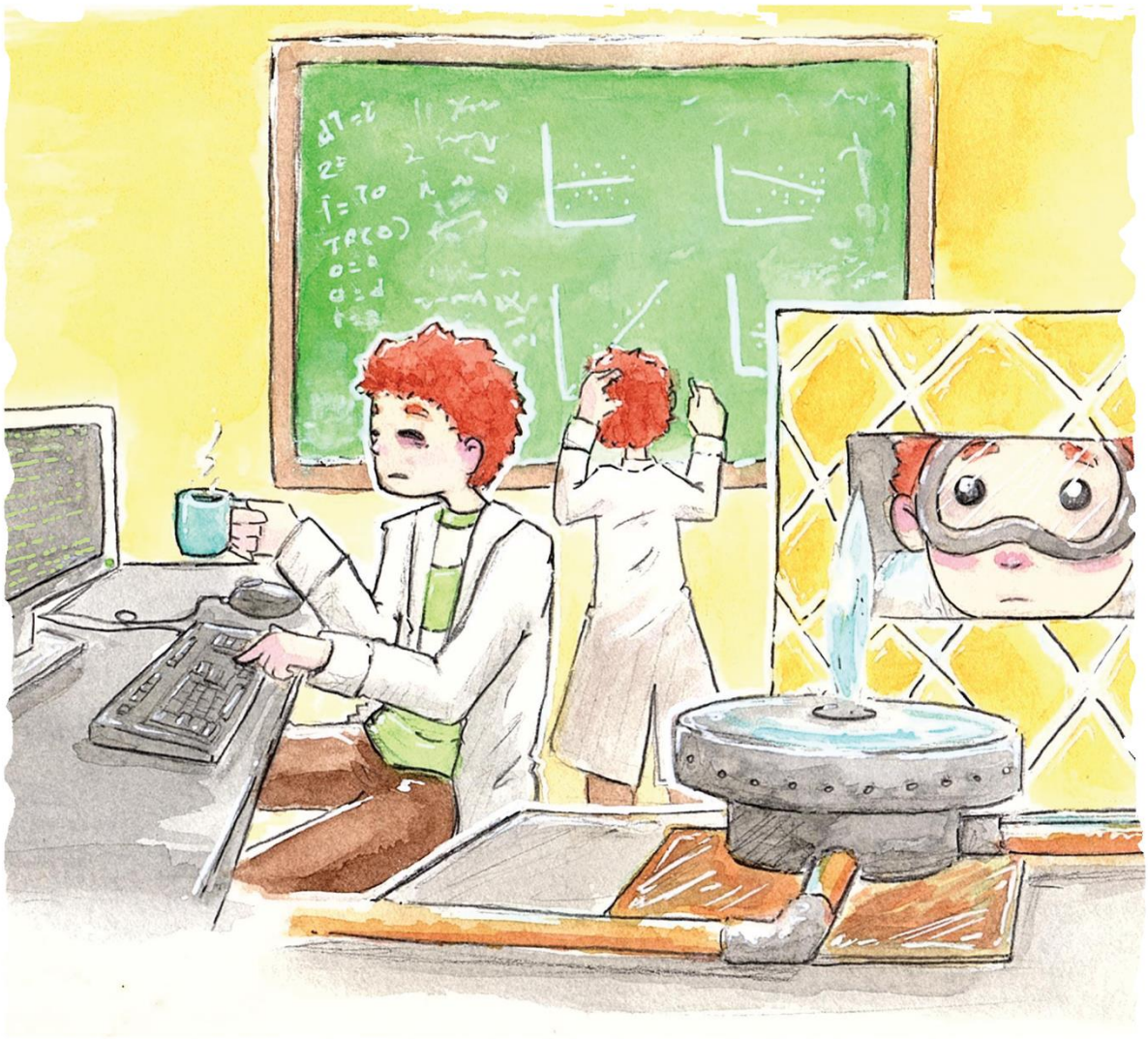

**I tested with computers by lots of simulations.**

**I looked for trends in data from my many computations.**

**The answer that fell out from it needed to be tested.**

**After many different checks, it seemed to be accepted.**

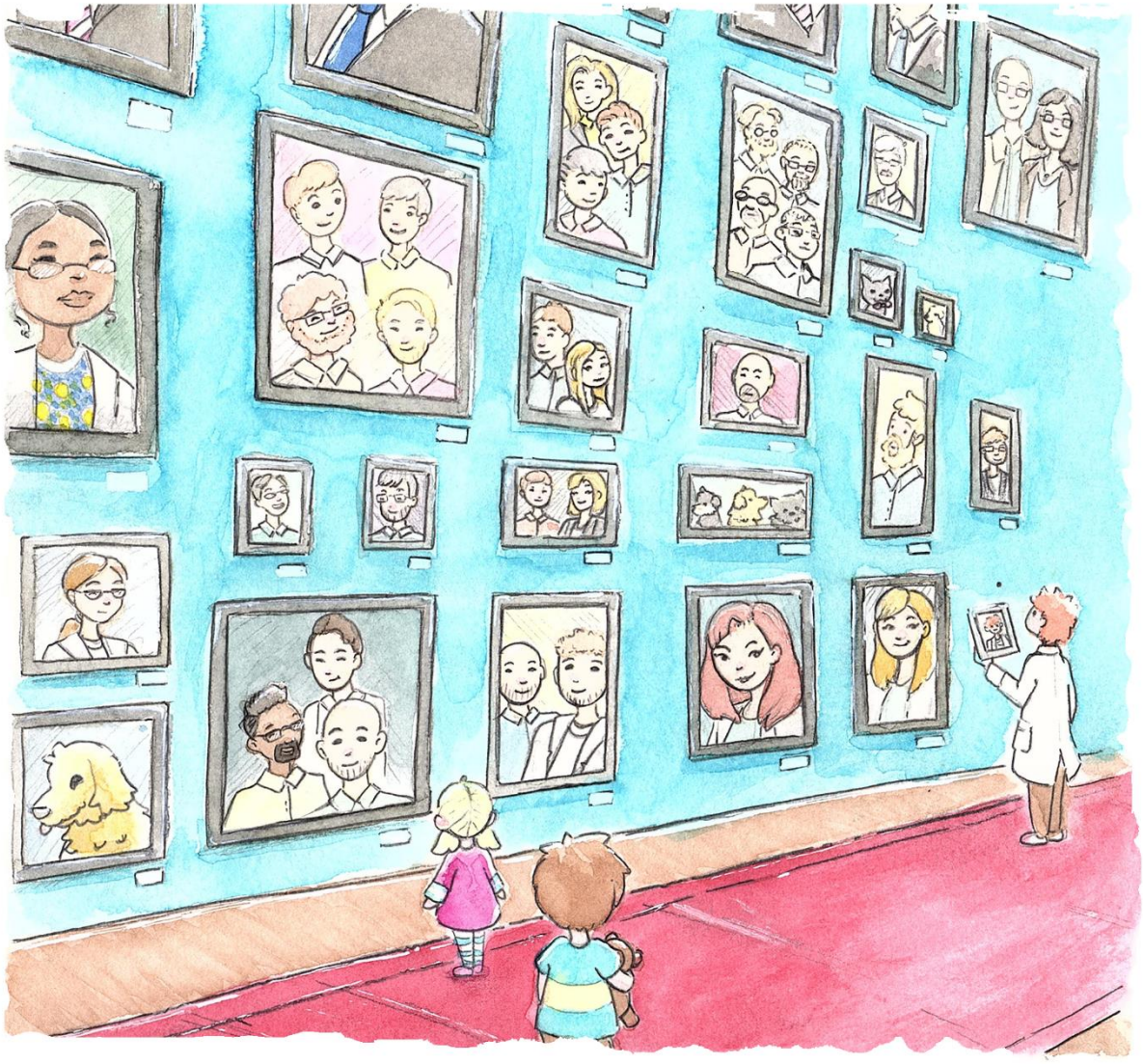

**My work was one small part, a single grain upon the shore.**

**Any difference that I've made is thanks to those who came before.**

**And one day you will both grow up and do much greater things.**

**Just don't forget to thank the ones who helped you find your wings.**

## APPENDIX B – TUBING STRESS CALCULATIONS

The pressure for experimental setups was supplied from compressed-gas bottles which have a maximum fill pressure of 3,000 psi. Assuming failure of the gas regulator, the tubing system must be able to withstand this as the maximum working pressure to ensure safety of the operator. The material selected was 316 SS with 0.035" wall thickness with stress calculations below. This is stated for informational purposes only and does not constitute a recommendation, guideline, or standard. Consult with a professional engineer and use applicable standards.

$A := 0.0\ in$ — $A$ = additional thickness

$D := 0.25\ in$ — $D$ = nominal outside diameter

$D_{tol} := 0.02\ in$ — $D_{tol}$ = outside diameter tolerance

$D_o := D - D_{tol} = 0.23\ in$ — $D_o$ = actual outside diameter

$P := 3000\ psi$ — $P$ = internal design pressure

$P_{max}$ (determined by Eq. 2) — $P_{max}$ = maximum allowable internal pressure

$SE_{Cu} := 6\ ksi$ — $SE_{Cu}$ = maximum allowable stress in copper

$t$ (determined by Eq. 1) — $t$ = nominal wall thickness

$t_m$ (determined by Eq. 1) — $t_m$ =minimum required wall thickness

$t_{tol} := 0.003\ in$ — $t_{tol}$ = wall thickness tolerance

$y := 0.04$ — $y$ =coefficient from Table 104.1.2(A) in ASME D31.1-2016

$$t_m := \frac{P \cdot (D_o)}{2\ (SE_{Cu} + P \cdot y)} + A = 0.056\ in$$ Eq. 1 - See Eq. 7 from ASME B31.1-2016

From commercial wall thickness schedules, the next available size is **0.065 in**

$t := 0.065\ in$ With tolerance, the min. thickness becomes:

$$t_m := t - t_{tol} = 0.062\ in$$ Eq. 2

$$Pmax := \frac{2\ SE_{Cu} \cdot (t_m - A)}{(D_o) - 2 \cdot y \cdot (t_m - A)} = 3306\ psi$$ Eq. 3 - See Eq. 9 from ASME B31.1-2016

For values used in the above calaculations, see standards
(1) ASTM B280 -16 - Table 2 for coil lengths
(2) ASME B31.1-2016 - Section 104.1, and Table A-6 Copper and Copper Alloys

Due to tubing length and potential for choked flow, stainless steel with 0.035 wall thickness will be used. The maximum allowable internal pressure from the same calculations is more than twofold greater than the maximum supply pressure.

$SE_{SS} := 27\ ksi$ (Assume annealed for worst case)

$t_m := 0.032\ in$ (Subtract tolerance from wall thickness)

$$Pmax := \frac{2\ SE_{SS} \cdot (t_m - A)}{(D_o) - 2 \cdot y \cdot (t_m - A)} = 7598\ psi$$ Eq. 3 - See Eq. 9 from ASME B31.1-2016

## APPENDIX C – MIXTURE RATIO CONVERSION CHART

Mixture ratio is commonly used throughout the dissertation due to industry standards and is synonymous with the oxidizer-to-fuel mass ratio. The mass fraction, mixture ratio, and equivalence ratio are related expressions that offer situational value. The mixture fraction prevents division by zero (singularities), which is useful when performing computational fluid dynamics studies whereas the equivalence ratio is ideal for chemistry-focused efforts as it is normalized to the stoichiometric mixture. As this work may be read for a variety of reasons, Figure 54 is provided for the convenience of the reader.

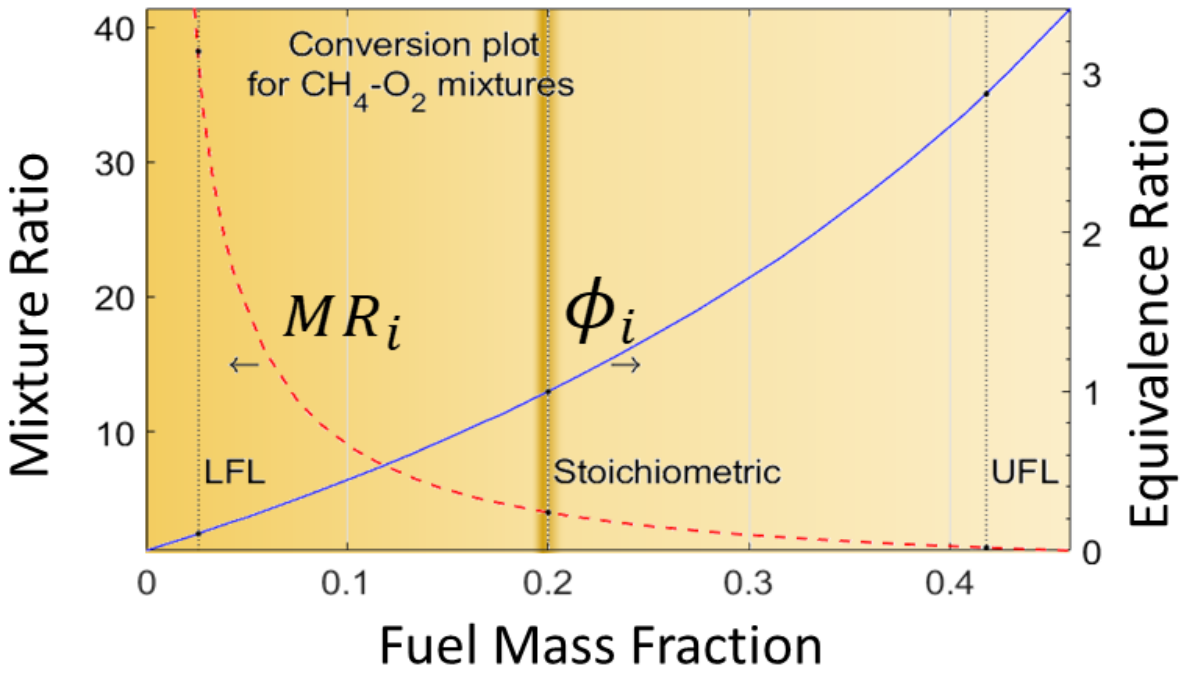


Figure 54 – Conversion chart for related terms describing methane-oxygen mixtures

## APPENDIX D – SUPPLEMENTARY CFD INFORMATION

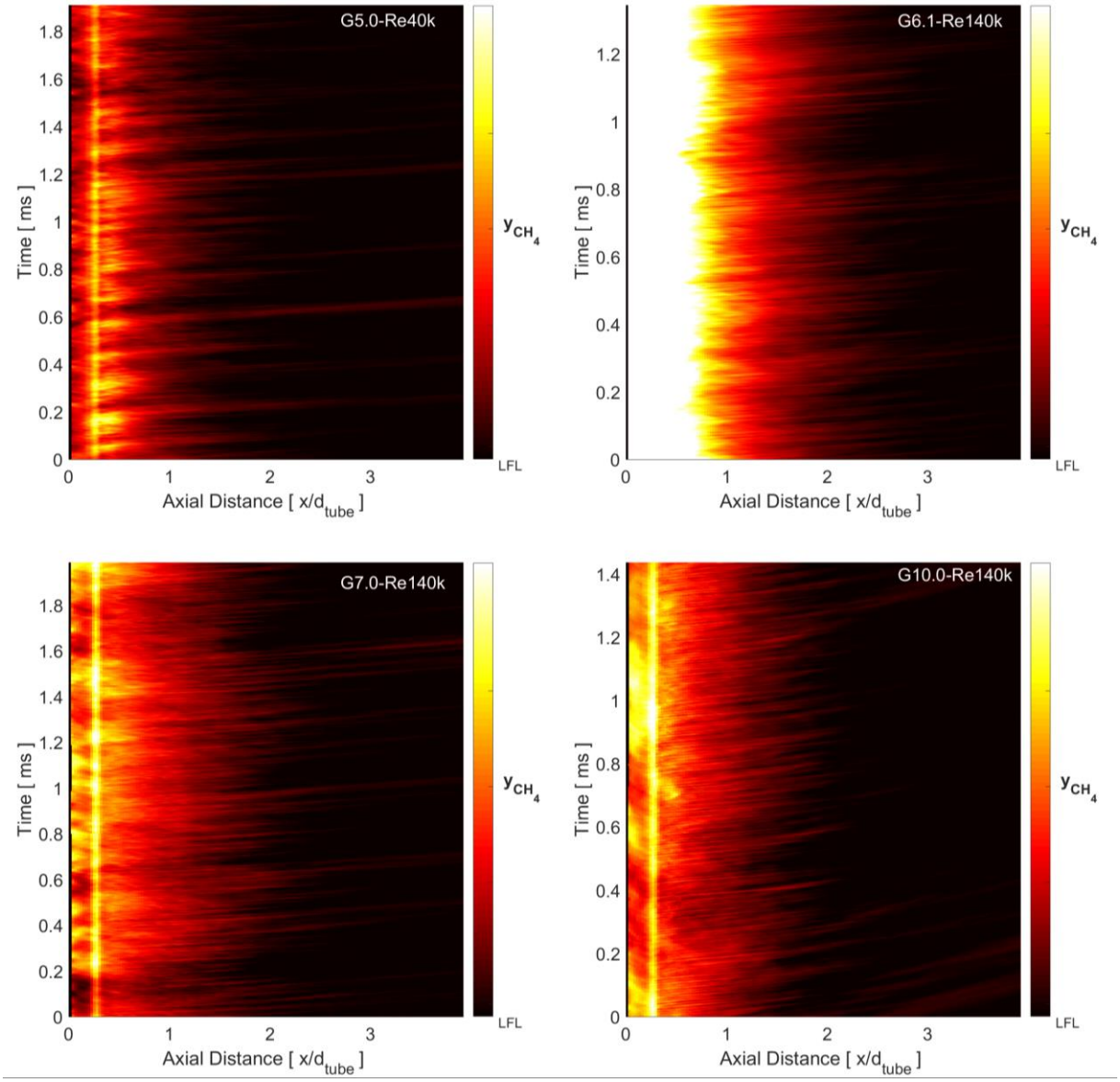


Figure 55 – Streak images of methane mass fraction (unitless) with the lower flammability limit set as the lowest value on the color scale (black). Vertical movement along each chart shows variance of methane mass fraction in a given location. Horizontal movement shows variation in methane mass fraction along the torch tube (length normalized to tube diameters) for a single snapshot in time. Flow through (residence) time for three tube diameters was 0.53 ms for *Re* 40,000 and 0.15 ms for *Re* 140,000

Table 8 – Residence times for select tube diameters vs. Reynolds number

| | | **Residence times [ms]** | | | | | | | | | |
|---|---|---|---|---|---|---|---|---|---|---|---|
| | | **Re 10k** | **Re 18k** | **Re 26k** | **Re 34k** | **Re 40k** | **Re 50k** | **Re 73k** | **Re 96k** | **Re 119k** | **Re 140k** |
| **$d_t$** | 3 | 2.10 | 1.17 | 0.81 | 0.62 | 0.53 | 0.42 | 0.29 | 0.22 | 0.18 | 0.15 |
| | 10 | 6.98 | 3.91 | 2.72 | 2.07 | 1.77 | 1.41 | 0.97 | 0.74 | 0.59 | 0.50 |